Characterization of Nipah virus in differentiated bronchial epithelial cells cultured at the air-liquid interface and Cedar virus reverse genetics

Inauguraldissertation

zur

Erlangung des akademischen Grades eines

Doktors der Naturwissenschaften (Dr. rer. nat)

der

Mathematisch-Naturwissenschaftlichen Fakultät

der

Universität Greifswald

vorgelegt von

Martin Müller

Greifswald, 18.04.2023

Dekan:	Prof. Dr. Gerald Kerth
1. Gutachter:	Prof. Dr. Stefan Finke
2. Gutachter:	Prof. Dr. Andrea Maisner
Tag der Promotion:	06.10.2023

Dedicated with Love and Memory to my Mother

Table of contents

1. Introduction

1.1. *Henipavirus*

1.1.1. *Henipavirus* classification

Paramyxoviruses are a group of large enveloped negative strand RNA viruses infecting mammals, birds, reptiles and fish (Rima et al., 2019). Many of them are important human pathogens such as the Nipah virus (NiV), Hendra virus (HeV), Measles virus (MeV) and the Mumps virus (MuV). The transmission is horizontal via direct contact or airborne routes, and in most cases resulting in an infection starting in the respiratory tract. The envelope is derived from the host plasma membrane, contains two transmembrane glycoproteins and the matrix protein which is associated with the inside of the envelope, while the genomic RNA is encapsidated and linked to the phosphoprotein and the RNA-dependent RNA polymerase (ICTV, 2012; Rima et al., 2019). Since 2018, the family of *Paramyxoviridae* includes four subfamilies instead of two. The outdated subfamily of *Paramamxyovirinea* was split into four different ones: *Avulavirinae*, *Metaparamyxovirinae*, *Orthoparamyxovirinae* and *Rubulavirinae* (Table 1). The second original subfamily of the family *Paramyxoviridae*, formerly known as *Pneumovirinae*, became an independent virus family named *Pneumoviridae*.

Table 1: Taxonomy of the *Paramyxoviridae* and important species. The family of *Paramyxovirdae* consist of the four subfamilies *Avulavirinae, Metaparamyxovirinae, Orthoparamyxovirinae and Rubulavirinae*. Classification and names are according to the ICTV.

Subfamily	Genus	Examples	Publication
Avulavirinae	*Metaavulavirus*	*Avian metaavulavirus 2*	(Bankowski et al., 1960)
	Orthoavulavirus	*Avian orthoavulavirus 1*	(Doyle, 1927; Kraneveld, 1926)
	Paraavulavirus	*Avian paraavulavirus 3*	(Shortridge and Alexander, 1978; Webster et al., 1976)
Metaparamyxovirinae	*Synodonvirus*	*Synodus synodonvirus*	(Shi et al., 2018)
Orthoparamyxovirinae	*Aquaparamyxovirus*	*Salmo aquaparamyxovirus*	(Kvellestad et al., 2003)
	Ferlavirus	*Reptilian ferlavirus*	(Foelsch and Leloup, 1976)
	Henipavirus	*Hendra henipavirus*	(Murray et al., 1995)
		Nipah henipavirus	(Chua et al., 1999)
		Cedar henipavirus	(Marsh et al., 2012)
	Jeilongvirus	*Beilong jeilongvirus*	(Li et al., 2006)
	Morbillivirus	*Canine morbillivirus*	(Carré, 1905)
		Measles morbillivirus	(Enders and Peebles, 1954)
	Narmovirus	*Nariva narmosvirus*	(Tikasingh et al., 1966)
	Respirovirus	*Murine respirovirus*	(Kuroya et al., 1953)
	Salemvirus	*Salem salemvirus*	(Renshaw et al., 2000)
Rubulavirinae	*Orthorubulavirus*	*Mumps orthorubulavirus*	(Levens and Enders, 1945)
	Pararubulavirus	*Sosuga pararubulavirus*	(Albariño et al., 2014)

Avulavirinae is divided into three genera: *Metaavulavirus*, *Orthoavulavirus* and *Paraavulavirus*, whereas the *Metaparamyxovirinae* only includes the genus of *Synodonvirus*. The biggest subfamily *Orthoparamyxovirinae* includes the *Henipaviruses* and 7 other genera: *Aquaparamyxovirus*, *Ferlavirus*, *Jeilongvirus*, *Morbillivirus*, *Narmovirus*, *Respirovirus* and *Salemvirus*. The last of the four subfamilies is divided into the two genera named *Orthorubulavirus* and *Pararubulavirus* (Walker et al., 2020).

1.1.2. Significance and epidemiology of *Henipavirus* species

NiV is a bat-borne zoonotic virus and together with the closely related HeV eponymous for the genus *Henipavirus*. Fruit bats of the genus *Pteropus* are the natural reservoir of the *Henipaviruses*. They do not develop clinical signs but secrete the virus via body fluids like urine or saliva (Middleton et al., 2007; Yob et al., 2001). However, NiV is causing severe respiratory and neurological disease in pigs and humans (Chua et al., 1999; Lee et al., 1999; Yob et al., 2001). Beside pigs and humans, bats, cats, hamsters, guinea pigs, ferrets and apes have been shown to be susceptible to NiV infection (Hooper et al., 2001; Middleton et al., 2002; Torres-Velez et al., 2008; Wong et al., 2003; Yob et al., 2001). The extraordinarily large host range, lack of a vaccine and a case fatality rate over 70 % results in the classification of *Henipaviruses* as high consequence BSL-4 pathogens for live-stock and humans (Luby and Broder, 2014). Consequently, NiV and henipaviral diseases are on the World Health Organization's blueprint list of priority diseases for an urgent need for research and development (Mehand et al., 2018; WHO, 2022).

NiV was first described in 1998, after recognition of a disease causing encephalitis among pig farmers, near the city of Ipoh in Perak, Malaysia. In March 1999, the virus was isolated from the cerebrospinal fluid of a patient from the Sungai Nipah village (Ang et al., 2018; Chua et al., 1999; Weingartl, 2015). During the initial outbreak between late 1998 and early 1999, more than 200 human NiV-infected patients were reported in Malaysia and Singapore (Chua et al., 1999). Since the first emergence of NiV, it reappeared in Bangladesh and India on an almost yearly basis (Chadha et al., 2006; Harit et al., 2006; Hossain et al., 2008; Sharma et al., 2019). It was believed that contact with diseased pigs was the primary risk factor for NiV infection. However, more recent outbreaks between 2001 and 2003 in Meherpur and Naogaon, Bangladesh, resulted in foodborne transmission through infected date palm sap, and human-to-human transmission (Figure 1) (Hsu et al., 2004; Luby et al., 2006). Genetic characterization in 2005 revealed two distinct NiV variants, NiV Malaysia (NiV_M) and Bangladesh (NiV_B) (Harcourt et al., 2005). In humans, the NiV_M strain caused respiratory symptoms in around 20 % of cases, whereas NiV_B led to respiratory symptoms in up to 70 % of human cases during the outbreaks between 2001 and 2004 in Bangladesh (Lo and Rota, 2008). Unlike previous NiV_M findings in pigs with severe respiratory symptoms, clinical signs of an NiV_B infection in swine were absent (Kasloff et al., 2019). For the high contagiosity from pig host to humans efficient infection of the respiratory tract is considered causative (Hooper et al., 2001). Vascular and epitheliotropic infections are observed in the

lungs of NiV-infected pigs with widespread vasculitis and lymphangitis. NiV antigen is located in the columnar epithelium from the trachea to small bronchioles and in brush borders of epithelial cells (Hooper et al., 2001). To understand NiV susceptibility, pathogenicity and likelihood of transmission, it is of utmost importance to investigate both NiV replication and antiviral host responses in the relevant respiratory tract cells.

HeV was identified and characterized in September 1994 in Hendra, a suburb of Brisbane, Australia causing an outbreak of a respiratory disease with fever in horses (Murray et al., 1995). Due to close contact with the affected horses, two people got infected (Murray et al., 1995). One of those succumbed to the infection within a week, while the other recovered, and died later after relapsing encephalitis (O'Sullivan et al., 1997). Overall, the mortality rate is greater than 70 % for horses and exceeds a case fatality rate of 50 % for humans (Hess et al., 2011). Serological testing of humans in close contact to infected horses revealed that the virus is not easily transmitted to humans. Direct physical contact with body fluids such as blood seems to be necessary (McCormack et al., 1999). In contrast to NiV, horses instead of pigs serve as an intermediate host (Figure 1). No human-to-human, human to horse or bat to human transmission was observed (Hess et al., 2011). Even though no other animals have been recognized to be affected, pigs, cats and guinea pigs can be infected experimentally (Hooper et al., 1997; Li et al., 2010).

Until the discovery of Cedar virus (CedPV) in 2012, the *Henipavirus* genus consisted exclusively of BSL-4 pathogens (Marsh et al., 2012). CedPV was isolated from pooled bat urine samples of *Pteropus* bats. Genome analyses from Marsh and colleagues revealed that CedPV is closely related to NiV and HeV, although it lacks pathogenicity in animal models such as ferret and guinea pigs (Laing et al., 2018; Marsh et al., 2012). It is believed that the lack of the interferon antagonistic proteins is the reason why CedPV caused no clinical signs in those animal models (Marsh et al., 2012). No outbreaks are known to this date.

Two additional species, Ghana virus (GhV) and Mojiang virus (MojV), were identified by sequencing data. Viral RNA of GhV was found by targeted RNA sequencing of fecal samples of the straw-colored fruit bat (*Eidolon helvum*) in 2009 (Drexler et al., 2012) and the MojV was discovered in 2012 from yellow-breasted rats (*Rattus flavipectus*) samples in Mojiang, Yunnan, China (Wu et al., 2014).

In 2022, the novel Angavokely virus (AngV) was identified in urine samples of wild Madagascar fruit bats. Genomic and phylogenetic analysis revealed a divergent *Henipavirus* that might be ancestral to previously described bat *Henipaviruses* (Madera et al., 2022). Furthermore, the Gamak virus (GAKV) and Daeryong virus (DARV) were isolated in 2021 from *C. lasirua* and *C. shantungensis*, respectively (Lee et al., 2021). They are related to the genus *Henipavirus* but together with AngV or the recently

identified Langya virus (LayV), which was detected in febrile patients in China, not yet classified as *Henipaviruses* by the international committee on taxonomy of viruses (ICTV, 2022; Sah et al., 2022; Zhang et al., 2022). Together with HeV and NiV, LayV remains the only *Henipavirus* with documented outbreaks.

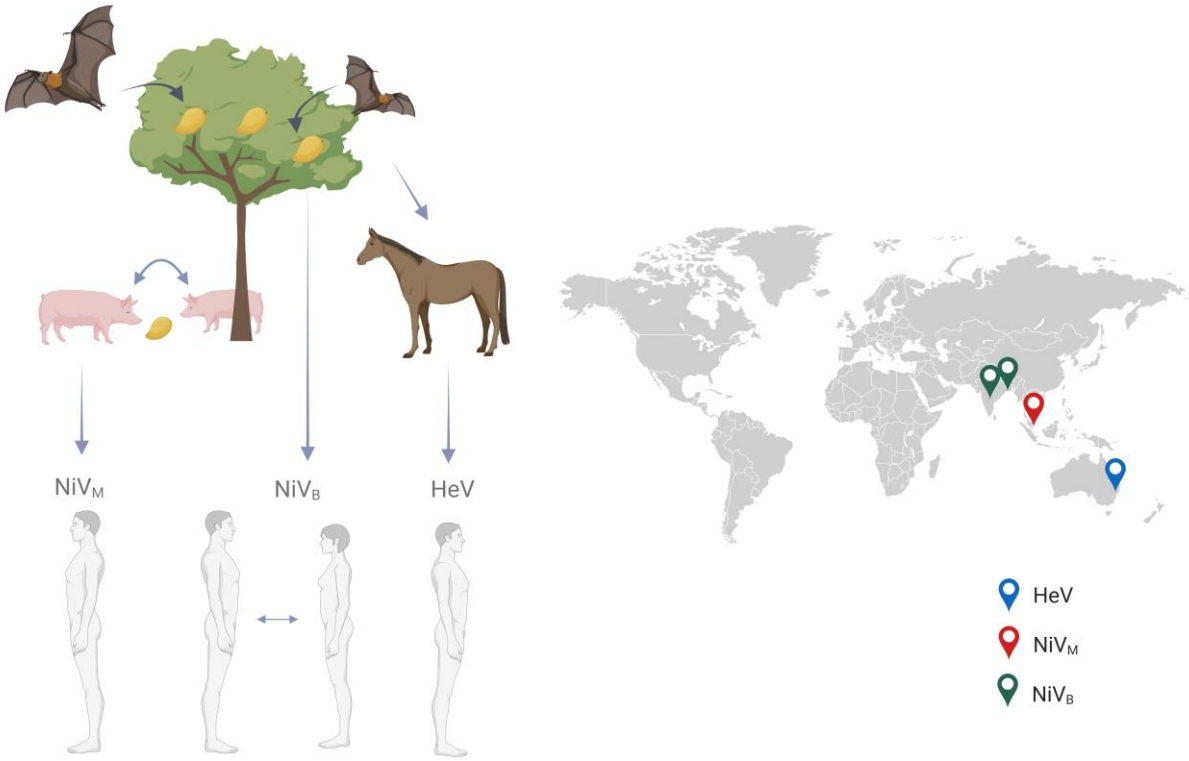

Figure 1: Main transmission routes and distribution of HeV and NiV. The natural hosts of HeV and NiV are fruit bats of the *Pteropus* species. In the case of the NiV$_M$ strain, those fruit bats can contaminate fruits, which then can be consumed by pigs, which infect humans, while for the NiV$_B$ strain in most cases the contaminated fruits are directly consumed by humans. For the NiV$_B$ strain human-to-human transmission has been observed. In contrast to NiV, the intermediate host for HeV are horses, which can be infected by bats of the *Pteropus* species. On the right, the distribution of NiV and HeV is depicted. The most important outbreak countries for NiV$_B$ (green) are Bangladesh and India, for NiV$_M$ (red), Malaysia and for HeV (blue), Australia. Modified from Dawes and Freiberg, 2019.

1.1.3. *Henipavirus* genome and proteins

The enveloped *Henipaviruses* are of pleomorphic shape and have in general a size up to 600 nm (Hyatt et al., 2001). The genome is a non-segmented negative-sense single-stranded RNA with a length of around 18 kb and six transcription units encoding for six major structural proteins (Figure 2A). In contrast to other viruses, the non-coding regions at the 3’ ends of the mRNAs are extraordinarily long and considered to have a major impact on the transcription of the downstream genes (Wang et al., 1998; Wang et al., 2000; Yu et al., 1998). Viral RNA is encapsidated by the nucleoprotein (N) forming the ribonucleoprotein complex (RNP) to which the phosphoprotein (P) and the larger viral polymerase (L, RNA dependent RNA polymerase) are associated (Figure 2B). The RNP is surrounded by the host-derived lipid membrane which is linked to the three envelope-proteins. The surface proteins, glycoprotein (G) and fusion protein (F), are embedded in the envelope and are important for the

attachment and fusion with the host membrane (Figure 2B). At the inner side of the membrane, the matrix protein (M) links the RNP to the surface proteins (Becker et al., 2022; Dietzel et al., 2016; Wang et al., 2010). The genome starts with a 3'-leader sequence comprising a promoter essential for transcription and the replicative generation of the antigenome. The 5'-trailer of the genomic RNA contains the promoter for the replicative synthesis of the antigenomic RNA. Between the leader and trailer regions, the coding sequences (CDS) for the virus proteins are sequentially organized (3'-N-P-M-F-G-L-5'). These CDS are separated by non-coding and intergenic regions.

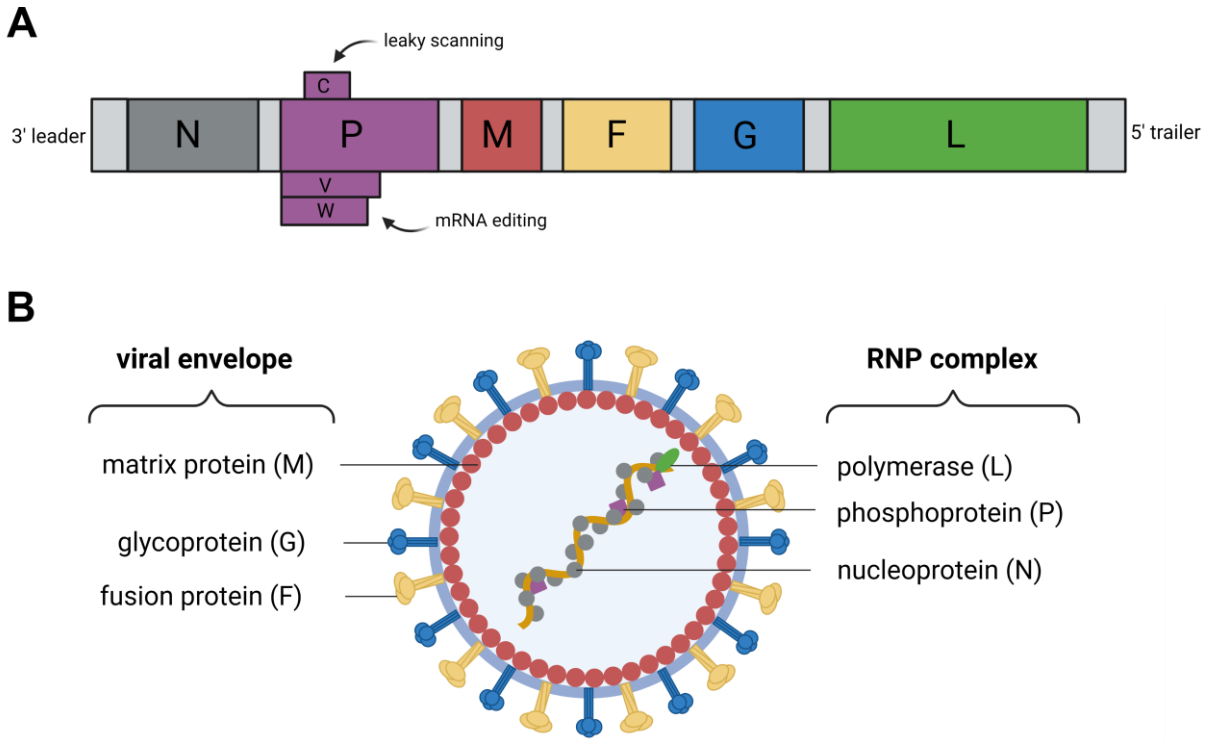

Figure 2: *Henipavirus* particle and genomic organization. (A) Genomic organization of the N, P, M, F, G, and L. The leader and the trailer region as well as the intergenic regions are indicated by gray boxes between the open reading frames (ORFs). Depending on the *Henipavirus,* nonstructural proteins can be generated. The C protein is generated by leaky scanning and a V and W protein by mRNA editing. **(B)** The *Henipavirus* virion features a pleomorphic shape that consists of six structural proteins and a host derived membrane. The two surface proteins F and G are embedded in the membrane and are in contact with the M-protein that is attached at the inside of the membrane. Together they form the viral envelope. The RNP complex consist of the genome encapsidated by the N-, P-, and L-protein.

Similar to other paramyxoviruses *Henipaviruses* conform to the rule of six. To ensure efficient replication six nucleotides of the templates for transcription and replication are associated with one N subunit (Calain and Roux, 1993; Halpin et al., 2004). N is the most abundant protein and besides the structural function and to prevent enzymatic degradation, essential for the transcription of virus mRNA and genome replication. N is furthermore involved in the inhibition of STAT-1/2 heterodimers and recruits the polymerase complex by interaction with the P-protein (Habchi et al., 2011; Sugai et al., 2017).

As a polymerase cofactor, the P-protein is involved in virus mRNA transcription and genome replication by positioning of the L polymerase on the RNP template. In contrast to all other henipaviral genes the P-gene also codes for the V-, W-, and C-proteins in addition to the P-protein. The enhanced coding capacity of the P gene relies on ribosomal leaky scanning and transcriptional mRNA editing. While the C-protein is translated from an alternative start codon, the V- and W-protein are generated through a frameshift via insertion of one or two extra G residues in the P gene transcripts (Harcourt et al., 2000; Wang et al., 2001). All of the P-variants and the P-protein itself have IFN antagonist activity (Basler, 2012; Park et al., 2003; Rodriguez et al., 2002; Shaw et al., 2005; Shaw et al., 2004). Interestingly, the CedPV P-protein lacks the ability of mRNA editing and does not produce the W or V protein (Marsh et al., 2012).

The M-protein is essential for efficient assembly and budding, although budding is observed with M-deficient mutants. However, such particles were less stable, showed a different morphology and differences in the viral envelope (Becker et al., 2022; Dietzel et al., 2016; Wang et al., 2010). For efficient budding, the M-protein forms dimers, which then assemble at the cytoplasmic side of the plasma membrane to pseudotetrameric arrays. Those arrays cause membrane curvature and finally budding of enveloped particles (Battisti et al., 2012). The membrane association of M is caused by large continuous areas of positively charged and hydrophobic residues (Battisti et al., 2012; Leyrat et al., 2014). Interestingly M has to transit the nucleus to gain the ability to localize and bud from the plasma membrane (Wang et al., 2010). Studies about the acidic leucine-rich nuclear phosphoprotein 32 family member B (ANP32B) revealed further interaction during the nuclear passage. ANP32B was identified as a nuclear target, however, the impact of the protein-protein interaction has yet to be clarified (Bauer et al., 2014; Günther et al., 2020). After the nuclear passage, M localizes in inclusion bodies (IBs) at the plasma membrane, which appear to be a platform where virus assembly and budding is facilitated (Ringel et al., 2019). In the course of virus budding, M links the RNP-complex and the surface proteins. Besides its role in virus assembly, M is involved in the inhibition of the innate IKKepsilon Kinase (IKKε)-mediated Type-I IFN antiviral response by interaction with the tripartite motif-containing protein 6 (TRIM6) (Bharaj et al., 2016).

For the virus entry in the host cell, both, F- and G- are essential. While G is a ligand for ephrin receptors for attachment to the host cell membrane, F mediates pH-independent fusion of the viral and cellular membrane (Diederich and Maisner, 2007; Diederich et al., 2005; Liu et al., 2013). Both G and F are transported to the membrane via the secretory pathway. For proteolytic activation, F is re-internalized through endocytosis and gets proteolytically cleaved in the endosomal compartment before it is then transported to the cell membrane as a fusion active F1/F2-heterodimer (Diederich and Maisner, 2007; Diederich et al., 2005; Diederich et al., 2008; Pager et al., 2006).

The L-protein is the enzymatic subunit of the viral RNA-dependent RNA polymerase. It is part of the RNP-complex and necessary for the replication and transcription. Besides the polymerase activity, it is responsible for 3'-polyadenylation, 5'-capping and methylation of the mRNA transcripts (Harcourt et al., 2001).

1.1.4. *Henipavirus* replication cycle

The replication cycle is initiated by attachment of the virions through the G-protein to the cellular receptors ephrin-B2 or -B3 or in the case of the CedPV to ephrin-B1, -B2, -A2 or -A5 (Figure 3, ①) (Laing et al., 2019). After binding to host cells, the presence of both, F and G is necessary to mediate fusion with the cell membrane and release of the RNP into the cytoplasm (Figure 3, ②) (Tamin et al., 2002). Upon virus entry, all steps of virus RNA transcription take place in the cytoplasm starting with the primary transcription. The viral genome RNP serves as a template for the transcription of monocistronic mRNAs by the viral polymerase complex (Figure 3, ③) (P and L Proteins). During transcription the polymerase complex stops at the internal transcription stop signals, polyadenylates the mRNAs, crosses the non-transcribed intergenic regions and reinitiates at the downstream transcription start signal of the next gene. During this process, the polymerase complex can dissociate from the RNP template, which leads to an mRNA gradient with highest mRNA abundance for 3'-located genes. Translation of F and G occurs at the rough endoplasmic reticulum, while N, P, M and L are synthesized by cytoplasmic ribosomes (Figure 3, ④). Furthermore, the viral genome serves as a template for the antigenome synthesis, which serves as a replicative intermediate for the generation of negative-sense genomic RNA (Figure 3, ⑤). The newly synthesized genomic and antigenomic RNAs are co-replicatively packaged in RNPs. Once sufficient N is generated, internal transcription stop signals are no longer recognized and full length genomic RNAs are synthesized. After translation, M and W are the only proteins that shuttle through the nucleus (Figure 3, ⑥). The initial inactive F-protein first undergoes endocytosis and gets proteolytically activated within endosomes prior to the transport to the cell membrane as the fusion-active F1/F2-hetereodimer, while G is not proteolytically processed (Figure 3, ⑦) (Diederich and Maisner, 2007; Diederich et al., 2005; Diederich et al., 2008; Pager et al., 2006). Afterwards, structural viral proteins and the genomic RNA are assembled at the plasma membrane. Virion assembly and release occur at the plasma membrane, where M mediates the interaction between the RNPs and the cytoplasmic domains of the surface proteins (Figure 3, ⑧) (Harrison et al., 2010; Patch et al., 2008).

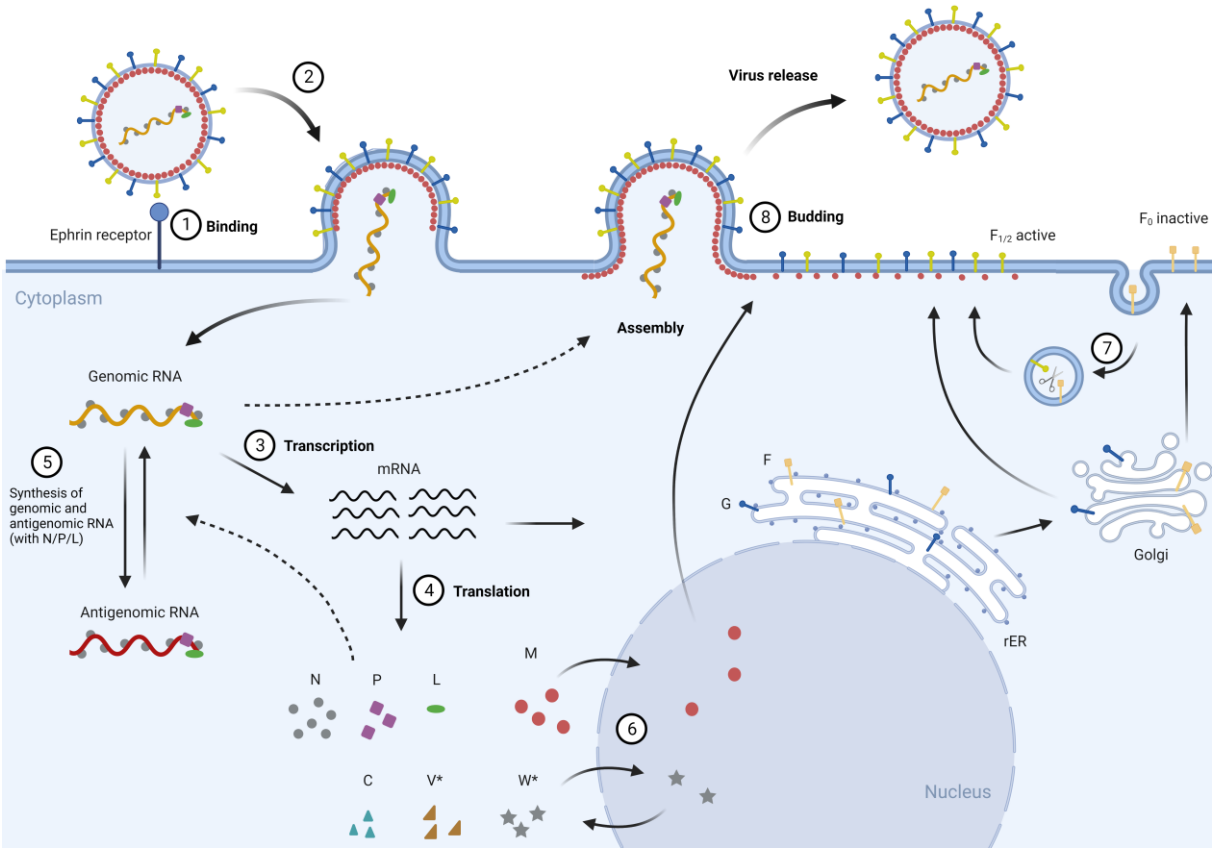

Figure 3: *Henipavirus* replication cycle. (1) Virus entry is initiated by binding of the G-protein to the ephrin-B2 or -B3 or in the case of CedPV to ephrin-B1, -B2, -A2 or -A5. **(2)** pH-independent fusion at the plasma membrane is then mediated by the F-protein. **(3)** Upon the release of the viral components into the cytoplasm, primary transcription of viral mRNAs occurs in the cytoplasm **(4)** and virus proteins are translated. **(5)** Furthermore, the viral genome serves as a template for the antigenome synthesis. **(6)** M and W undergo a nuclear passage. **(7)** The F-protein is activated in endosomes after re-internalization **(8)** and together with G incorporated in virions by budding at the plasma membrane. Stars indicate proteins not produced by CedPV.

1.1.5. *Henipavirus* reverse genetics

Reverse genetic systems drastically changed the understanding of viral replication cycles and subsequently became a fundamental tool in virus research. Until the development of reverse genetics systems to generate recombinant negative strand RNA viruses, functional studies relied on individual recombinant protein expression and minigenome systems with limited possibilities to investigate the complete virus cycles. The first negative stranded RNA virus rescued was a rabies virus in 1994 (Schnell et al., 1994). In 2006, Yoneda and colleagues constructed the first NiV full length cDNA plasmid and successfully rescued the recombinant virus. Later, several variants such as enhanced green fluorescent protein (eGFP) expressing NiV or an M-gene deletion NiV were generated (Dietzel et al., 2015). The first recombinant HeV was generated by Marsh and colleagues, including several variants, such as a GFP expressing HeV with retained ability to cause fatal disease in the ferret model (Marsh et al., 2013). A recombinant CedPV was rescued in 2018 together with a GFP expressing variant. The GFP gene insertion did not significantly affect virus replication (Laing et al., 2018). The full-length plasmids encoded the virus cDNA under the control of a bacteriophage T7 promoter (Figure 4). Downstream of

the virus cDNA, a hepatitis delta-ribozyme-sequence (HDV-SC) and a T7-Terminator sequence are located, which are required for T7 polymerase transcription termination and self-cleavage of the RNA after the last virus genome nucleotide. The latter is required to remove all non-viral sequences from the 3' full genome transcript end.

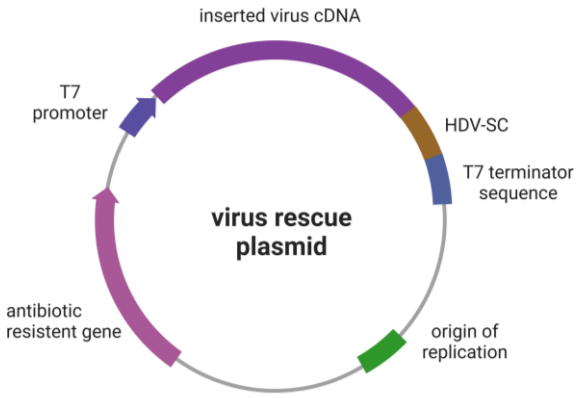

Figure 4: Organization of a typical paramyxovirus rescue plasmid. The plasmid contains an antibiotic resistant gene and an origin of replication. The inserted virus cDNA is under the control of a bacteriophage T7 promoter. Downstream of the virus cDNA, a HDV-SC and a T7-Terminator sequence are located.

For the virus rescue, the full length cDNA plasmid is co-transfected with helper plasmids encoding for the N-, P-, and L-protein in cells (Figure 5, ①). Either BSR-T7/5 cells (Buchholz et al., 1999) which constitutively express the T7 polymerase are used, or an additional plasmid for transient expression of the T7 polymerase is added to the transfection. In some cases, a highly host-restricted strain of vaccinia virus was used to express the T7 polymerase (Dietzel et al., 2015; Yoneda et al., 2006). After cytoplasmic T7 polymerase transcription of positive strand antigenome RNA, plasmid expressed N-, P-, and L-proteins result in the formation of a positive sense RNP that serves as a template for replicative synthesis of genomic RNA (Figure 5, ②). Genomic RNA synthesis, co-replicative packaging in a negative sense RNP, and subsequent transcription are mediated by the plasmids expressed N, P, and L proteins (Figure 5, ③). With transcription of virus genes from the negative sense RNP, all essential virus proteins are synthesized (Figure 5, ④ and ⑤) and an infectious virus cycle with release and spread of the virus is initiated (Figure 5, ⑥ and ⑦).

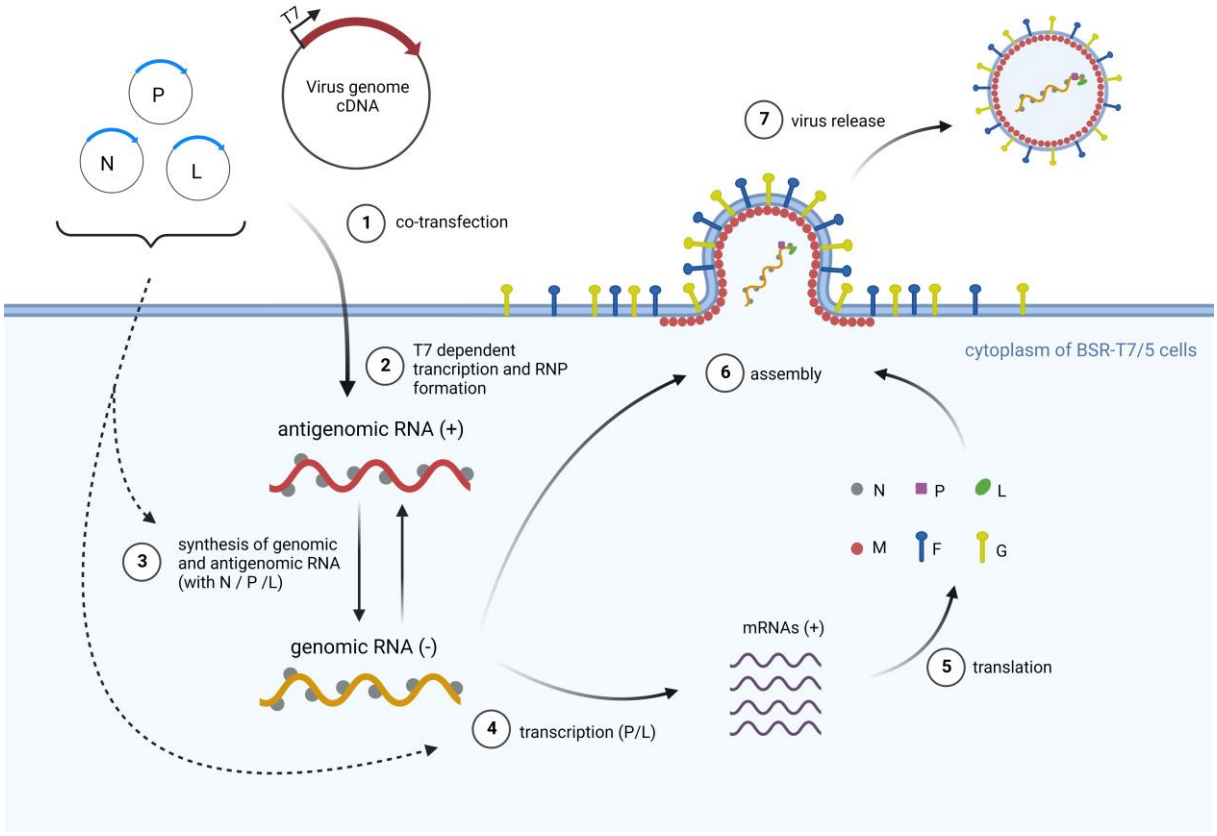

Figure 5: Schematic presentation of *Henipavirus* rescue. (1) The full length cDNA plasmid under the control of a T7 promoter is co-transfected with helper plasmids encoding for *Henipavirus* N/P/L. **(2)** Transcription of the antigenome is then mediated by the T7 polymerase supplied by BSR-T7/5 cells. **(3)** The antigenomic RNA is encapsidated and the genomic RNA can be synthesized leading to the **(4)** transcription, and **(5)** translation of all viral proteins, following the **(6)** assembly at the plasma membrane and the **(7)** virus release.

1.1.6. Nipah virus - Modulating the innate host immune response

Human monolayer cultures of primary bronchial epithelial cells (BEC) react with a pro-inflammatory response upon NiV infection (Escaffre et al., 2013). However, NiV infection of human respiratory epithelium air-liquid-interphase cultures, resembling the differentiated human tracheal/bronchial epithelia, demonstrated that NiV efficiently replicates in these cultures while only a limited antiviral host response is triggered (Escaffre et al., 2016). A limited interferon response, with pro-inflammatory cytokine expression in NiV infected BEC might also explain the efficient replication of NiV in the pig respiratory tract (Elvert et al., 2020). In contrast, HeV and NiV replication in ferret lungs induces type I interferons indicating that the virus replicates in the presence of a potent interferon response (Leon et al., 2018). Therefore, the susceptibility of the respiratory tract seems to not solely depend on the suppression of the type I IFN response by the virus (Leon et al., 2018).

Similar to most other viruses, NiV developed several ways to regulate, interact and modulate the host immune response. To this end, NiV expresses different antagonists of the innate immune responses. The most important ones are the P, V, W and C proteins. Additionally, M and N are able to interfere

with the host immune system as well (reviewed in (Pelissier et al., 2019)). While M blocks TRIM6-mediated activation of the IKKε dependent type I interferon induction and response, N interferes with the nuclear localization of signal transducer and activator of transcription (STAT)-1/2 heterodimers by hampering their complex formation (Bharaj et al., 2016; Sugai et al., 2017). Furthermore, the P and V proteins block the STAT-1/2 phosphorylation, important for the JAK/STAT pathway activated by interferons (Ciancanelli et al., 2009; Rodriguez et al., 2004; Rodriguez et al., 2002). Besides that, the V protein binds the RNA sensors laboratory of genetics and physiology gene 2 (LGP2) and melanoma differentiation-associated gene 5 (MDA5) to inhibit subsequent retinoic acid-inducible gene (RIG)-I activation (Rodriguez and Horvath, 2013). Additionally, RIG-I signaling is inhibited by the interaction of V and the caspase activation and recruitment domains (CARDs) of RIG-I as well as the V interaction with TRIM25 preventing ubiquitination of RIG-I (Pelissier et al., 2019; Sanchez-Aparicio et al., 2018). The role of V as a key player in the pathogenicity was further highlighted by experiments with a recombinant NiV V-protein deficient mutant that resulted in a replication competent but non-lethal infection (Satterfield et al., 2015). Together with M, the W-protein is the only protein that undergoes nuclear trafficking (Audsley et al., 2016; Shaw et al., 2005). It prevents nuclear translocation of interferon regulatory factor (IRF) 3/7, blocks nuclear export of STAT1/2 and accumulates cellular scaffold protein 14-3-3 in the nucleus, inhibiting NF-κB-induced pro-inflammatory responses (Ciancanelli et al., 2009; Enchery et al., 2021; Shaw et al., 2005; Shaw et al., 2004). Studies with recombinant NiV lacking the W protein revealed an altered disease course, highlighting the role as an inflammatory host response modulator that determines the disease course (Satterfield et al., 2015). By interaction with IKKα, the C-protein inhibits phosphorylation of IRF7 (Yamaguchi et al., 2014). Furthermore, it can interfere with the toll-like receptor (TLR) 7/9 dependent interferon induction (Mathieu et al., 2012; Yamaguchi et al., 2014).

1.2. Complex cell culture systems – The air-liquid interface (ALI) system

Cell culture techniques became a pillar of biology research and their influence on modern human society is immeasurable. The first cell culture was developed between 1907 and 1910 from the American embryologist Ross Granville Harrison at Yale University (Harrison, 1910). The discovery of antibiotics, the use of trypsin for the cultivation of adherent cells by Rous and Jones in 1916 and the standardization of cells and cell culture media made cell cultures a viable tool for scientists (Rous and Jones, 1916). Since then cell culture techniques have constantly gotten improved and became more complex. Beside the culturing and use of stem cells, novel approaches such as 3D cell cultures, cells cultured in a microfluidic device (organ-on-a-chip), self-organizing organoids and organ printing techniques were developed to overcome limitations of the standard cell culture. This includes lack of predictivity, missing cell types and therefore loss of heterogeneity or cell-cell and cell-matrix interaction (Abbott, 2003). With the ALI system, 3D models to represent *in vivo* biology in an *in vitro*

environment became available. The first publications date back to the second half of the 20th century where keratinocytes or pancreatic explants were cultured at the ALI (Hegre et al., 1972; Pruniéras et al., 1983). This technique allows mimicking of the respiratory tract epithelium to study the physiological and pathological responses and processes of the lung *in vitro*, as first shown by Whitcutt and colleagues in 1988 (Bals et al., 2004; Whitcutt et al., 1988). For example, drug absorption via airway delivery can be evaluated (Lin et al., 2007). Recent studies used ALI cultures to study the severe acute respiratory syndrome-coronavirus-2 (SARS-CoV-2) infection and the suppressing effect of remdesivir on viral infection and replication (Mulay et al., 2021). Furthermore, co-culture models were developed. With the addition of immune cells, for instance, the imitation of the microenvironment can be greatly improved (Blom et al., 2016; Castellani et al., 2018).

Importantly, BEC cultivated at the ALI represent a complex cell culture consisting of ciliated, goblet, basal, and club cells (Miller and Spence, 2017). Interactions and processes within these cultures exceed the ones in standard cell culture. Main differences to standard cell culture have been observed in cell-matrix and cell-cell interaction, ion transport properties, mucous secretion and cell-type specific infections (Matsui et al., 1998a; Matsui et al., 1998b; Zhang et al., 2002). Two examples are the protective layer of mucus capturing particles or the mucociliary transport to clear particles from the surface. Furthermore, differences in the receptor and protein expression levels were observed. Standard A549 cultures are resistant to SARS-CoV-2 while differentiation at ALI resulted in a decreased level of proliferation marker KI-67 and an increased level of ACE2 and TMPRSS2 switching the phenotype of A549 cells from resistant to susceptible to SARS-CoV-2 infection (Sasaki et al., 2021). Studies with influenza have shown that the physical barrier function was maintained after apical infection despite a loss of ciliated cells. However, the loss of ciliated cells might be compensated by basal cells (Wu et al., 2016). Interestingly, in differentiated respiratory epithelial cell cultures MeV caused the release of multinucleated giant cells (Lin et al., 2021). However, comparison with undifferentiated cells revealed a lower replication and interferon beta response in differentiated ALI cultures infected with influenza virus, indicating a major impact on the host innate immune response due to the differentiation status of the cells (Chan et al., 2010). This is in line with NiV infection studies on differentiated human bronchial epithelial cells where replication and shedding were observed while only a limited host response was induced (Escaffre et al., 2016). However, IFN-λ was upregulated in differentiated human BEC after NiV infection. While it is known that IFN-λ pretreatment results in antiviral activity that inhibits NiV replication, it varied between donors (Sauerhering et al., 2017).

To generate a polarized and differentiated bronchial respiratory epithelium with *in vivo*-like properties, primary lung epithelial cells are cultured at the ALI. The cells are exposed to air on the apical side and the medium is supplied from the basal side via a porous membrane (Figure 6). The two crucial parts are the isolation of primary cells and their cultivation. First, lungs are dissected. The bronchial tree is

freed from surrounding tissue prior to the dissection into small pieces (Figure 6, ① and ②). Those pieces undergo antibiotic treatment and enzymatic digestion before the BEC are expanded in collagen coated flasks (Figure 6, ③ and ④). Afterwards, they are transferred to cell culture inserts with media on the apical and basal side. With confluency of the cells the apical medium is removed to initiate cell differentiation and establishment of a pseudostratified epithelium (Figure 6, ⑤) (Bals et al., 2004; Fulcher et al., 2005).

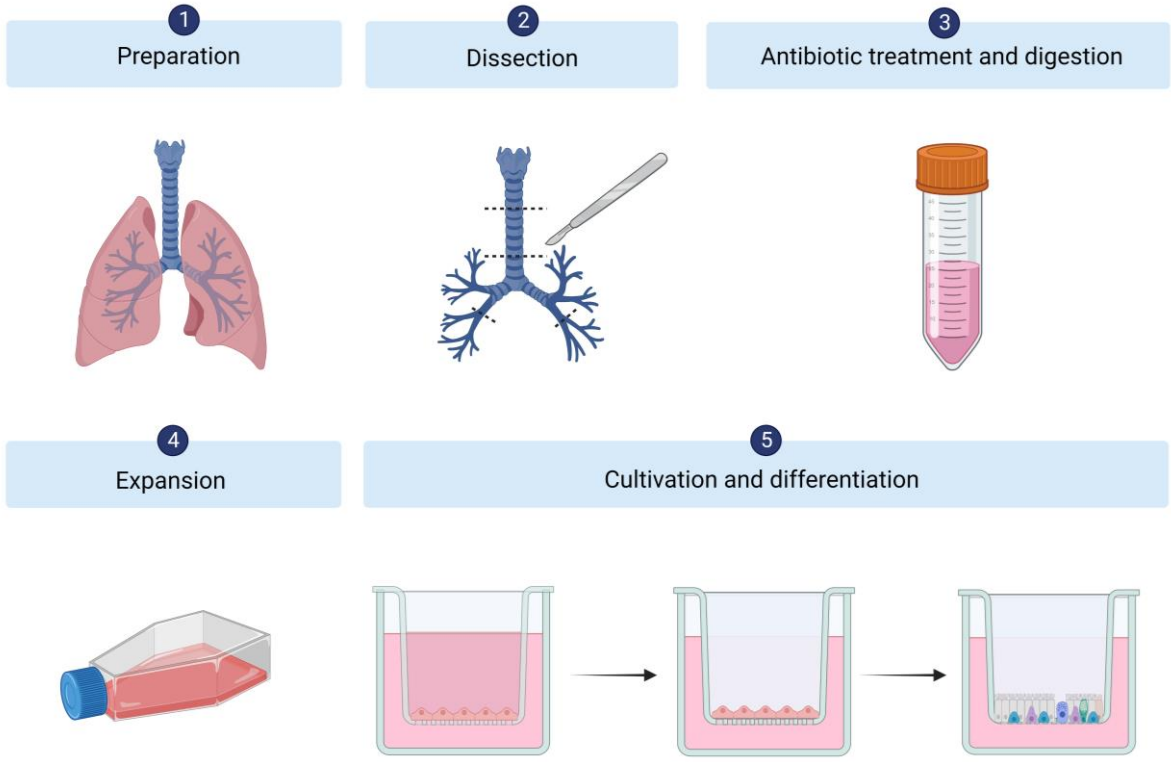

Figure 6: Preparation of primary BEC cultured at the ALI system. (1) First, the lung of the respective animal is removed, **(2)** the bronchial tree is dissected and cut into small pieces. **(3)** Afterwards, the bronchial pieces undergo an antibiotic treatment and are enzymatically digested **(4)** before they are expanded in collagen coated flasks. **(5)** Cultivation is carried out in cell culture inserts with media supplied from both sides. After the cells are confluent the differentiation is initiated by the removal of the apical medium. Differentiation takes around 4 weeks and beating cilia can be observed under a light microscope.

1.3. Mass spectrometry

Proteins are complex molecules, each with a different task. They belong to the most abundant organic molecules in biologic systems and there are many ways to detect and visualize them, but none reach the level of detail you can acquire by mass spectrometry. The foundation for this revolution in bioanalytics was laid when Wilhelm Wien discovered that beams of charged particles can be deflected by a magnetic field. The British scientist J.J. Thomson, known for his discovery of the electron in 1897, was the first person effectively using the principle of the mass spectrometry we know today. In his experiments he deflected channel rays in a magnetic field and found out that lighter ions are more deflected than the heavier ones. The idea of mass spectrometry was born and since then constantly developed. One big step into the direction of sensitivity and acquisition time was done with the time-

of-flight mass spectrometry (TOF-MS). Here, the ions are accelerated by an electric field to determine the mass-to-charge ratio by a time of flight measurement (Cameron and Eggers, 1948; Wolff and Stephens, 1953). The higher the mass-to-charge ratio, the later the ions arrive at the detector. With the introduction of the electrospray ionization (ESI), and the matrix-assisted laser desorption/ionization (MALDI), two tools to improve the resolution became available (Karas et al., 1985; Tanaka et al., 1988; Yamashita and Fenn, 1984). With those so-called "soft-ionization" methods, large biological molecules like proteins can be converted to ions mitigating a loss of sample integrity (Singhal et al., 2015). Those improvements made MS a viable tool for researchers in all scientific fields. By adding trapped ion mobility spectrometry (TIMS) to an ESI-TOF platform the sensitivity is further increased, by trapping ions in an electric field releasing them according to their mobility. The specificity is highly increased and a high speed of shotgun proteomics can be achieved, to identify proteins in complex mixtures. This platform is called timsTOF and is used in this study (Figure 7).

To identify cellular *Henipavirus* M-binding proteins, for example, mass spectrometry analysis was performed by Bauer and colleagues, revealing ANP32B as a nuclear interaction partner (Bauer et al., 2014). Independent mass spectrometric analysis off the human NiV protein interactome revealed 101 protein-protein interactions and confirmed ANP32B as an interactor of NiV M (Martinez-Gil et al., 2017). Furthermore, immunoprecipitation followed by mass spectrometry analysis revealed ephrin-B2 as a host-cell receptor for NiV (Negrete et al., 2005). Proteomic analysis can also be extended to analyze the composition of virus-like particles (VLP). Vera-Velasco and colleagues identified 67 human proteins in VLP generated by HEK293T cells and were able to estimate the ratio of incorporated viral proteins, while other studies focused on incorporated vesicular trafficking and actin cytoskeletal factors (Johnston Gunner et al., 2019; Vera-Velasco et al., 2018). Beside such interaction studies, mass spectrometry has an expanding role in vaccine development and can be combined with several techniques to achieve rapid identification of infectious agents, for example (Sampath et al., 2007; Sharma et al., 2020). utilize MS-based proteomics in combination with virus-infected ALI cultures

However, despite these advantages ALI cultures offer as a respiratory *in-vivo* like system, only a few studies exist that utilize high-resolution MS-based proteomics in combination with virus-infected ALI cultures. Most of them focusing on SARS-CoV-2 (Bojkova et al., 2020; Grossegesse et al., 2022; Hatton et al., 2021; Hekman et al., 2020; Lamers et al., 2021; Liou et al., 2021). Even less studies are published regarding NiV infection in ALI cultures (Escaffre et al., 2016) and MS studies of NiV-infected ALI cultures lack so far. The ability to analyze all proteins in a cell culture, especially in a complex culture that contains different cells and has a more complex response to infections can obtain crucial insight into the respiratory infection process and immune response (Mertens et al., 2017; Miller and Spence, 2017). In this thesis this approach was chosen to provide insight into the complex virus-host interplay and complex reaction patterns upon NiV infection.

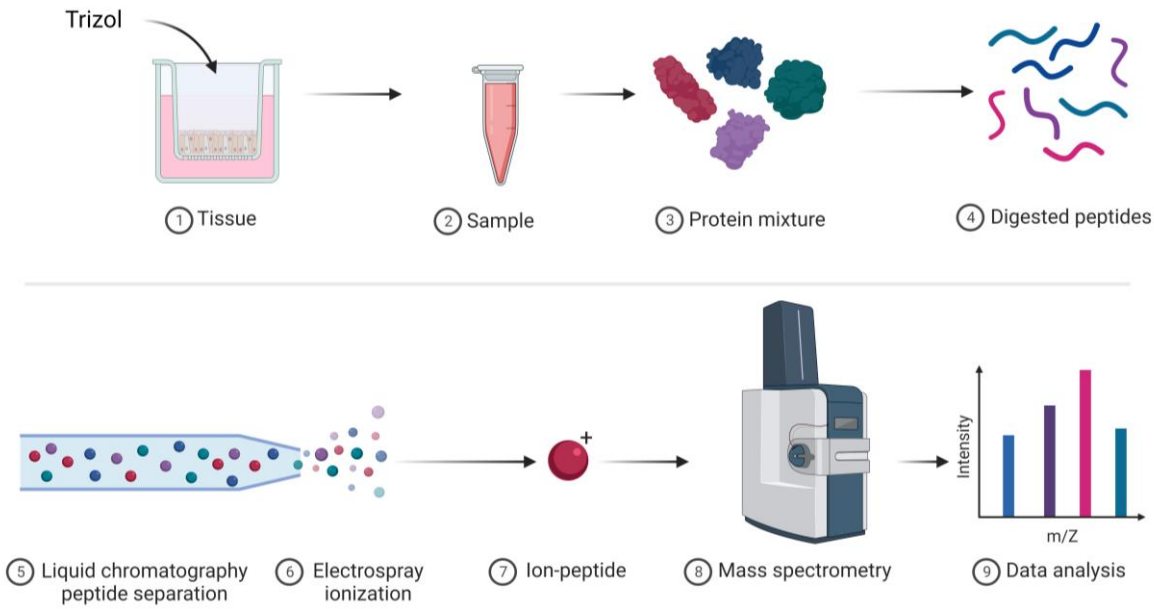

Figure 7: Overview of the MS-based proteomics workflow. For MS analysis **(1)** the tissue **(2)** is extracted **(3)** and proteins are **(4)** digested to peptides and **(5-8)** analyzed on a LC-MS platform the data is then **(9)** processed on basis of a database containing both NiV and respective animal protein sequences.

2. Objectives

Most *in vitro* studies have been performed in conventional cell lines, however, they only partially reflect the actual infection process since they lack cellular subpopulations and general physiological markers, for example. Since the respiratory epithelium acts as a barrier to virus entry and takes part in the airborne transmission studies in physiological relevant models are crucial. The susceptibility of undifferentiated pig and human BEC for NiV infection is already known from previous studies. However, differences between ferret and pig BEC cultures resulting upon NiV infection, especially in differentiated BEC-ALI cultures remains to be evaluated. Accordingly, in this thesis the infection, replication, spread and host protein dynamics of NiV in primary bronchial epithelial cells cultivated as differentiated ALI cultures was investigated. Despite the advantages ALI cultures offer, studies that utilize MS-based proteomics in combination with virus-infected ALI cultures are scarce. This thesis combines quantitative mass spectrometry proteomics with confocal-based imaging to achieve insights of the virus-host interaction during a NiV infection in a differentiated respiratory pig epithelium model. The complex experimental design was used for a comprehensive understanding of the virus replication and host reaction patterns over a 12 day time course. Consequently, important knowledge of the respiratory infection and the host immune response during the infection were addressed.

Genomic analysis from Marsh and colleagues revealed that the CedPV is closely related to the NiV and the HeV, yet it lacks the pathogenicity in animal models which is known from other *Henipaviruses* (Laing et al., 2018; Marsh et al., 2012). In order to generate a recombinant CedPV (rCedPV) that allows functional studies of *Henipaviruses* at BSL-2 facilities a CedPV cDNA full length plasmid was constructed from synthetic DNAs and rCedPV were successfully rescued. To investigate the role of cellular factors and to screen for potential host gene directed inhibitory factors, an imaging based screening and quantitative analysis pipeline were established. Therefore, different host and viral genes were targeted with siRNAs prior to CedPV infection, immunofluorescent visualization and bioinformatic quantification. With development of the siRNA screening pipeline and proof of concept for antiviral siRNA pools, various fluorescence reporter expressing viruses were generated for direct virus quantification by live cell imaging.

3.Materials

3.1. Consumables

Avicel – microcrystalline cellulose	Dupont Cell culture
Cell culture flasks with filter (25 cm^2, 75 cm^2, 150 cm^2)	Sarstedt
Cell culture plate (6-well, 12-well, 24-well, 96-well)	Corning Incorporated
Cell scraper	Sarstedt
Costar® Stripette (serological pipet) 10 ml	Corning Incorporated
Costar® Stripette (serological pipet) 2 ml	Corning Incorporated
Costar® Stripette (serological pipet) 25 ml	Corning Incorporated
Costar® Stripette (serological pipet) 5 ml	Corning Incorporated
Cover slip (ø 12 mm, 18 × 18 mm)	Carl Roth
Eppendorf tube (1 ml)	Sarstedt
Eppendorf tube (2 ml)	Starlab
Falcon tube (15 ml, 50 ml)	Sarstedt
HEPES (4-(2-hydroxyethyl)-1-piperazineethanesulfonic acid)	Sigma
Mounting medium	Ibidi
Microscope slides	VWR
Nail polish	Essence
Non-skirted Low profile-96-well PCR Plate	Thermo Scientific
Optically clear flat 8 Cap Strips	Thermo Scientific
Parafilm® M Laboratory Film	Bemis
PCR tubes	Bio-Rad
Petri dish	Sarstedt
ProLong™ Glass AntiFade Mountant	Invitrogen
Poly-L-lysin solution 0.1% (w/v) in H_2O	Sigma
Pipette tip boxes	Nerbe plus
Pipette tip filtered (1000 µl, 200 µl, 100 µl, 20 µl, 10 µl)	Nerbe plus
Pipette tip unfiltered (1 – 10 µl)	Starlab
Pipette tip unfiltered (100 - 1000 µl)	Greiner
Pipette tip unfiltered (20 – 200 µl)	Starlab
Pipette tip filtered (0.1 -2-5 µl)	Biosphere

RNA/DNA free reaction tubes (1.5 ml, 2.0 ml)	Starlab
Scalpel	B. Braun
µ-Slide 8-well	Ibidi

All devices and their software are listed with their respective methods (see 4).

3.2. Cell culture media

All cell culture media were obtained from the biobank of the Friedrich-Loeffler-Institut (FLI), Greifswald including *Alsever's Trypsin-Versene* (ATV).

Table 2: Abbreviations and composition of cell culture media obtained from the biobank of the FLI.
Abbreviation: FCS: Fetal calf serum; NCS: Newborn calf serum; DMEM: Dulbecco's Modified Eagle Medium; MEM: Minimal Essential Medium.

No.	Base medium	Serum	Supplements
ZB5	MEM Hanks, MEM Earle	10 % FCS / 2.5 %FCS	Non-essential amino acids, sodium pyruvate, $NaHCO_3$
ZB5 dd	MEM Hanks, MEM Earle (double concentrated)	5 % FCS	Non-essential amino acids, sodium pyruvate, $NaHCO_3$
ZB9d	DMEM Earle	No serum	Low glucose (1 g/l), $NaHCO_3$
ZB10	DMEM Earle	No serum	High glucose (4.5 g/l), $NaHCO_3$; Sodium pyruvate
ZB23	Glasgow's MEM	10 % NCS	Tryptose Phosphate
ZB24	Ham's F12	No serum	
ZB28	Ham's F12 / IMDM (1:1)	10 % FCS	NaHCO3
ATV			NaCl (8.5 g), KCl (0.4 g), dextrose (1 g), $NaHCO_3$ (0.58 g), Trypsin 1:250 (0.5 g), EDTA (0.2 g), ultrapure water (ad 1 l), pH 7.2
Ham's F12 Nutrient Mix	ZB24	No serum	HEPES (15 mM), gentamicin (50 µg/ml), 100 U/mL penicillin, 100 µg/mL streptomycin
Freezing medium	ZB24	10 % FCS	HEPES (37.5 mM), 10%DMSO
Titration medium	ZB5	2.5 % FCS	
Overlay medium	ZB5	2.5 % FCS	1.2% Avicel (microcrystalline cellulose)

3.3. Material used for the cultivation of BECs at the ALI

Table 3: Cell culture media, antibiotics, reagents and material used for the cultivation of BECs at the ALI.

Name	Supplier
PneumaCult-Ex medium	STEMCELL Technologies
PneumaCult-ALI medium	STEMCELL Technologies
TrypLE™ Express enzyme (1x), phenol red	Gibco
HBSS (Hank's Balanced Salt Solution)	Thermo-Fisher
Pronase	Roche
DNase I	AppliChem
Penicillin	Sigma-Aldrich
Streptomycin	Sigma-Aldrich
Gentamicin	Gibco
Amphotericin B	Sigma-Aldrich
Fluconazol	Claris Lifesciences
Collagen type I (PureCol)	Advanced BioMatrix
Collagen IV	Sigma-Aldrich
0.33 cm2, polyethylenterephtalate [PET] membrane, 0.4 µm pore size	Corning
Cell freezing container (Cool cell)	Corning

3.4. Buffers and solutions

PBS (phosphate buffered saline): 8 g NaCl, 1.15 g $Na_2HPO_4 \times 2\ H_2O$, 0.2 g KCL, 0.2 g KH_2PO_4, pH 7.4, ad 1 l ddH_2O

LB medium: 1 % (w/v) casein hydrolysate, 0.5 % (w/v) NaCl, 0.5 % (w/v) yeast extract, 1mM $MgSO_4$, in ddH_2O

LB^{++}: 20 mM $MgSO_4$, 10 mM KCl, in LB medium

All further buffers and solutions are listed with their respective methods.

3.5. Antibiotics

If not describe otherwise, antibiotics were used with the following concentrations:

Ampicillin	100 µg/ml	Carl Roth
Geneticin-418	1 mg/ml	Corning

3.6. Molecular weight marker

Quick-Load 1 kb DNA Ladder from New England Biolabs was used for agarose gel electrophoresis.

3.7. Enzymes

The Phusion Hot Start Flex DNA Polymerase, T5 Exonuclease and following restriction enzymes were acquired from New England Biolabs: DpnI, EcoRI, HindIII, NheI, ScaI, PvuII, XhoI, SmaI, PstI, XmaI and XbaI.

3.8. Oligonucleotides

Oligonucleotides are short single strands of DNA or RNA, with sequences complementary to a region of interest. They were used for molecular cloning (see 4.7), qRT-PCR (see 4.4.11) and DNA-sequencing (see 4.4.9). All oligonucleotides were obtained from Eurofins Genomics.

Name	**Sequence**
Backbone_CedPV_fw_ov	5’-TTCAAAGAAGTTTGAAAACCATCATAGAATATGGATCCGTCAGATTTGAG-3’
CedPV_HindIII_Muta_rv	5’-GCTGGTTGTATACAGTATTAGGA-3’
CedPV_Kathush_woNLS_rv_ins	5’-ATCAGCACGCTATCCTCACCCACCATATTCTATGATGGTTTTCAAAC-3’
CedPV_seq_1	5’-ATCTTACCGCTGTTGAGATC-3’
CedPV_seq_2	5’-CATGGATTCCCTAAGAAAGATT-3’
CedPV_seq_3	5’-TGAACCTGTCTATTTTAGGCTA-3’
CedPV_seq_4	5’-ATGTATACTTCTGCTGACCG-3’
CedPV_seq_5	5’-TAAACTGAATCCTGACGCAAAAC-3’
CedPV_seq_6	5’-GGATGGAAATGGAGTATGGA-3’
CedPV_seq_7	5’-GACAGAACATCCATGATGAAG-3’
CedPV_seq_8	5’-ACAAGATCACACCAGAGGT-3’
CedPV_seq_9	5’-CATCACCAAAGCAGGCATC-3’
CedPV_seq_10	5’-GTAATCTATATAGCTTTTAGTTCATGA-3’
CedPV_seq_11	5’-AGAGGACAACAGTATTGATCA-3’
CedPV_seq_12	5’-GCTACAGACATACATCAACAA-3’
CedPV_seq_13	5’-GAATACTGTCCTGTTGAGG-3’
CedPV_seq_14	5’-TGGCAAAGCCAGTAAGAGTAAC-3’
CedPV_seq_15	5’-GGAATCTCCTAATTTACAATCTAT-3’
CedPV_seq_16	5’-ATCAAGTCATTACCATCCTTATTC-3’
CedPV_seq_17	5’-AGGCAGGATTTGTCGAGAAA-3’
CedPV_seq_18	5’-AAATTGTTGCACTCAGCTATTATT-3’
CedPV_seq_19	5’-CCCAACAATCTTTATTTGGAAAT-3’
CedPV_seq_20	5’-CATGTAAAGGCCATCTGC-3’
CedPV_seq_21	5’-GGGAAATAGAGTGTATAATATTATAT-3’
CedPV_seq_22	5’-GCATTATCACCTTTAAGGGATCT-3’

CedPV_seq_23	5’-AAACTGTAACCCCAAGTATAAC-3’
CedPV_seq_24	5’-ATCTATGGTTTGCCTGGTTTC-3’
CedPV_seq_25	5’-AATATCAGCACAACAATTGCAAA-3’
CedPV_seq_26	5’-ACGAGTCGGTCACGAGAT-3’
CedPV_seq_27	5’-GATGTTCTCAAAACGATAACAC-3’
CedPV_seq_28	5’-AATGTTTGCCGTAAATTTAGGATT-3’
CedPV_seq_29	5’-CGTCAAAGCAATGAGCCTATT-3’
CedPV_seq_30	5’-CGGGCTTGTTCACTCC-3’
CedPV_seq_31	5’-CAGTCACCTTCTATGATGATGT-3’
CeV_Vec_rv	5’-CCCTATAGTGAGTCGTATTAATAC-3’
CedPV_LCDS_ov_rv	5’-TTAAGTGTTTAACTGACAAGTTGGATGTGGTTATGGATTGCTTATT ATCACGA-3’
CedPV_LCDS_ov_fw	5’-TAGTTAGAAGGAAGAAACCTTTTACCAGATATGGAAAGTGACTTTGAT ATATC-3’
CedPV_full-length_L fw	5’-CCACATCCAACTTGTCAG-3’
CedPV_full-length_L_rv	5’-ATCTGGTAAAAGGTTTCTTCC-3’
CedPV_frag1_fw	5’-TTGAATGTATTAATACGACTCACT-3’
CedPV_frag1_rv	5’-ATACCCATAAAGTAATAATGTGGA-3’
CedPV_frag2_fw	5’-CAACAGTCCACATTATTACTTTAT-3’
CedPV_frag2_rv	5’-TTGCTTCTCCCCAGTATTG-3’
CedPV_frag3_fw	5’-GGACCTGAGACCAATACTG-3’
CedPV_frag3_rv	5’-GCCCTTTTTAGTATTTCATGAAC-3’
CedPV_frag4_fw	5’-GCTTTTAGTTCATGAAATACTAAAAA-3’
CedPV_frag4_rv	5’-AACGCTTGGAGATATAAGACT-3’
CedPV_frag2_ov_backbone_rv	5’-CGCGAGGAGGTGGAGATGCCATGCCGACCCTTGCTTCTCCCCAGTATTG-3’
CedPV_frag3_ov_fw	5’-TTGAATGTATTAATACGACTCACTATAGGGGGACCTGAGACCAATACTG-3’
CedPV_frag4_ov_rv	5’-CGCGAGGAGGTGGAGATGCCATGCCGACCCAACGCTTGGAGATAT AAGACTG-3’
CedPV_frag3_ov_rv	5’-CGCGAGGAGGTGGAGATGCCATGCCGACCCGCCCTTTTTAGTATTTCA TGAAC-3’
CedPV_Complex_ov_rv	5’-CGCGAGGAGGTGGAGATGCCATGCCGACCCACCTAAAAAAGGGAATTA TAAGT-3’
CedPV K11 repair1_fw	5’-GCCAATTGTGTTGCTAATGAT-3’
CedPV K11 repair1_rv	5’-ACTTGTTTGATCATTAGCAACACA-3’
CedPV_seq_32	5’-CATTAATCCCCGCCAGCT-3’
CedPV_seq_33	5’-GGATCAGGGACTTCTAAAC-3’
CedPV_seq_1_rv	5’-TCCATAACATATCTCGGGGC-3’
CedPV_seq_2_rv	5’-TCGGGGTAAAGGGTTTCCAT-3’
CedPV_seq_3_fw	5’-CTTGAGTACGAACCTATCATGA-3’

CedPV_seq_4_rv	5’-ATATCAACGGGATCAAAGTCC-3’
CedPV_seq_5_rv	5’-CTTTCTCTTTTAAACTATAAGAAGC-3’
CedPV_seq_6_fw	5’-TGGATTTAGAGATAGACATGG-3’
CedPV_Xho_Muta_fw	5’-CTAGATGCTAACCAAATGTCTC-3’
Complex frag CedPV_rv	5’-ACCTAAAAAAGGGAATTATAAGTTTT-3’
Complex frag CedPV_fw	5’-GTAAATATCAGTCTTATATCTCCA-3’
Ced_UnaG_insM_fw	5’-TAAAGTAGGAGAGTCAGTC-3’
Ced_UnaG_insM_rv	5’-CTACCTTTCTCTTCTTCTTTGGCATATTCTATGATGGTTTTCAAAC-3’
Crep_fw_correct	5’-GGATCTGAGACTGAGATCACAGGC-3’
Crep_rv_correct	5’-GCCTGTGATCTCAGTCTCAGA-3’
Katush_fw	5’-GTGGGTGAGGATAGCGTGCTGA-3’
pt7_Vec_fw	5’-GGGTCGGCATGGCATCT-3’
StrepStrepHeVMrv	5’-TTGGCAGAGGGAAAAAGATCTGCTAGCTCACCCCTTTAGGATCTTCCC-3’
StrepSTrepHeVMfw	5’-CCACCCGCAGTTCGAAAAAGCGGCCGCTGATTTTAGTGTGAGTGATAAC-3’
trNLS_Kat_fw	5’-TGCCAAAGAAGAAGAGAAAGGTAGATCCGAAAAGAAGAGCAAGGTGGATC CTAAGAAGAAGAGCAAGGGCACGTGGGTGAGGATAGC-3’

qRT-PCR primer: Primer sequences were obtained from literature (Elvert et al., 2020).

Name	**Sequence**
NiV-N for	5’-ATCAATCGTGGTTATCTTGA-3’
NiV-N rev	5’-CAGCCAGTTCTGCAACTTGATC-3’
porcine tubulin A1b for	5’-CTGAACCGCCTTATTAGCCAAA-3’
porcine tubulin A1b rev	5’-CGTTCAGGGCCCCATCA-3’
porcine IFN-β for	5’-GCTAACAAGTGCATCCTCCAAA-3’
porcine IFN-β rev	5’-AAGCACATCATAGCTCATGGAAAG-3’
porcine IFN-λ3 for	5’-AAGAGGGCCAAGGATGCCTTTGAA-3’
porcine IFN-λ3 rev	5’-AGGCGGAAGAGGTTGAACATGACA-3’
porcine OAS1 for	5’-GAGCTGCAGCGAGACTTCCT-3’
porcine OAS1 rev	5’-TGCTTGACAAGGCGGATGA-3’
porcine ISG56 for	5’-TCAGAGGTGAGAAGGCTGGT-3’
porcine ISG56 rev	5’-GCTTCCTGCAAGTGTCCTTC-3’
porcine IL-6 for	5’-TGTCGAGGCTGTGCAGATTAGT-3’
porcine IL-6 rev	5’-GGTGGCTTTGTCTGGATTCTTT-3’
porcine IL-8 for	5’-CCGTGTCAACATGACTTCCAA-3’
porcine IL-8 rev	5’-GCCTCACAGAGAGCTGCAGAA-3’

3.9. Small interfering RNAs (siRNAs)

siRNAs are able to regulate gene expression by RNA interference. They are often used to study single gene functions or can function as a therapeutic reagent (Behlke, 2006; Sioud, 2004). All siRNAs were acquired from siTOOLs Biotech. Different host and viral genes were targeted with a siRNA-pool, each consisting of 15 or 30 different siRNAs, respectively (sense and antisense). All siRNAs are listed in Supplement 1.

3.10. Plasmids

The pCAGGS plasmid is a commonly used plasmid vector for gene expression in mammalian cells. It contains the chicken-β-actin promoter, the splice acceptor of the rabbit-β-globin gene, the human CMV (cytomegalovirus) immediate early enhancer and an ampicillin resistance gene selection in *E. coli* (Niwa et al., 1991). The expression plasmids pCAGGS CedPV-N, -P, -L used here coded for the CedPV Nucleoprotein (N), Phosphoprotein (P) and RNA-dependent RNA polymerase (L), respectively, and were obtained from Dr. Sandra Diederich, FLI.

The pt7 NiV Mini GFP plasmid, was used for the construction of the CedPV full length cDNA plasmid (see 4.7). It contains a T7 bacteriophage promoter, a hammerhead ribozyme sequence, an 85 nucleotides long hepatitis delta virus ribozyme (HDV-SC) sequence, a T7 polymerase transcription termination sequence and an ampicillin resistance gene selection in *E. coli*. Sequence is provided in Supplement 2.

pEX-A258 is a 2446 bp long cloning vector acquired from Eurofins Genomics that contains an ampicillin resistance gene.

pt7 NiV Mini GFP	NiV minigenome plasmid with insertion of an extra-cistron coding for GFP flanked by NiV genome sequences from the nucleotide positions 1 – 131 and 17894 – 18246 (GenBank accession no AF212302).
pt7 CedPV	Full-length cDNA clone of the genomic CedPV sequence (CedPV isolate CG1a, NC_025351.1) generated in this thesis.
pt7 CedPV C-R68K	Full-length cDNA clone of the genomic CedPV sequence (CedPV isolate CG1a, NC_025351.1) with a mutation at genomic nucleotide position 2312 (G2312A) generated in this thesis.
pt7 CedPV nUnaG	Full-length cDNA clone with insertion of an extra-cistron coding for nUnaG green fluorescence reporter between the P and M genes generated in this thesis. nUnaG is a nucleus-

located variant of UnaG in which the authentic sequence from the Japanese eel (*Anguilla japonica*) was fused to three copies of the nuclear localization signal from the large T antigen of SV40 virus .

pt7 CedPV TurboFP635 — Full-length cDNA clone with insertion of an extra-cistron coding for far-red fluorescent protein Katushka (TurboFP635) between the P and M genes generated in this thesis. TurboFP635 is derived from the bubble-tip anemone (*Entacmaea quadricolor*).

pt7 CedPV nTurboFP635 — Similar to the pt7 CedPV TurboFP635 plasmid, a plasmid coding for far-red fluorescent protein TurboFP635 between the P and M genes . nTurboFP635 is a nucleus-located variant fused to three copies of the nuclear localization signal from the large T antigen of SV40 virus generated in this thesis.

3.11. Cell lines

All cell lines were obtained from the biobank (*Collection of Cell Lines in Veterinary Medicine* (CCLV)) of the FLI (Isle of Riems).

BSR-T7/5: Geneticin-resistant baby hamster kidney cells derived from BHK-21 cells (clone BSR-CL13) stably expressing the T7 RNA polymerase from the T7 bacteriophage (Buchholz et al., 1999).

A549: Human lung cell line originated from pulmonary carcinoma tissue (Giard et al., 1973).

Vero: Vero cells are derived from kidney epithelial cells of an African green monkey (*Chlorocebus sp.*) (Yasumura and Kawakita, 1963).

Vero 76: This Vero cell line exhibit a lower saturation density than the original Vero cells. They were used for propagation and titration of NiV.

3.12. Bacteria

Escherichia coli (*E. coli*) XL1 blue: Commercially available *E. coli* strain (Stratagene). Genotype: *recA1 endA1 gyrA96 thi-1 hsdR17 supE44 relA1 lac [F´ proAB lacI^{q}ZΔM15 Tn10 (Tet^{r})]*.

3.13. Viruses

Nipah virus (NiV Malaysia, GenBank accession no AF212302) was propagated and titrated on Vero 76 cells. The virus was originally isolated from a human brain. Infection, propagation and titration were

carried out by Dr. Sandra Diederich and Dr. Kerstin Fischer in the BSL-4 facility of the Friedrich-Loeffler-Institut (FLI, Isle of Riems).

Recombinant CedPV (parental CedPV isolate CG1a, NC_025351.1) was generated (see 4.7.1), rescued (see 4.3.1), and quantified (see 4.3.2) as described below. Recombinant viruses rCedPV nUnaG, rCedPV TurboFP635 and rCedPV nTurboFP635 were rescued from the respective full-length cDNA plasmids (see 3.10).

3.14. Serologic reagents

3.14.1. Primary antibodies

Table 4: Primary antibodies with dilutions in working solution.

Target	Host species	Clonality	Source	RRID	Dilution
α-β-tubulin	mouse	Monoclonal	Sigma-Aldrich	AB_477577	1:100
α-Mucin-5AC	mouse	Monoclonal	Origene	N/A	1:100
α-ZO-1	rabbit	Polyclonal	Thermo Fisher	AB_2533938	1:200
α-β-catenin	rabbit	Polyclonal	Thermo Fisher	AB_2533938	1:100
α-Cytokeratin 5	rabbit	Polyclonal	Thermo Fisher	AB_869889	1:1000
α-HeV-N (detects NiV-N/CedPV N)	rabbit	Polyclonal	FLI, provided by Dr. Anne Balkema-Buschmann	N/A	1:1000
α-NiV-P (detects CedPV P)	mouse	Polyclonal	FLI, Dr. Sven Reiche	N/A	1:1000
α-HeV M	rabbit	Polyclonal	FLI, Dr. Anne Balkema-Buschmann	N/A	1:1000
α-CedPV G	mouse	Monoclonal	FLI, Dr. Sven Reiche	N/A	1:10

3.14.2. Secondary antibodies

Table 5: Fluorophore conjugated secondary antibodies with dilutions in working solution.

Target	Host species	Conjugate	Source	RRID	Dilution
α-rabbit IgG	donkey	Alexa Fluor® 488	Invitrogen	AB_2535792	1:1000
α-mouse IgG	donkey	Alexa Fluor® 488	Invitrogen	AB_141607	1:1000
α-rabbit IgG	donkey	Alexa Fluor® 568	Invitrogen	AB_2534017	1:1000
α-mouse IgG	donkey	Alexa Fluor® 568	Invitrogen	AB_2534013	1:1000

3.14.3. Fluorescent dyes

Table 6: Fluorescence dyes with dilutions in working solution. Preparation of the stock solution (10 mg/ml) was carried out according to the manufacturer's protocol.

Name	Purpose	Excitation	Source	Dilution
Hoechst 33342	DNA stain	405 nm	Molecular Probes	1:20000

3.15. Kits

Commercially available kits were acquired from Qiagen (QIAfilter Plasmid Midi/Maxi Kit, QIAquick Gel Extraction Kit, QIAquick Nucleotide Removal Kit, RNeasy kit), Invitrogen (TURBO DNA-free Kit), and Thermo Fisher (RevertAid First Strand cDNA Synthesis Kit).

3.16. Software

EndNote	Reference management software; v20.0.1
GraphPad Prism	Graphing and statistics software; v7.01
GeneiousPrime	Sequence analysis software; v2021.0.1
ImageJ	Image processing software; v1.53c
LAS X	LM software; v3.7.423463
LAS AF	CLSM software; v.2.7.3.9723
Perseus	Mass-spectrometry based software platform; v1.6.15.0
MaxQuant	Quantitative proteomics software package; v2.0.2.0
R	Software environment for statistical computing and graphics; v4.0.3
Arivis Vision4D	Image processing software; v3.5.1 (Build 12111.20211111)
Arivis Converter	File converter; v3.1.4 (Build 6978)
BioRender.com	Visualization program; web application used for all schematic images
Bio-Rad CFX Maestro	Real-time PCR analysis software; v.4.1.2433.1219

BioRender web application was used for all schematic images.

4. Methods

4.1. Cell culture methods

4.1.1. Cell cultivation

Every three or four days BSR-T7/5 (ZB23 medium), original Vero (ZB5 medium), and A549 (ZB28 medium) cells were passaged to new T-75 cell culture flasks at dilutions of 1:6, 1:6, and 1:3, respectively. BSR-T7/5 cells were supplemented with 1 mg/ml Geneticin-418 (see 3.5) each second passage to maintain the T7 polymerase transgene. To split cells, the medium was aspirated and cells were washed once with ATV before they were incubated with 3 ml of ATV (see 3.2) at 37°C and 5 % CO_2 until all cells were detached. The cells were then diluted with 3 ml medium (Table 2) and seeded into a new cell culture flask at above mentioned ratios. All cells were cultured at 37°C and 5 % CO_2 in a humid environment.

For cultivation of cells on coverslips, 18 × 18 mm coverslips were placed in Ø = 3.5 cm cell culture dishes and were coated by incubation with 2 ml poly-L-Lysin (0.1% (w/v) diluted 1:100 in H_2O) for at least 30 min at RT. After removal of the coating-solution and two washing steps with H_2O the cells were seeded on the cover slips.

4.1.2. Transfection with Lipofectamine

Lipofectamine 2000 (Invitrogen) is a cationic lipid transfection reagent, which forms complexes with negatively charged nucleic acids. The liposomes have a positively charged surface, allowing fusion with negatively charged cell membranes by overcoming the electrostatic repulsion of the cell membrane. This results in an efficient way to deliver plasmids into cells.

Transfection was carried out according to the manufacturer's protocol. Briefly, 70 % to 90 % confluent cells were transfected, if not described otherwise. DNA (a total amount of 6 µg/well of a 6-well cell culture plate, if not described otherwise) and 12 µl of Lipofectamine 2000 reagent were diluted in 250 µl of serum-free Opti-MEM medium (Gibco) in two separate reaction tubes. The diluted DNA was slowly added to the diluted Lipofectamine 2000 reagent, following a 5 min incubation at RT. Afterwards, the DNA-lipid complex was added drop by drop to the cells. The cells were then incubated as previously described (see 4.1.1), and medium was exchanged 24 h after transfection.

For siRNA transfection in 96-well cell culture plates, 1×10^4 A549 cells per well were seeded. Afterwards siRNA pools (see 3.9, 3 nM) were transfected with Lipofectamine RNAiMAX (Invitrogen) according to the manufacturer's protocol and incubated for 48 h at 37°C and 5 % CO_2. The concentration of the individual pools remained constant (3 nm) for combination of different siRNA pools.

4.1.3. Preparation, differentiation and cultivation of primary BEC

Porcine BECs were isolated from the airways of healthy pigs aged 6- to 12-months and ferret BECs from 1- to 2 year aged ferrets. Cultivation and isolation was modified from previous descriptions for humans (Fulcher et al., 2005). The lung was removed and the bronchial tree dissected, washed with PBS and cut into pieces of 2 cm in length, followed by digestion in Dulbecco's Modified Eagle's Medium (ZB10, see Table 2) supplemented with 1 mg/mL pronase , 10 µg/mL DNase I, 100 U/mL penicillin, 100 µg/mL streptomycin, 50 µg/mL gentamicin, 1.25 µg/mL amphotericin B, and 2 µg/mL fluconazol for 48 h at 4 °C with gentle shaking. The epithelial cells were harvested by scratching the inside of the dissected bronchia with a scalpel following an expansion in collagen type I coated cell culture flasks with PneumaCult-Ex medium at 37°C and 5 % CO_2 until they reached 70-90 % confluency. The cells were washed with PBS one day after seeding and were finally detached using TrypLE (see 3.3). Detached cells were then resuspended in Ham's F12 nutrient mix (see 3.2), and an equal volume of freezing medium (see 3.2) was slowly (ca. 0.5 ml/3 s) added while keeping cells at 4°C. Aliquots of 4 x 10^6 cells per vial (2 ml) were frozen overnight at -80°C in a CoolCell (see 3.3), then transferred to liquid nitrogen for long-term storage.

Cells were defrosted in a 37°C water bath, transferred to a 15 ml tube and 10 ml of Ham's F12 nutrient mix was gradually added, prior to a centrifugation step (500 g, 5 min). Pelleted cells were resuspended in PneumaCult-Ex medium and expanded in collagen I-coated flasks as described above. For differentiation, 5 x 10^4 cells were transferred to collagen IV-coated cell culture inserts (0.33 cm2, polyethylenterephtalate [PET] membrane, 0.4 µm pore size). The cells were incubated at 37°C and 5 % CO_2 with PneumaCult-Ex medium at the basal and apical sites of the membrane until they reached confluency. Then, the apical medium was removed and the basal medium was exchanged to PneumaCult-ALI medium. The cells were cultured under ALI conditions at 37°C and 5 % CO_2 for four weeks, until they reached full mucociliary differentiation. The basal media was exchanged every 2-3 days and the cell surface was washed once per week with HBSS. All used solutions and buffers are listed in Table 3 (see 3.3).

4.2. Bacteriological methods

4.2.1. Cultivation of *E. coli*

Escherichia coli (*E. coli*, see 3.12) is a gram-negative bacterium first described by Theodor Escherich in 1885. The 1922 isolated *E. coli* K12 strain lacks most pathogenic factors (Ijperen et al., 2002). Therefore, *E. coli* K12 and different derivatives like XL1 blue are considered safe to use in the laboratory environment.

For exponential growth, the bacteria were grown in a liquid LB medium (see 3.4) in an orbital shaker at 37°C and 200 rpm overnight. For colony selection *E. coli* were plated on agar plates and incubated at 37°C overnight (LB medium + 1.5 % bacteriological grade agar). Plasmid transformed (see 4.2.3) *E. coli* was grown in LB medium supplemented with 100 µg/ml ampicillin to select for plasmid containing bacteria. All used plasmids carried the ampicillin resistance gene (see 3.10).

4.2.2. Preparation of chemically competent *E. coli*

Bacterium suspension buffer: 15 % (v/v) glycerin, 60 mM $CaCl_2$, 10 mM PIPES (pH 7.1), in ddH_2O

Uptake of DNA by *E. coli* can be induced by $CaCl_2$. The positively-charged calcium ions neutralize the charge repulsion of the membrane and, together with a subsequent heat shock, favor the uptake of DNA (Mandel and Higa, 1970).

For this purpose, 100 ml LB^{++} (see 3.4) were inoculated with 1 ml of a 5 ml *E. coli* overnight culture (see 4.2.1) and incubated at 37°C and 200 rpm until an optical density (OD600) of 0.6 was reached. Afterwards, the cells were pelleted (1800 g, 10 min, 4°C), the supernatant discarded, the cells resuspended in 25 ml of bacterium suspension buffer, and cooled on ice for 40 min. After another pelleting step (1800 g, 10 min, 4°C) the bacteria were resuspended in 5 ml of bacterium suspension buffer and incubated on ice for another 1-3 h. Aliquots of 50 µl were stored at -80°C.

4.2.3. Transformation of plasmid DNA into competent *E. coli*

For the transformation of plasmid DNA into chemically competent *E. coli* (see 4.2.2), 5 µl of a Hot Fusion product (see 4.4.8), or 10 ng of purified plasmid DNA were mixed with 50 µl competent *E. coli* culture (slowly thawed at RT) and incubated on ice for 20 min. After a 1-minute heat shock at 42°C and a 5 minute incubation on ice, 200 µl LB^{++} (see 3.4) were added to the cells followed by a 1 h incubation at 37°C and 750 rpm on a thermomixer. Transformation of plasmid DNA assembled via Hot Fusion was carried out with 300 µl LB^{++}. For plasmid-DNA midipreparation (see 4.4.2), 100 µl of the bacteria suspension were used to inoculate 50 ml LB medium supplemented with ampicillin and cultured as described earlier (see 4.2.1). Bacteria transformed with plasmid-DNA for colony selection were plated (150 µl) on LB agar plates supplemented with ampicillin (see 3.5).

4.3. Virological methods

4.3.1. Rescue of recombinant CedPV

The virus rescue is based on a reverse genetic system where the full-length virus cDNA is transcribed to antigenomic RNA via the T7 RNA-Polymerase and a RNP is formed in presence of the CedPV-N, P and L. Initial RNP-formation, replication and transcription are mediated by plasmid expressed N, P, and L proteins after co-transfection with full-length cDNA plasmid (see 1.1.5). So-called helper plasmids for N, P, and L protein expression either mediate virus protein expression through T7-RNA-Polymerase or

cellular RNA-Polymerase II controlled promoters (Martin et al., 2006; Schnell et al., 1994). Here, pCAGGS based helper plasmids (pCAGGS-CedPV-N, -P, -L) promoting efficient transcription by the cellular polymerase were used.

For virus rescue, 3 x 10^5 BSR-T7/5 cells/well were seeded in 6-well cell culture plates. After overnight cultivation, the cells were transfected with Lipofectamine 2000 (see 4.1.2). To this end, 3.5 µg full-length cDNA plasmid, 1.25 µg of pCAGGS-CedPV-N, 0.8 µg of pCAGGS-CedPV-P and 0.4 µg of pCAGGS-CedPV-L were co-transfected. After 24 h incubation at 37°C and 5 % CO_2, the cells were scraped off the 6-well cell culture plate with a cell scraper and the cells were transferred together with the media into a T-25 flask and filled up to 5 ml with fresh media (ZB23, 3.2). The cells were then incubated at 37°C and 5 % CO_2 for further 4 - 6 days, with medium exchanges every 2 days. First syncytia were observed microscopically (Nikon eclipse TS100, 10×/0.25 Ph1 Apodized Dark Low (ADL)) 3-4 days after the transfer to T-25 flasks, indicating a successful rescue. When 70-90 % syncytia were formed, the supernatant was transferred to a 15 ml reaction tube and cell detritus was pelleted by centrifugation for 10 min at 4000 g. The cleared supernatant was transferred to a T-75 flask with 3 x 10^6 BSR-T7/5 cells. In parallel, 100 µl of the supernatant were added to 3 x 10^5 BSR-T7/5 cells in a Ø = 3.5 cm well of a 6-well cell culture plate. Two days later, the 6-well cell culture plate was fixed with 4 % paraformaldehyde (PFA, in PBS), immunostained (see 4.5.1) for viral CedPV N/P proteins and screened for the presence of infected cells using a fluorescence microscope (see 4.5.3). The cells in the T-75 flask were cultured up to 4 days until syncytia indicated an almost complete infection of the cell monolayer. Then, the supernatant was clarified from debris via centrifugation (10 min, 4000 g), and 1 ml aliquots were stored at -80°C.

4.3.2. CedPV titration

For titration of the infectious CedPV titres, a plaque assay was performed, in which end-point dilutions of the virus solution were added to cells. Strong syncytia formation of BSR-T7/5 and Vero cells resulted in visible plaques, thus allowing plaque counting and calculation of plaque forming units (pfu)/ml. In contrast, syncytia formation in A549 cells was much less observed and plaques were not detected. Therefore, CedPV infection of A549 cells was determined by immunofluorescence staining. Accordingly, the infectious titer was calculated as focus forming units (ffu)/ml.

For infectious virus titration, 2 × 10^5 cells were seeded in a Ø = 2.2 cm well of a 12-well cell culture plate at day 1 prior to infection. Cells were microscopically checked for confluency. Then, the cells were washed once with sterile PBS, and 100 µl of titration medium (see 3.2) were added per well. A triplicate of a tenfold serial dilution of the virus in titration medium (10^1 - 10^6) was performed. Cells were infected with 200 µl/well of each dilution and incubated for 1 h at 37°C and 5 % CO_2. Every 20 min the plates were slightly tilted in all directions to support virus distribution. Cells were then washed

twice with sterile PBS prior the addition of 1.5 ml overlay medium (see 3.2). After incubation of BSR-T7/5 cells for 4 days and Vero/A549 cells for 5 days at 37°C and 5 % CO_2, the medium was removed and the cells were washed once with PBS, before fixation with 4 % PFA (in PBS) for 1 h at RT. PFA was discarded and the cells were washed three times with PBS. Afterwards, BSR-T7/5 and Vero cells were stained with crystal violet (CV, w/v: 1 % CV in 70 % ethanol)) by incubation with CV for at least 2 h at RT. The CV was gently removed with water, and the infectious CedPV titer was determined by plaque counting and calculation of the pfu/ml considering the inoculum amount and the dilution factor. For titration of CedPV titers on A549 cells, G protein was immunostained (see 4.5.1) and ffu/ml was calculated.

Formula for the calculation of "pfu/ml and ffu/ml"

pfu/ml or ffu/ml = plaque or foci count / (dilution × inoculum volume in ml)

4.3.3. Preparation of CedPV stocks

For virus stock generation, 3 x 10^6 BSR-T7/5 cells were infected in a T-75 flask with CedPV at an MOI of 0.01 in a total volume of 12 ml medium (ZB23, see 3.2). The infected cells were incubated at 37°C and 5 % CO_2. Two days after infection, the supernatant was collected and cell debris was removed by centrifugation (10 min, 4000 g). Cleared supernatant was stored as 1 ml aliquots at -80°C.

4.3.4. NiV titration of ALI culture samples

NiV titration was carried out by Dr. Sandra Diederich and Dr. Kerstin Fischer in the BSL-4 facility of the Friedrich-Loeffler-Institut (FLI, Isle of Riems). Samples of apically released virus were generated by adding 200 µl of sterile PBS to the apical "air" side of the BEC-ALI cultures. After 30 min incubation time at 37°C and 5 % CO_2, PBS was removed for virus titration. Basally released virus was quantified by titration of basal medium samples. All samples were frozen at -80°C prior to titration on Vero76 cells. Serial dilutions and infections were performed as described above for CedPV (see 4.3.2). In contrast to the CedPV titration protocol, the inoculum was removed after 1 h of incubation and 2 ml of a 1:1 mix of ZB5 + 2.5 % FCS and 2 % Carboxymethylcellulose (medium viscosity, Sigma Chemical Co.) were added. The cells were further incubated for 5 days, after which the overlay was removed and the cells were fixed with 10 % formalin for 1 h at RT. Formalin was discarded and the cells were washed three times with PBS prior to staining with CV for 15 min at RT. CV was gently removed with water, and the titer (pfu/ml) was determined as described above (see 4.3.2).

4.3.5. CedPV growth curves

To determine CedPV replication kinetics, growth curves were generated. To this end, 1 × 10^6 BSR-T7/5, A549 or Vero cells (see 3.11) were infected in suspension at an MOI of 0.01 in a total volume of 8 ml medium. The infection was performed with a roller mixer for 1 h at RT. To remove non-cell bound

virus, the cells were afterwards washed three times by pelleting (1500 g, 5 min) and resuspending them in 8 ml of their respective cell culture medium (see 3.2). Subsequently, the cells were pelleted again (1500 g, 5 min). One ml of the supernatant was transferred to a reaction tube and stored at -80°C (0 dpi value). The pellet was resuspended in 8.1 ml of cell culture media and 100 µl were transferred to a well of a 96-well cell culture plate for infection control by immunostaining (see 4.5.1). The remaining cell suspension was transferred to a T-25 cell culture flask and incubated at 37°C and 5 % CO_2. Supernatant samples (0.5 ml) were taken at 16 hpi, 24 hpi, 48 hpi, 72 hpi, and 96 hpi. Cell debris was removed via centrifugation (1500 g, 5 min) and the samples were stored at -80°C. Each removed sample was substituted by 500 µl fresh cell culture medium. The virus titers were determined by virus titration (see 4.3.2).

4.3.6. Infection of BEC cultures with NiV

Infection of BEC-ALI cultures were carried out by Dr. Sandra Diederich and Dr. Kerstin Fischer in the BSL-4 facility of the Friedrich-Loeffler-Institut (FLI, Isle of Riems). BEC-ALI cultures were prepared in a BSL-2 facility, as described earlier (4.1.3), before they were transferred to a BSL-4 facility for NiV infection. The BEC-ALI cultures were washed three times with sterile PBS prior to the infection with 2 × 10^6 infectious units/well. The infection was carried out by adding virus containing medium (maximum volume of 350 µl) to the apical side of the transwells. After 1 h incubation with the inoculum at 37°C and 5 % CO_2, the cells were washed three times with PBS, and the medium in the basal compartment was replaced by fresh medium. Non-infected mock controls were processed in parallel in a BSL-2 lab. Basal medium was exchanged every 2-3 days.

For the infection of undifferentiated BECs, µ-Slide 8-well (Ibidi) were coated with collagen IV and expanded BECs were seeded (0.8 × 10^5 cells/well). After 24 h incubation at 37°C and 5 % CO_2 the cells were infected with NiV at an MOI of 4 by removing the medium and adding 350 µl inoculum for 1 h at 37°C and 5 % CO_2. Subsequently, the cells were washed three times with PBS and incubated with PneumaCultEx medium for 5 days at 37°C and 5 % CO_2.

Samples for immunofluorescence staining were collected by removing the medium and fixation for 24 h with 4 % PFA prior to the transfer to the BSL-2 facility. After transfer, the samples were post-fixed for another 24 h period for biosafety reasons. After three washing steps with PBS, the samples were stored in PBS at 4°C until immunofluorescence staining (see 4.5.2).

4.4. Molecular biological methods

4.4.1. Plasmid-DNA minipreparation from *E. coli*

Flexi I: 100 mM Tris-HCl (pH 7.5), 10 mM EDTA (pH 8), 100 µg/ml RNase A, in ddH_2O

Flexi II: 200 mM NaOH, 1 % SDS, in ddH_2O

Flexi III: 3 M potassium acetate, pH 5.75 (adjustment with acetic acid), in ddH_2O

Preparation of plasmid-DNA from *E. coli* was performed based on the principle of alkaline lysis (Birnboim and Doly, 1979). Both, high molecular weight chromosomal DNA and circular plasmid DNA are denatured by NaOH. Upon neutralization with potassium acetate, the chromosomal DNA only partially renatures and becomes insoluble, while the plasmid DNA renatures to a dsDNA and stays soluble in the aqueous phase, from which it can be precipitated by isopropyl alcohol precipitation.

For plasmid-DNA minipreparation, 1.5 ml LB medium supplemented with 100 µg/ml ampicillin were inoculated with *E. coli* cultures from LB agar plates (see 4.2.3) and were incubated overnight at 37°C and 750 rpm in a thermomixer. The cultures were pelleted (1 min, 4500g, RT) and resuspended in 200 µl of Flexi I buffer. Subsequently, 200 µl of Flexi II buffer was added and thoroughly mixed prior to addition of 200 µl of Flexi III buffer. The sample was inverted 3 - 5 times and incubated on ice for 20 - 60 min. To remove chromosomal DNA and precipitated proteins, the sample was centrifuged for 10 min at 16100 g, and the supernatant was transferred into a new reaction tube. The precipitation of plasmid-DNA from the supernatant was initiated by adding 400 µl of isopropyl alcohol for 10 min at RT. The plasmid-DNA was pelleted by centrifugation (10 min, 16100 g). After removal of the supernatant, the pellet was washed with 1 ml of 70 % ethanol followed by another centrifugation for 5 min at 16100 g. The supernatant was discarded and the pellet dried at 56°C. Finally, the pellet was dissolved in 50 µl of ultrapure water. To verify the identity of the extracted plasmid-DNA, the DNA was digested enzymatically with the respective restriction endonucleases (see 4.4.4). Resulting DNA-fragments were examined by agarose gel electrophoresis (see 4.4.5) and verified plasmid DNA were sequenced (see 4.4.9).

4.4.2. Plasmid-DNA midipreparation from *E. coli*

Extraction of plasmid-DNA from 50 ml *E. coli* overnight cultures (see 4.2.3) was carried out with the QIAfilter Plasmid Midi Kit (see 3.15), according to the manufacturer's instructions. The purified plasmid DNA was dissolved in 100 µl ddH_2O and the DNA concentrations were determined by spectrophotometric analysis (see 4.4.3). The identity of the extracted plasmid-DNA was verified as described earlier (see 4.4.1).

4.4.3. Spectrophotometric nucleic acid quantification

Spectrophotometric quantification of nucleic acids is based on ultraviolet light absorption. The nucleic acid concentration is proportional to the light absorbed. Due to the aromatic ring structure of purine and pyrimidine bases, nucleic acids have the absorption at a maximum of 260 nm (E_{260}), whereas proteins have their absorption maximum at 280 nm (E_{280}), and organic compounds at 230 nm (E_{230}).

Concentration of DNA or RNA in a given volume is calculated using the Beer-Lambert Law (see below). An optical density (OD) of E_{260}= 1 corresponds to a concentration of 50 µg/ml for dsDNA, and 40 µg/ml for RNA. Purity of nucleic acid samples can be estimated by analysing quotients of $E_{260}/_{280}$ as well as E_{260}/E_{230}. Pure DNA and RNA samples possess a coefficient ≥ 1.8. DNA samples were measured with a NanoPhotometer P330 (Implem), whereas RNA samples were measured with a nanodrop ND-1000 (peqlab). All samples were analyzed, undiluted and ultrapure water served as a reference value. Concentrations were calculated with the following formula:

$c = E_{260} \times f \times \varepsilon \times d$

c	= concentration in µg/ml		
E260	= absorption at λ = 260 nm		
ε	= absorption coefficient:	dsDNA	= 50 µg/ (ml × cm)
		RNA	= 40 µg/ (ml × cm)
d	= thickness in cm		

4.4.4. Restriction endonuclease digest of DNA

Restriction endonucleases recognize and cleave specific DNA sequences. They catalyze the hydrolysis of the bond between adjacent nucleotides resulting in two kinds of ends: the blunt end without an overhang and the sticky ends with an overhang. Four different types of restriction enzymes are known. In this work, only type II restriction endonucleases (Smith and Welcox, 1970) were used. These enzymes cleave DNA at defined positions, do not possess an intrinsic methyltransferase activity and do not need ATP for their enzyme activity.

The restriction endonuclease digests were performed according to the manufacturer's instruction. Briefly, plasmid DNA, 10 x enzyme buffer, restriction enzyme (10 units) and water were mixed in a reaction tube and incubated at 37°C for 2 h. To digest DNA, 1 µl from plasmid minipreparation or 1 µg from midipreparations was used. Resulting DNA-fragments were examined by agarose gel electrophoresis (see 4.4.5).

4.4.5. Agarose gel electrophoresis

50 × TAE buffer:	2 M Tris, 0.25 M sodium acetate trihydrate, 50 mM EDTA, in ddH_2O
Agarose gel (0.7 %):	0.7 % (w/v) agarose, 0.001 % (v/v) ethidium bromide (10mg/ml in ddH_2O), in 1 × TAE buffer
10 × loading buffer:	30 % (w/v) glycerin, 0.25 % (w/v) bromophenol blue, 0.25 % (w/v) xylene cyanol, in ddH_2O

Agarose gel electrophoresis is used to separate linear DNA fragments by their respective size. Negatively-charged DNA molecules migrate to the positive pole through a porous matrix of agarose when an electric field is applied. The migration time depends on the length of the DNA molecules, the pore size, and the electric field. Smaller fragments travel faster through the matrix than larger fragments. The pore size depends on the agarose concentration in the gel. For large fragments, a lower amount of agarose is suggested, and for small fragments, a higher amount of agarose. In this study, gels with 0.7 % (w/v) agarose were used.

The required amount of agarose was dissolved in 1 × TAE buffer by heating in a microwave. Then, 0.2 µg/ml ethidium bromide (stock solution 10 mg/ml in ddH_2O) was added. The liquid agarose solution was transferred to a horizontal gel chamber with a comb and polymerized at room temperature. Appropriate amounts of 10 × loading buffer were mixed with 5 µl of the sample, loaded on an agarose gel, and a constant voltage of 120 V was applied for 30 min. A DNA ladder allowed to estimate the length of the DNA-fragments (see 3.6). DNA-fragments in the gel were visualized with ethidium bromide, a fluorescence dye which intercalates in DNA. It can be visualized with the excitation of a wavelength of 302 nm to detect the DNA-fragments in the gel by a gel imaging system (Gel doc, Bio-Rad).

4.4.6. Purification of DNA-fragments from agarose gels

Separated DNA-fragments can be extracted from agarose gels to obtain purified DNA for downstream analysis, almost free of contaminants such as salt, enzymes and undesired DNA-fragments. Gel extractions were performed with the QIAquick gel Extraction Kit (see 3.15), according to the manufacturer's instructions. Briefly, the DNA-fragments bands were visualized with UV-light, excised with a scalpel, transferred to a reaction tube and processed as described in the kit's protocol. The DNA-fragments were eluted with 20 µl ultrapure water.

4.4.7. Polymerase chain reaction (PCR)

The polymerase chain reaction (PCR) is an *in vitro* method used to amplify small amounts of DNA in a short period of time, invented in the early 1980s by Kary B. Mullis (Mullis et al., 1986). For the amplification process, the PCR relies on a DNA polymerase, template DNA, free nucleotides (dNTPs) and specific pairs of oligonucleotides (see 3.8). Amplification of DNA-fragments occurs in a tripartite

reaction, facilitated by a thermocycler. DNA is denatured by heat to provide a single-stranded template for the annealing of primers to their complementary sequence. Afterwards, the polymerase extends the primers to synthesize new strands of DNA.

Phusion® Hot Start Flex DNA Polymerase (see 3.7) was used with the detailed reaction setup and thermocycling protocol listed below. The correct annealing temperature for the different primer pairs were calculated with the Tm Calculator from New England BioLabs. Amplified DNA-fragments were separated by agarose gel electrophoresis (see 4.4.5), and DNA-fragments were extracted (see 4.4.6).

Reaction Mix		Temperature cycles			
x µl	DNA template (100 ng)	Denaturation	98°C	30 sec	
10 µl	5 × Phusion HF buffer	Denaturation	98°C	10 sec	30 cycles
1 µl	10 mM dNTPs	Annealing	x°C	15 sec	
2.5 µl	10 pmol/µl forward primer	Elongation	72°C	30 sec/kb	
2.5 µl	10 pmol/ µl reverse primer	Final elongation	72°C	10 min	
1.5 µl	DMSO	Hold	4°C	∞	
0.5 µl	Phusion DNA Polymerase (1 unit)				
ad 50 µl	ddH_2O				

4.4.8. Hot Fusion

5 × Pre-assembly buffer: 0.5 M Tris (pH 7.5), 50 mM $MgCl_2$, 1mM of each dNTP, 50 mM DTT, 25 % (w/v) PEG-8000, in ddH_2O

2 × Hot Fusion reaction mix: 160 µl 5x Pre-assembly buffer, 0.3 µl 10U/µl T5 Exonuclease, 10 µl 2 U/µl Phusion DNA polymerase, in 230 µl ddH_2O

In 2014, Changlin Fu and colleagues developed an efficient method to clone one or several DNA-fragments into plasmid vectors without the use of ligases, such as the T4 DNA ligase (Fu et al., 2014). One of its greatest benefits is that there are no necessities regarding the availability of restriction enzyme recognition sites. Briefly, linear DNA-fragments are combined through terminal, 17-30 bp long homologous regions. In the Hot Fusion Reaction, T5 Exonuclease (see 3.7) removes nucleotides in 5' to 3' direction of the linear dsDNA-fragments, enabling the remaining 3'-ssDNA-overhangs of the DNA-fragments to hybridize. DNA-synthesis by Phusion® Hot Start Flex DNA Polymerase fills gaps generated by the T5 Exonuclease, resulting in a circular plasmid that is replicated in *E. coli* after transformation.

With specific primers (see 3.8), insert and plasmid vector DNA-fragments with terminal overlapping regions were amplified by PCR (see 4.4.7). Prior to Hot Fusion, the amplified DNA-fragments were

verified by agarose gel electrophoresis (see 4.4.5), DpnI digested (see 4.4.4) and gel purified (see 4.4.6). In the Hot Fusion reaction, the plasmid vector and insert DNA-fragments were combined in a molar ratio of 3:1, together with 10 µl 2 × Hot Fusion reaction mix in a total volume of 20 µl. The reaction was performed in a thermocycler with 1 h incubation at 50°C and subsequent cooling to 20°C (0.1°C/sec). 5 µl of the reaction mix were then transformed into *E. coli* and ampicillin resistant clones were selected on LB-agar plates (see 4.2.3).

4.4.9. DNA-sequencing

DNA-sequencing was performed with the LightRun Tube service from Eurofins Genomics, based on the classic chain-termination method by Sanger (Sanger et al., 1977). For sequencing 5 µL of plasmid DNA (100 ng/µl) were mixed with 5 µl primer (5 pmol/µl) and sent to Eurofins Genomics. Sequence analysis was performed with GeneiousPrime (see 3.16).

4.4.10. RNA extraction

Most available RNA extraction kits are based on a bind-wash-elute process with silica membranes in the presence of chaotropic salts. Proteins and polysaccharides bind poorly to the membranes, and residual traces are removed with alcohol-based wash steps. For quantification of viral RNA and cytokine mRNAs in BEC-ALI cultures, the cultures were washed three times with PBS prior to cell lysis in TriFAST peqGOLD (VWR). 200 µl Chloroform were added per 1 ml of lysed sample. The sample was mixed for 15 s followed by 10 min incubation at RT and a centrifugation step for 10 min at 13000 rpm and 4°C. The upper aqueous phase was transferred to a new sterile reaction tube and 600 µl of ethanol were added. 700 µl of the mixed sample was transferred on a RNeasy spin column and it was proceeded as described in the manufacturer's instructions of the RNeasy kit (see 3.15).

Afterwards, remaining DNA in the extracted RNA was removed by digestion with DNase I from the TURBO DNA-free kit (see 3.15) with the provided protocol. Briefly, up to 10 µg RNA were digested with 1 µl DNase in a 50 µl reaction setup for 30 min at 37°C. DNase was deactivated with the supplied inactivation reagent, the sample was centrifuged and the supernatant was stored as 10 µl aliquots at -80°C. Before downstream analysis, the RNA concentration was determined by spectrophotometric analysis (see 4.4.3).

4.4.11. Reverse transcription and real-time PCR (qPCR)

In order to perform qPCR, RNA first has to be reversely transcribed into complementary DNA (cDNA). This is performed by reverse transcriptase's (RT) discovered by Howard Temin and David Baltimore (Temin and Mizutani, 1970). The resulting cDNA can then be used for quantification by qPCR. The quantification is based on fluorescence dyes, like SYBR green, which intercalates with dsDNA during the amplification. The amount of fluorescence correlates with the amount of dsDNA, and can be detected and quantified in each PCR cycle.

Reverse transcription was performed with 500 ng of purified RNA using the RevertAid First Strand cDNA Synthesis Kit (see 3.15) and oligo $(dt)_{18}$ primer, binding to the poly(A) tail of mRNAs, according to the supplier's instructions. For qPCR, 0.7 µl of the RT reaction were used. qPCR was performed with the PowerUp SYBR green Master mix (see 3.15) according to the supplier's instructions (standard cycling mode (primer $T_m \geq 60°C$) with α-tubulin, host cytokine and NiV-N mRNA specific primers (see 3.8).

Cycle threshold (Ct) values were normalized to α-tubulin expression (ΔCt), and differences in the RNA expression were calculated with the $2^{-\Delta\Delta Ct}$ method (fold change over mock, (Livak and Schmittgen, 2001)). For quantification of relative viral mRNA levels in PBEC-ALI cultures with NiV N gene primers, the ΔCt values were subtracted from the ΔCt mock value (ΔCt mock – ΔCt). Data were acquired with a C1000 Thermal Cycler (BioRad), the CFX96 Real-Time System (BioRad) and with the Bio-Rad CFX Maestro 1.1 (v.4.1.2433.1219) software.

Formula for the calculation of "fold gene expression"

ΔCt = Ct (gene of interest) − Ct (housekeeping gene)

ΔΔCt = ΔCt (infected) – ΔCt (mock control)

Fold gene expression = $2^{-\Delta\Delta CT}$

Temperature cycles

Uracil-DNA glycosylase (UDG) activation	50°C	2 min	
Dual-Lock DNA polymerase	95°C	2 min	
Denature	95°C	15 sec	40 cycles
Anneal/extend	60°C	1 min	

4.5. Immunofluorescence staining and microscopy

4.5.1. Indirect immunofluorescence staining

Immunofluorescence staining is a method that permits the visualization of components in any tissue or cells. Principally, immunostaining can be divided into two categories: Indirect or direct, depending on whether the fluorophore is conjugated with the primary or the secondary antibody. With the help of several fluorophores and antibodies, it is possible to label different antigens in the same tissue.

To analyze the intracellular localization of proteins, cells were seeded either in cell culture dishes with poly-L lysin coated (1:100 in ddH_2O for 20 min) 18 mm × 18 mm coverslips or, for undifferentiated BEC, in µ-Slide 8-well chamber slides coated with Collagen type I. These cells were either transfected with plasmids (see 4.1.2), or infected with virus (see 4.3.1 and 4.3.6) prior to fixation with 4 % PFA (in PBS) for 20 min at RT. Cells infected with NiV were fixed as described earlier (see 4.3.6). The cells were washed three times with PBS and were permeabilized with 0.2 % Triton X-100 (in PBS) for 20 min at RT. Unspecific binding sites were blocked with 10 % donkey serum and 0.3 M glycine in PBS-T (0.1 % Tween 20 in PBS) for 30 min at RT. Antibodies were diluted with 1 % donkey serum in PBS-T with their respective dilution. Primary antibodies (see 3.14.1) were applied for 2 h at RT, followed by three washing steps with PBS and the incubation with fluorophore-labelled secondary antibodies (see 3.14.2), for 1 h at RT. Nuclei were counterstained with Hoechst 33342 ((see 3.14.3), 1:20000 in PBS) for 10 min at RT. Coverslips were washed two times with PBS and once with ddH_2O, prior to mounting onto slides with a drop of mounting medium (Ibidi). Coverslips were fixed with conventional nail polish. Chamber slides were washed two times with PBS and once with ddH_2O before addition of 200 µl ProLong™ Glass AntiFade Mountant. Samples had to cure for at least 18 h to achieve refractive index of 1.52. Afterwards, the samples were analyzed with a confocal laser scanning microscope or a Leica THUNDER Imager (see 4.5.3).

4.5.2. Indirect immunofluorescence staining of NiV-infected BEC-ALI cells

Immunofluorescence staining for whole cell culture insert membranes was carried out as described above (see 4.5.1). After the Hoechst staining and the washing, the membranes were carefully removed from the cell culture inserts using a scalpel. The membranes were then embedded with ProLong™ Glass AntiFade Mountant and covered with a 12-mm round coverslip. Samples cured for at least 18 h and were analyzed with a confocal laser scanning microscope or a conventional fluorescence microscope (see 4.5.3).

To prepare cross sections the membranes of BEC-ALI cultures were carefully removed from the cell culture inserts with a scalpel, were paraffin embedded and cut into 5 µm slices with a microm HM 430 E (Thermo Fisher). Sections were permeabilized with 0.2 % Triton X-100 (in PBS; PBST) for 15 min at RT, followed by a blocking step with 5 % donkey serum (in PBST) and the primary antibody incubation

in 1 % donkey serum (in PBST) for 1 h at RT. Subsequently, the sections were washed three times with PBS and secondary antibodies (in PBST with 1 % donkey serum) were applied for 1 h at RT. The nuclei were stained with Hoechst 33342 (see 3.14.3, 1:20000 in PBS) for 10 min at RT. Cross sections were embedded with ProLong™ Glass AntiFade Mountant and covered with a 12-mm round coverslip. The samples were analyzed with a confocal laser scanning microscope or a conventional fluorescence microscope (see 4.5.3).

4.5.3. Indirect immunofluorescence microscopy

Large cross section images (Figure 13), membrane overviews (Figure 10), figures for automated cell counting (see 4.5.4) and phase contrast images were acquired with a Leica THUNDER imager DMi8 and LAS X (v3.7.423463) software. Fluorescence was either detected with a 10×/0.12 dry N PLAN objective or a 20×/0.40 dry HC PL FLUOTAR L objective. All other images were acquired using a confocal laser-scanning microscope (CLSM, Leica DMI6000 TCS SP5) and LAS AF (v2.7.3.9723) software. Confocal images were recorded by sequential scans of different channels at a pinhole diameter of 1 Airy unit and a z-step size of 0.35 µm using a 63x/1.40 oil immersion HCX PL Apo objective. Within an experiment, all detection parameters and laser intensities remained constant, and images acquired by CLSM are displayed as maximum intensity projections. All images were processed with the software package Fiji 1.53c (Schindelin et al., 2012).

4.5.4. Automated cell counting pipeline

For automated cell counting, cells were fixed for 20 min with 4 % PFA (in PBS) prior to immunofluorescence staining for CedPV G (4.5.1). The plates were scanned in a motorized Leica THUNDER imager DMi8 by acquisition of six field of views per well using a 10×/0.12 dry N PLAN objective and the LAS X (v3.7.423463) software. To remove background noise and enhance contrasts instant computational clearing mode (THUNDER), a background subtraction method, was used. The subsequent analysis was carried out with the Arivis-Vision 4D software (3.16) to establish a counting pipeline using the Arvis analysis pipeline tool. Briefly, both channels (nuclei and virus antigen immunofluorescence) were denoised (Discrete Gaussian, 5 µm) followed by a threshold setting (Thresholder: Li). To identify nuclei (25 µm, probability threshold: 5 %, split sensitivity: 85 %) and virus signals (50 µm, threshold: 100, split sensitivity: 25 %) the blob finder was used. Afterwards, the signals of the nuclei channel (> 0 μm^2, < 2000 μm^2) and the CedPV G channel (200 pm, > 20 µm) were segmented. The number of nuclei segments within segments generated by viral immunofluorescence were counted, resulting in the number of infected cells. Segments from nuclei signal outside the viral immunofluorescence segments treated as uninfected. The percentage of infected cells was calculated and cell numbers were used as a measure for inhibitory effects of siRNAs to cell viability.

4.6. Mass spectrometry

4.6.1. Preparation and measurement of MS samples

Shotgun proteome analysis was performed in collaboration with the lab of Dr. Axel Karger (FLI, Isle of Riems). Protein was extracted with TriFast peqGOLD according to the manufacturer's protocol. Protein extracts were solubilized by incubation in 200 µl 20 mM Tris-HCL, pH 7.4, 50 mM DTT, 1 % SDS at 100°C for 10 min. After centrifugation (10 min, 10000 g, 4°C), the supernatants were collected and protein concentrations were determined densitometrically with coomassie-stained SDS-polyacrylamide gels (Neuhoff et al., 1988). Aliquots containing 150 µg were digested with trypsin (Promega) using the FASP (filter-aided sample preparation) protocol (Wisniewski et al., 2009) with an enzyme to substrate ratio of 1:50 (w/w) and 30 kDa cut-off ultrafilters (Vivacon 500, Satorius). Subsequently, the peptides were desalted using Pierce C18 tips (Thermo Fisher) according to the manufacturer's protocol, vacuum dried, and resuspended in 0.1 % formic acid (FA, in ddH_2O), prior to the analysis on a nanoElute/timsTOF Pro (Bruker) MS platform.

For the purpose of analysis, 1 µg of peptides were separated by nano reversed phase liquid chromatography using a nanoElute chromatography station, together with an IonOpticks Aurora column (25 cm x 75 µm inside diameter, 1.6 µm particle size, C18 stationary phase) at a temperature of 40°C and a flow rate of 0.4 uL/min. Subsequently, peptides were eluted in a binary gradient formed by solvent A (0.1 % FA in ddH2O) and solvent B (0.1 % in acetonitrile) with the following parameters: from 2 % to 16 % solvent B (0-60min), 15-24 % solvent B (60-90min), 24 %-34 % solvent B (90 min – 105 min), 35-95 % solvent B (105-107 min) and 95 % solvent B (107-115 min). The TimsTOF Pro instrument was equipped with a CaptiveSpray nano electrospray ion source (Bruker), and was operated in Parallel Accumulation and Serial Fragmentation (PASEF) (Meier et al., 2015) mode using the standard method for proteome analysis (1.1 sec cycle time) recommended by the manufacturer. Mass spectrometry data have been uploaded to the ProteomeXchange Consortium (http://proteomecentral.proteomexchange.org) via the PRIDE partner repository (Perez-Riverol et al., 2019) with the dataset identifier PXD032673 and 10.6019/PXD032673.

4.6.2. Processing and analysis of MS data

Analysis was performed in collaboration with the lab of Dr. Axel Karger (FLI, Isle of Riems). For label free quantification (LFQ) and protein identification, MaxQuant (MQ) version 2.0.2.0 was used (Cox and Mann, 2008; Prianichnikov et al., 2020) with the parameters suggested for a timsTOF instrument (Supplement 3). Analysis was performed using a database containing both NiV (GenBank AF212302) and porcine protein sequences. The latter (S. scrofa version 11.1) were downloaded from the Ensembl repository (Aken et al., 2017).

The false discovery rate (FDR) was set to 1 % for peptides and proteins. Methionine oxidation and N-terminal acetylation were allowed as variable modifications, while the carbamidomethylation of cysteine was set as fixed modification. Trypsin was chosen as a protease and 2 missed cleavage sites were tolerated. The resulting MQ tables were processed using in-house R scripts (version 4.0.3 (R Core Team, 2020); R studio (RStudio Team, 2020)) prior to the analysis in the Perseus version 1.6.15.0 (Tyanova et al., 2016), using the workflow depicted in Supplement 4. Protein identifiers were referenced to genes and enrichment analysis was carried out with the R-package gprofiler2 version 0.2.1 (Kolberg, 2021) Data was visualized with ggplot2 version 3.3.5 (Wickham, 2021). The von Neumann test (von Neumann, 1941) was performed in R with the DescTools package (Andri et mult. al. S, 2021).

Tables combining data from public repositories KEGG (Kyoto Encyclopedia of Genes and Genomes) (Kanehisa and Goto, 2000) and GO (Gene Ontology) (Ashburner et al., 2000), as well as identified proteins and corresponding genes with experimental data (stages of infection, replicates) in Perseus were constructed using in-house R scripts. The KEGG and GO annotations of biological processes (GO:BP) and cellular components (GO:CC) are based on porcine annotations and the human orthologs of the identified porcine genes. Statistical analysis in Perseus was performed with an FDR of 5 % and S0 to 0, or 0.1 for t-tests and Volcano plots, respectively.

Term enrichment analyses were performed as multi query based on up or down regulated differentially expressed genes (DEG) (Supplement 5) using R together with the gProfiler2 package (Kolberg, 2021) or in Cytoscape version 3.9.1 (Shannon et al., 2003) using the Plug-in ClueGO (Bindea et al., 2009). The detailed results can be found in Supplement 6. In-house R-scripts were developed in the Laboratory for Biochemistry and Protein Analysis (IMVZ, FLI).

4.7. Cloning of full length cDNA clones and mutagenesis

4.7.1. Generation of the pt7 CedPV full length

The cDNA plasmid pt7 CedPV coding for the complete CedPV antigenome was generated by assembling synthetic DNA-fragments comprising partial virus genome sequences into the plasmid vector pt7 (see 3.10). All fragments were designed according to the CedPV isolate CG1a complete genome sequence (# NC_025351.1) and were obtained from Eurofins Genomics as linear dsDNA strands dubbed fragment 1 to 4 (each 2000bp long), except for fragment 5 (2806 bp) which was delivered in a pEX-A258 plasmid. Fragments were designed with terminal 30 bp long sequences that overlapped with the respective up-and downs-stream fragments of the vector.

First, the pt7 vector sequence was PCR-amplified from pt7 NiV mini GFP (3479 bp, see 3.10) with the primer pt7_Vec_fw and CeV_VeC_rv to a linear, 2217 kb DNA-fragment. Fragments 1 and 2 were PCR-amplified from the respective synthetic fragments with the primer pairs CedPV_frag_1_fw/CedPV_frag_1_rv and CedPV_frag_2_fw/CedPV_frag2_ov_backbone_rv, respectively. The purified PCR products were assembled by Hot Fusion (see 4.4.8) and the resultant plasmids were amplified in *E. coli* (see 4.2.3). To identify positive clones, plasmid minipreparation (see 4.4.1) following restriction endonuclease digestion (*PvuII* , see 3.7 and 4.4.4) was performed. A linear 6157 kB DNA-fragment was amplified from pt7-fragment 1-2 plasmid with the primers pt7_Vec_fw / CedPV_frag2_rv and was fused with fragment 3, amplified with the primer pair CedPV_frag3_fw / CedPV_frag3_ov_rv by Hot Fusion to yield a pt7-fragment 1-3 plasmid. Afterwards, a linear 8127 bp DNA fragment was amplified from pt7-fragment 1-3 plasmid with the primers pt7_Vec_fw / CedPV_frag3_rv and was fused with fragment 4, amplified with primers CedPV_frag4_fw / CedPV_frag4_ov_rv by Hot Fusion to construct a pt7-fragment 1-4 plasmid. Subsequently, a linear 10097 bp long DNA-fragment was amplified from the pt7-fragment 1-4 plasmid with the primer pairs pt7_Vec_fw / CedPV_frag4_rv and was fused with fragment 5, amplified with the primers Complex_frag_CedPV_fw / CedPV_Complex_ov_rv by Hot Fusion to obtain a pt7-fragment 1-5 plasmid. To complete the construction of the full-length sequence, the 7506 bp long CDS of the L protein was amplified from an expression plasmid with the primers CedPV_LCDS_ov_fw / CedPV_LCDS_ov_rv. This fragment was then fused by Hot Fusion with a linear 12873 bp DNA fragment amplified from the pt7-fragment 1-5 plasmid with the primer pair CedPV_full-length_L_fw / CedPV_full-length_L_rv.

A mutation appeared during the cloning procedure in the viral genome sequence being silent in the P-ORF but non-silent in the C-ORF (pt7 CedPV C-R68K). To remove this mutation the CedPV full length antigenome plasmid was amplified with the primer pair Crep_fw_correct / Crep_rv_correct. The purified PCR product was reassembled by Hot Fusion (see 4.4.8) and the resultant plasmids were amplified in *E. coli* (see 4.2.3).

All sub-clones and the final full length plasmid were identified by enzyme digestion (*PvuII* or *PstI*, see 3.7 and 4.4.4) and the sequence of resultant clones was verified by DNA-sequencing (see 4.4.9). The cloning strategy is summarized in Figure 22. An overview of oligonucleotide sequences is provided in chapter 3.8.

4.7.2. Mutagenesis of the pt7 CedPV full length and reporter gene insertion

Derivatives of the pt7 CedPV full length cDNA plasmid were generated to optimize the analysis workflow described previously (see 4.5.4). Therefore, reporter genes encoding the proteins TurboFP635, nuclear-localizing TurboFP635 (nTurboFP635) and nuclear localizing Bilirubin-inducible fluorescent protein UnaG (nUnaG), were inserted as an extra-cistron between the P and M genes.

For insertion of the nuclear UnaG (nUnaG), the pt7 CedPV full length cDNA plasmid (see 4.7.1) was amplified with the primers Backbone_CedPV_fw_ov / Ced_unaG_insM_rv. The resulting 20434 kb linear DNA fragment was combined by Hot Fusion (see 4.4.8) with a synthetic DNA-fragment comprising three copies of nuclear localization signal (NLS) derived from the SV40 large T antigen (ATGCCAAAGAAGAAGAGAAAGGTAGATCCGAAAAAGAAGAGCAAGGTGGATCCTAAGAAGAAGAGCAAGG TGCAC) N-terminally fused to the UnaG (Kumagai et al., 2013) coding sequence and a CedPV sequence (# NC_025351.1) from position 4326 to 4748.

To insert TurboFP635, the pt7 CedPV full length cDNA plasmid was digested with *XhoI* (see 4.4.4) to generate a linear fragment (19317 bp long). A linear 1034 bp long DNA-fragment was amplified from the pt7 CedPV nUnaG plasmid using the primer pair CedPV_Xho_Muta_fw / CedPV_Kathush_woNLS_rv_ins. Afterwards, the purified DNA-fragments were assembled via Hot Fusion (see 4.4.8) together with a synthetic 1213 bp long genome fragment acquired from Eurofins Genomics comprising the sequence of the TurboFP635 coding sequence and a CedPV sequence (# NC_025351.1) from position 4326 to 4748.

To generate nuclear localizing Katushka the pt7 CedPV full length cDNA plasmid (see 4.7.1) was digested with XhoI and HindIII (see 4.4.4) to obtain a 17775 kb DNA-fragment. Afterwards, pt7 CedPV C-R68K plasmid was amplified with the primer pairs CedPV_Xho_Muta_fw / Ced_unaG_insM_rv to obtain a 1033 bp long DNA-fragment and pt7 CedPV TurboFP635 was amplified with the primer pair trNLS_Kat_fw / CedPV_HindIII_Muta_rv to yield a 2756 bp long fragment. All three DNA-fragments were assembled via Hot Fusion (see 4.4.8).

All final full length plasmids were identified by plasmid minipreparation (see 4.4.1) followed by enzyme digestion (*PvuII* or *XhoI*, see 3.7 and 4.4.4). The sequence of resultant clones was verified by DNA-sequencing (see 4.4.9). An overview of the different constructs is summarized in Figure 28. An overview of oligonucleotide sequences is provided in chapter 3.8.

5. Results

5.1. Analysis of Nipah virus replication in differentiated BEC-ALI cultures

5.1.1. Infection of non-differentiated ferret and pig BEC (FBEC and PBEC)

Pigs serve as an intermediate host for NiV_M which develop severe respiratory symptoms and previous studies demonstrated the susceptibility of non-differentiated pig and human BEC for NiV infection (Sauerhering et al., 2016). However, undifferentiated cells only partially reflecting the actual infection process in the lung. They lack cellular subpopulations resulting in a loss of heterogeneity and cell-cell and cell-matrix interaction (Abbott, 2003). Also, general physiological markers of a respiratory system are missing. Differentiated bronchial epithelial cells can be used to represent *in vivo* biology in an *in vitro* environment as a physiological relevant model to overcome those limitations. However, detailed NiV infection and host response kinetics in differentiated ferret and pig BEC cultures at ALI have not been studied so far. Accordingly, it was an aim of this thesis to characterize NiV replication in fully differentiated PBEC and FBEC ALI-cultures. Primary BEC were prepared from pig and ferret bronchial tissue (see 4.1.3) and the general susceptibility of the prepared cells to NiV infection was confirmed by infection of non-differentiated monolayer cultures (see 4.3.6).

Indeed, by infection of undifferentiated BEC with 2×10^6 infectious units / well (calculated from Vero cell specific titers; see 4.3.4) and immunofluorescence detection of NiV N protein (see 4.5.1) from 1 dpi on, the susceptibility of both PBEC and FBEC was confirmed (Figure 8A). Most cells were infected 1 dpi and almost all cells were NiV N positive 3 dpi (Figure 8B). Notably, infected ferret cells exhibited a strong cytopathic effect (CPE) from day 2 on, visible by fragmentation of the cellular chromatin (Figure 8, arrowhead), while comparable fragmentation was not observed for infected PBEC at that time point. Besides confirmation of susceptibility these data also indicated a higher resilience of PBECs to NiV induced CPE compared to FBECs.

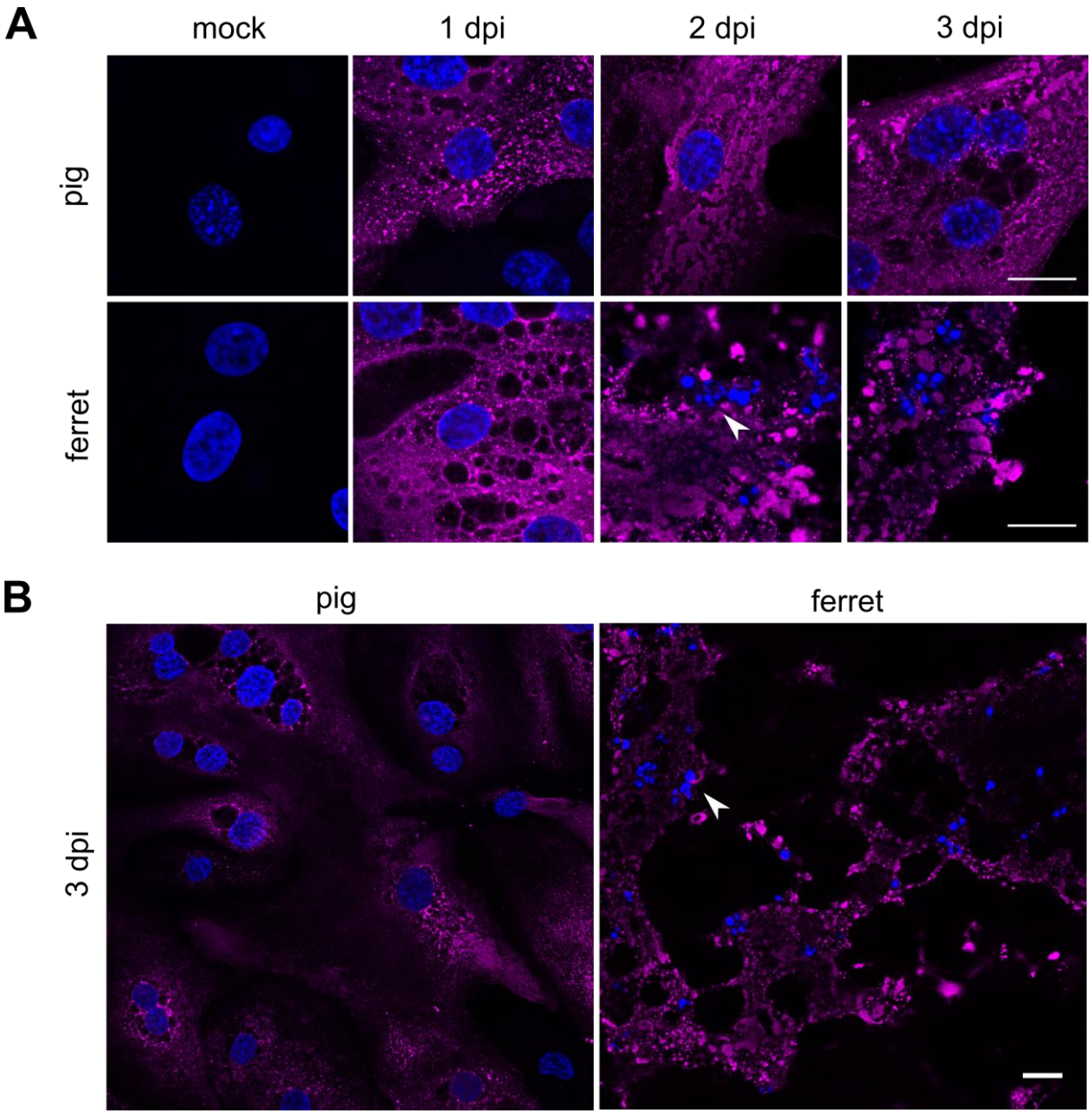

Figure 8: Time course of NiV infection in non-differentiated BECs. (A) Immunostaining of NiV infection in non-differentiated PBEC (pig) and FBEC (ferret) for NiV N (magenta) at 1 dpi, 2 dpi, and 3 dpi. Representative images from two independent experiments with distinct donor animals are shown for days 1 and 2. For the 3 dpi time point, samples of only 1 infection experiment were available. Blue: Hoechst 33342 chromatin stain (cell nuclei). **(B)** Immunostaining overviews of NiV infection in non-differentiated PBEC (pig) and FBEC (ferret) for NiV N (magenta) at 3 dpi. Scale bars = 20 µm.

5.1.2. Characterization of differentiated primary BEC cultured at ALI

To study NiV infection in a more physiologically context compared to non-differentiated BEC, ALI-differentiated BECs were prepared from two distinct ferrets or pigs (see 4.1.3). After 4 weeks of cultivation, this resulted in a polarized, pseudostratified respiratory epithelium as confirmed by fluorescence microscopy analysis of cross sections (Figure 9). Indeed, epithelial cell markers for tight junctions and cilia (ZO-1 and ß-tubulin; Figure 9A), basal cells and mucus (cytokeratin 5 and Mucin-5AC; Figure 9B), and adherens junctions (β-catenin, Figure 9C) were successfully detected. These

confirmed differentiation of the PBEC and formation of a complex epithelium including physiologically relevant cellular subpopulations such as ciliated cells, secretory cells and basal cells.

At 2 dpi NiV nucleoprotein N was detected in apical cells following infection with 2 × 10^6 pfu/well (Figure 9D, arrowhead), indicating a general susceptibility of the PBEC-ALI cultures to NiV infection. However, considering the high inoculation dose, the frequency of NiV infected cells was low, suggesting a low specific infectivity of NiV on these PBEC-ALI cultures.

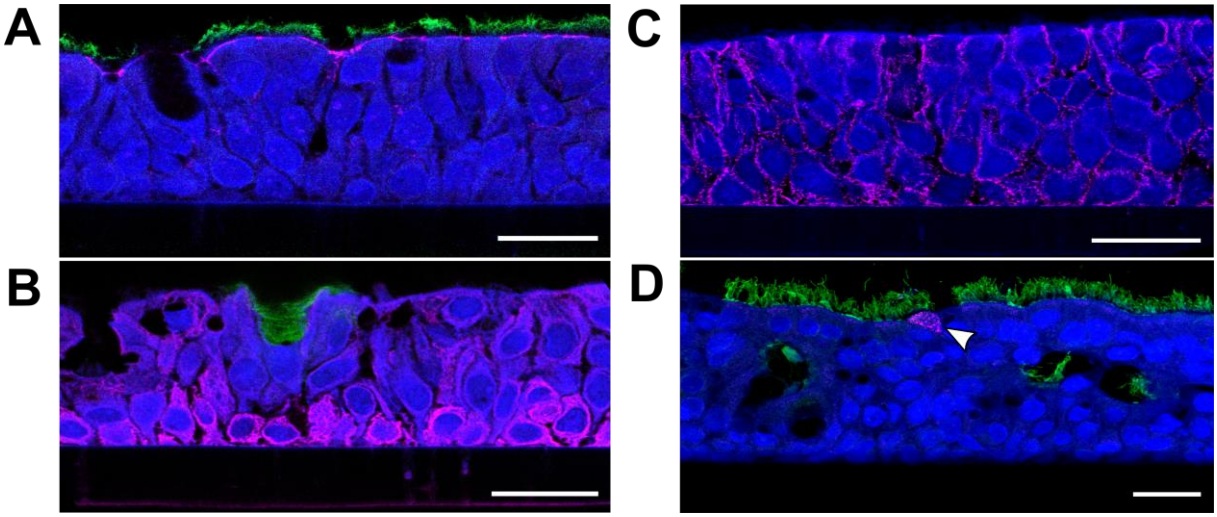

Figure 9: Characterization of PBEC-ALI cultures by detection of epithelial cell markers and NiV protein. (A) Immunostaining of cross sections for β-tubulin (ciliated cells; green) and ZO-1 (tight junctions; magenta), **(B)** Mucin-5AC (mucus secreting cells; green) and Cytokeratin 5 (basal cells; magenta), and **(C)** β-catenin (cell adherens junctions; magenta). **(D)** Immunostaining for β-tubulin (green) and NiV nucleoprotein N (magenta) at 2 dpi (see 4.3.6). Arrowhead: NiV infected cell. Scale bars: 20 µm.

5.1.3. Time course of NiV infection in pig and ferret BEC-ALI cultures

NiV infection dynamics were monitored in PBEC- and FBEC-ALI cultures, following infection of differentiated cultures with 2 × 10^6 pfu/well (see 4.3.6) and fixation at 0, 1, 2, 5, 7, 9, and 12 dpi. Immunofluorescence staining (see 4.5.2) for NiV N and chromatin staining were performed to assess virus spread and cell layer integrity (Figure 10). NiV N was not detectable at 0 and 1 dpi in both PBEC and FBEC cultures. However, after 2 days, N protein was detected in small spots. The NiV infection further spread until 12 dpi. Infections remained focal and complete infection of the cultures was not observed, even at 12 dpi. Whereas in the PBEC-ALI cultures a continues cell layer remained till 12 dpi the cell layer of FPEC was partially destructed at 5 to 12 dpi (Figure 10B arrowheads and Supplement 7).

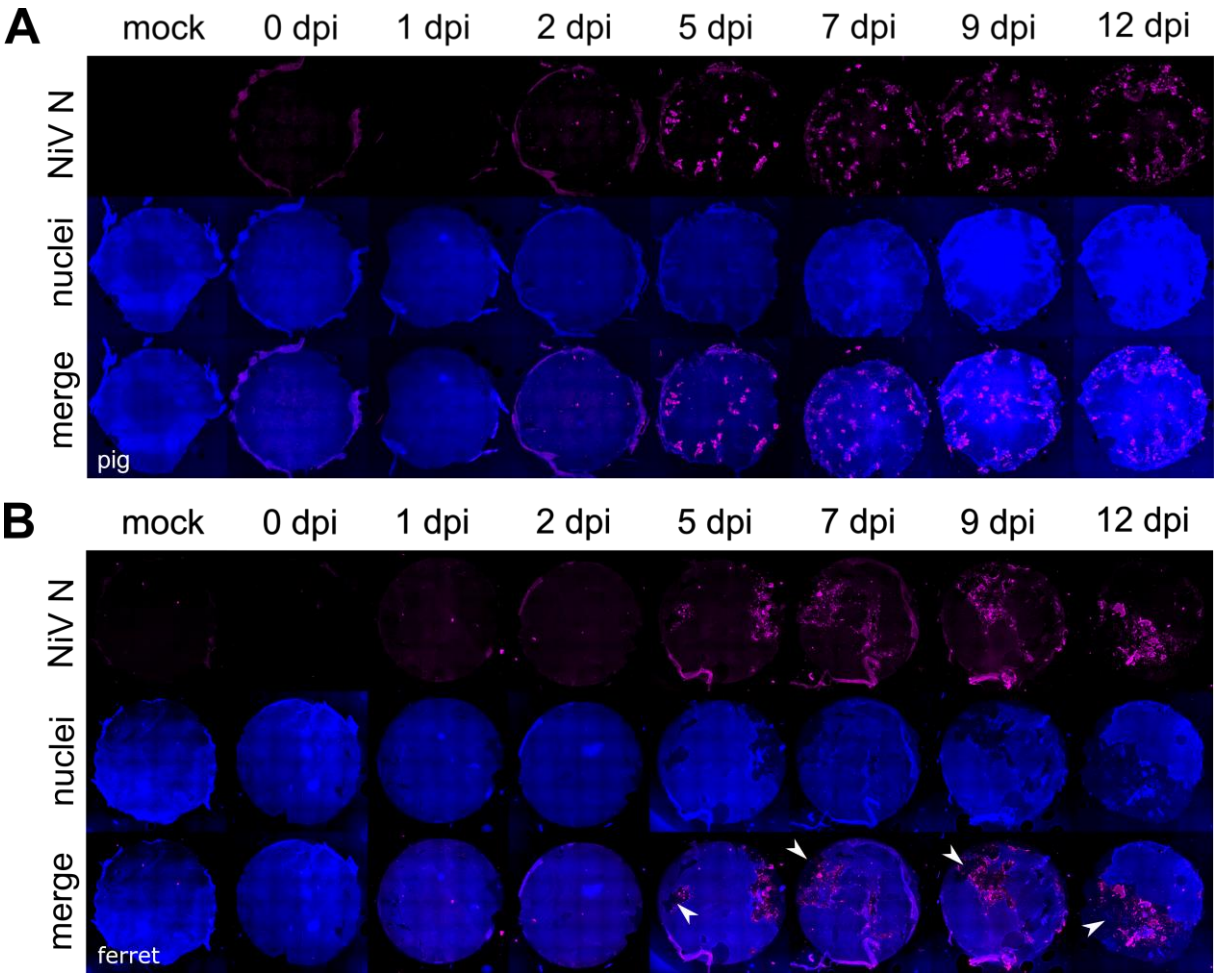

Figure 10: Time course of infected ferret and pig PBEC-ALI cells. Ferret and pig PBEC-ALI cultures were infected with the NiV (see 4.3.6) and fixed after 0, 1, 2, 5, 7, 9 and 12 dpi. Images were acquired by tile-scanning and subsequent stitching of complete membranes. **(A)** Immunostaining of NiV infected pig and **(B)** ferret PBEC-ALI membranes against NiV N (magenta). Arrowheads indicate destructed cell layers. Representative for two independent experiments with distinct donor animals. The diameter of the membranes was approximately 0.64 cm and nuclei were counterstained using Hoechst 33342.

Whether NiV infection correlated with virion release at the apical and basal side or if the virus remains cell associated was investigated by determining infectious titres in apical washes and in the basal medium by titration on Vero cells (see 4.3.4). Notably, in spite of progressing virus replication, in the PBEC ALI-cultures the apical infectious virus titers remained at input virus levels detected at 0 dpi (3×10^3 pfu/ml) (Figure 11A). In contrast, in FBEC ALI-cultures, a 4-log drop from 2.3×10^5 to 3.4×10^1 pfu/ml was observed at 1 dpi. With ongoing NiV infection, the apical titers increased to 4×10^4 and 2×10^5 pfu/ml at days 9 and 12 dpi, respectively (Figure 11B). However, a high variation between both ferret samples was observed and the apical titres did not reach the input level until 12 dpi. Even less virus was detected in the basal compartment, where virus titers up to 180 pfu/ml from PBEC-ALI and 263 pfu/ml from FEBEC-ALI cultures were determined from day 5 on (Figure 11).

These data revealed that infectious virions at the apical and basal side did not substantially increase even at days 5 to 12 (Figure 11), where substantial increase of NiV infected cells was observed (Figure 10). This indicated a limited virion release from the infected ALI-cultures.

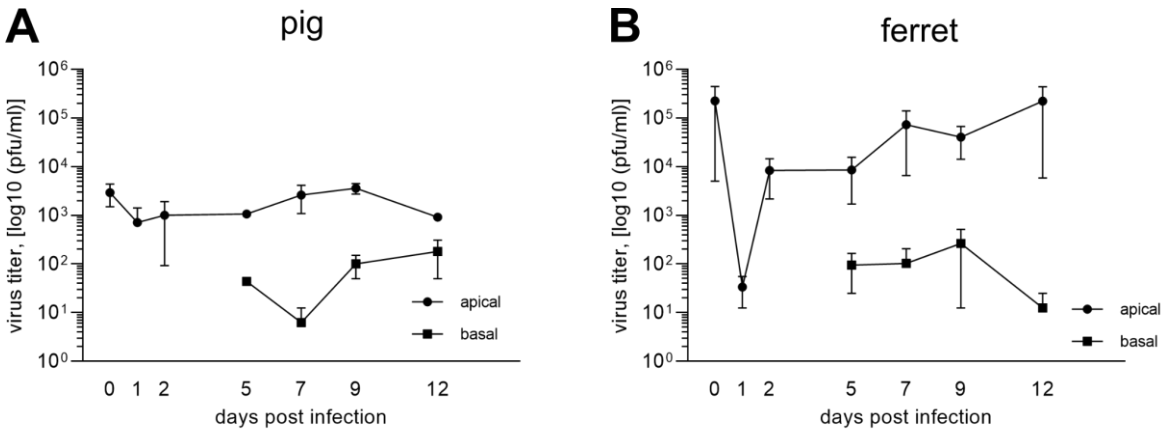

Figure 11: Time course of infectious NiV release at the apical and basal side of PBEC- and FBEC-ALI cultures. (A) NiV infectious titers (4.3.4) obtained from the apical and basal sides of pig and **(B)** ferret PBEC-ALI cultures. In the basal compartment no virus was determined until 5 dpi for both species. Results are depicted as the mean of two replicates with the minimum and maximum value indicated by error bars.

To assess whether virus RNA-levels as a measure of virus replication and gene expression correlated with low and steady state levels of infectious virus released at the basal and apical sides, relative virus mRNA levels in cell lysates of differentiated PBEC-ALI were determined by qPCR with NiV N specific primers (see 3.8) after RNA-extraction (see 4.4.10) and reverse transcription with Oligo (dt)18 primer (see 3.8). In contrast to the limited virus release (Figure 11), increasing virus mRNA levels in cell lysates indicated virus replication and spread in the PBEC-ALI cultures (Figure 12). These data indicated that most of the newly synthesized NiV-RNA remains cell associated.

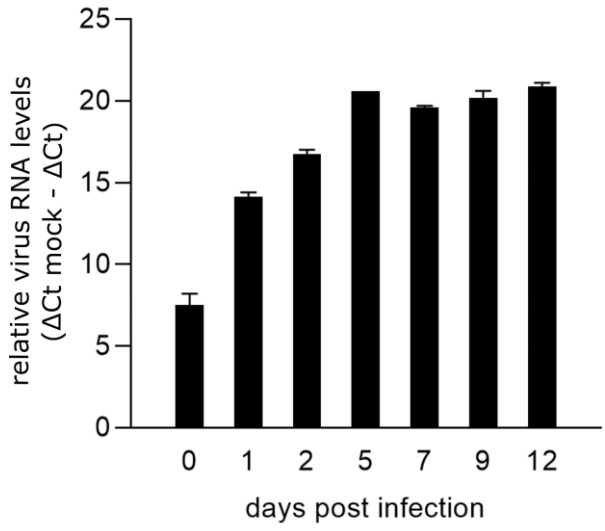

Figure 12: Quantification of viral mRNA in PBEC-ALI cultures. Quantification of viral mRNA (see 4.4.11) in PBEC-ALI cultures with NiV N gene primers (see 3.8). Depicted are the relative virus RNA levels after subtracting ΔCt values from the ΔCt mock value with a sample range of n=2. Error bars indicate minimum and maximum value.

5.1.4. Lateral NiV spread and cell death

Further characterization of NiV infection in BEC-ALI cultures was carried out by analyzing immunofluorescence stained cross sections (see 4.5.2) to monitor the infection process in the different cell types and areas. However, due to technical restrictions to generate cross sections for FBEC-ALI cultures, following analysis was performed with PBEC-ALI cultures. Cross sections at 12 dpi revealed large infected areas with a strong CPE and disruption of the epithelium (Figure 13A). Furthermore, the infection resulted in apical release of virus antigen-positive cell detritus (Figure 13A, top left). In spite of the abundance of NiV N in infected areas and virus positive cell detritus, the infected areas were surrounded by non-infected regions (Figure 13A, top right) resembling the uninfected mock control (Figure 13A, bottom). Additionally, even in highly infected and disrupted areas, clusters of ciliated apical cell and basal cell layers (Figure 13A, arrow and arrowhead, respectively) indicated that the apical and basal cell layers were less infected and exhibited less cytopathic effects than cells located in-between. Infection of ciliated and non-ciliated apical cells (Figure 13B, arrows), as well as basal cells at 2 dpi confirmed general susceptibility of these cell types for NiV infection. Virus infection spread to the basal side and subsequently laterally from 5 to 12 dpi in-between the apical and basal cell layer. Increasing cell destruction and cell debris accumulation were observed for the intermediate cell layer. However, apical and basal cells in these infection foci were either not infected (Figure 13, asterisks) or not destroyed by infection (Figure 13B, diamonds). Even at 9 and 12 dpi, areas with fragmented cell nuclei were framed by infected or non-infected ciliated and basal cells. These data indicate that cell-to-cell spread of the virus in the PBEC-ALI mainly occurs laterally in the middle cell layers and that apical and basal cell layers exhibit less CPE.

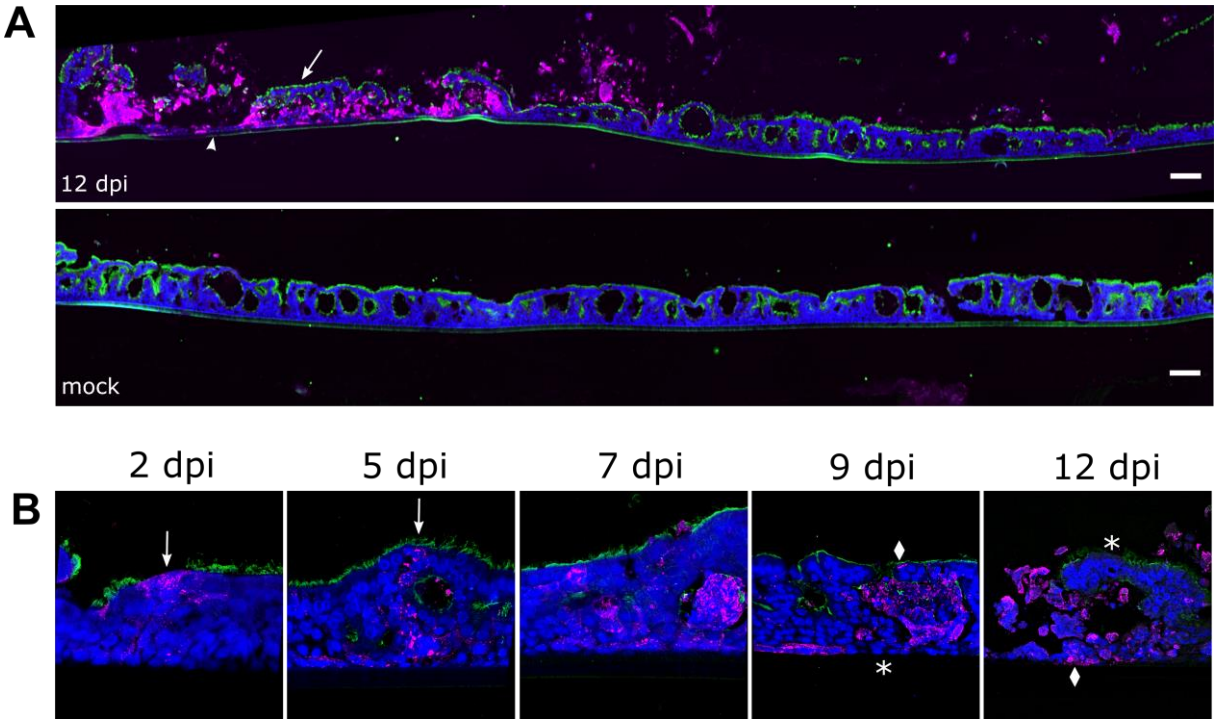

Figure 13: Time course of NiV infection in pig PBEC-ALI cultures and CPE. Immunostaining of NiV-infected PBEC-ALI culture cross sections against NiV N (magenta) and β-tubulin (green). Representative for two independent experiments with distinct donor animals. **(A)** Large cross section of a 12 dpi membrane at the top and the mock control at the bottom. Arrow and arrowhead indicate less infected and destructed areas of ciliated and basal cells, respectively. Scale bars: 100 µm. **(B)** Time course of NiV infection until 12 dpi with representative sections. No NiV positive cells were observed 1 dpi. Arrows indicate infection in ciliated and non-ciliated cells of the apical cell layer. Stars represent non-infected cells and diamonds infected. Nuclei were stained with Hoechst 33342.

The structural integrity of the apical and basal cells was further demonstrated by immunostaining (see 4.5.2) for cytokeratin 5, zonula occludens 1 (ZO-1), β-catenin, and Mucin-5AC at 12 dpi. The disrupted middle cell layer with condensed chromatin was framed by an intact continuous cytokeratin 5 positive layer with infected and non-infected basal cells (Figure 14A) and an intact apical cell layer with apical tight junctions, demonstrated by ZO-1 stain (Figure 14B). Furthermore, and in contrast to non-infected PBEC-ALI cultures or uninfected areas (Figure 9A, Figure 14F), ZO-1 appeared as double cell layered packages with tight junctions at both sides (Figure 14B). In addition, β-catenin revealed the same intact double-cell layer on top of the cell detritus (Figure 14C). The intact adherens junctions were observed in both apical and basal cell layers (Figure 14C). Mucus in apical parts and in close contact to infected cell detritus were indicated by Mucin-5AC stain (Figure 14D). Uninfected areas 12 dpi stained for cytokeratin 5 (Figure 14E) and ZO-1 (Figure 14F) further indicated the integrity of basal cells and the integrity of the tight junctions in infected regions shown in Figure 14A and B. These data confirmed the integrity of the basal and apical cell layers even at sites of strong NiV infections.

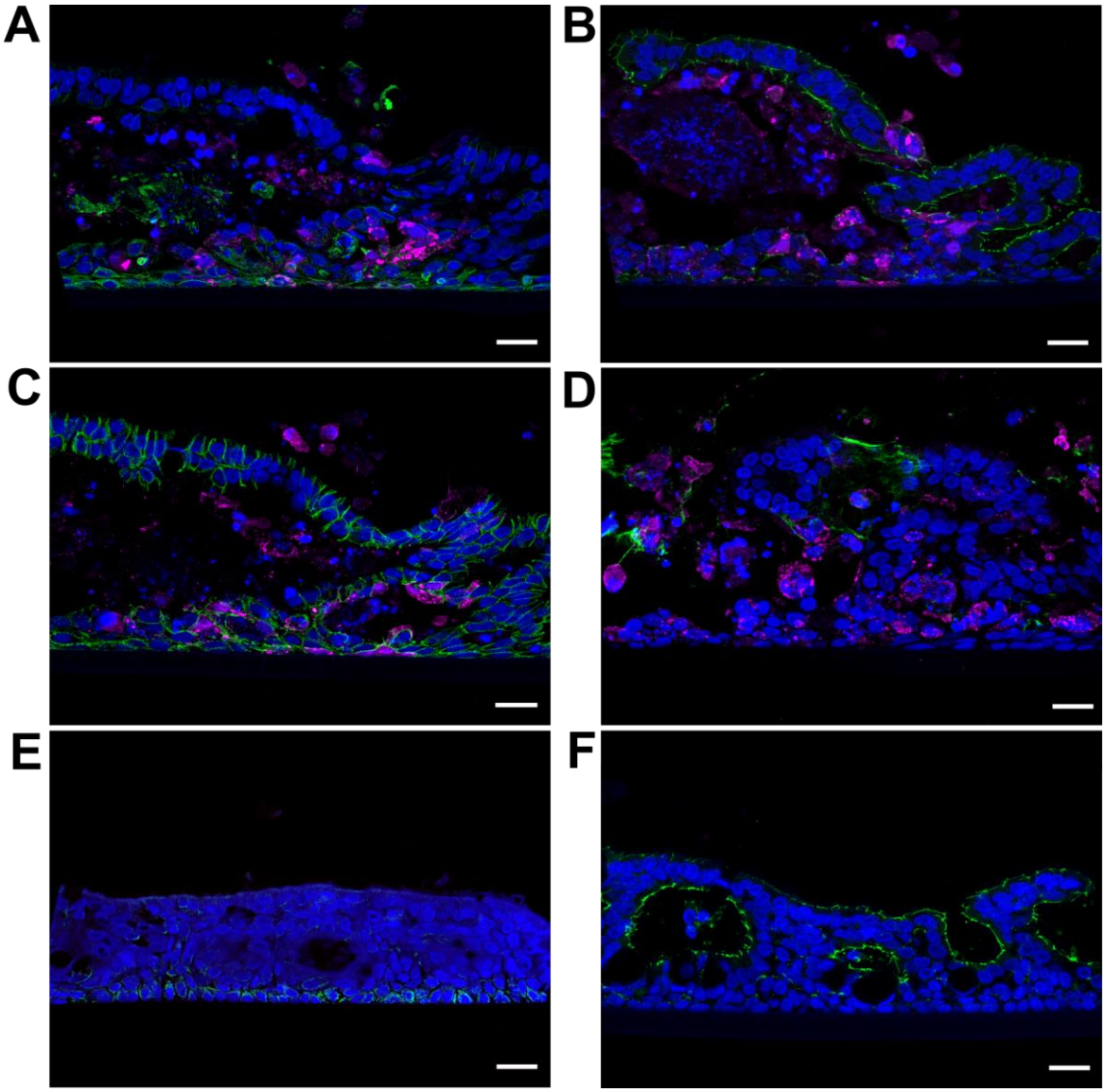

Figure 14: Visualization of NiV infection in cross section of infected PBEC-ALI cultures 12 dpi with various epithelial cell markers. Immunostaining of NiV-infected PBEC-ALI culture cross sections against NiV N (magenta) and **(A)** cytokeratin 5 as a basal cell marker (green), **(B)** ZO-1 for tight-junctions (green), **(C)** β-catenin for adherens junctions (green), and **(D)** Mucin-5AC for mucus-secreting cells (green). **(E)** Visualization of uninfected areas 12 dpi by immunostaining against NiV N (magenta) and cytokeratin 5 (green) **(F)** and ZO-1 for tight junctions (green). Representative sections of two independent experiments with distinct donor animals. Scale bars: 20 µm.

5.1.5. Upregulation of type I interferons and inflammatory cytokines

To analyze the induced host responses and the destruction of the epithelium by NiV infection, cytokine and interferon-stimulated-gene (ISG) upregulation was monitored. To assess NiV induced cytokine expression at 0, 1, 2, 5, 7, 9, 12 dpi, RNA samples were transcribed to cDNA and analyzed by qPCR (see 4.4.11) for interferon beta (IFN-β), interferon lambda (IFN-λ), interleukin 6 (IL-6), interleukin 8 (IL-8), oligoadenylatsynthetase 1 (OAS-1), and IFN-stimulated gene 56 (ISG-56). Cytokine expression was low at early time points of infection (day 1 and 2; Figure 15) and increased IFN-β, IFN-λ, IL-6 and IL-8 induction was observed at 5 dpi. In contrast, the ISGs OAS-1 and ISG-56 remained low.

Early increase of IL-6 and IL-8 after adding the virus to the cells suggest a quick host response after infection. However, since IL-6 and IL-8 levels decreased at 1 dpi, they either represented a direct response to NiV infection or the initial rise is based on a short-term effect induced by the transport of the PBEC-ALI cultures from the BSL-2 to the BSL-4 facility.

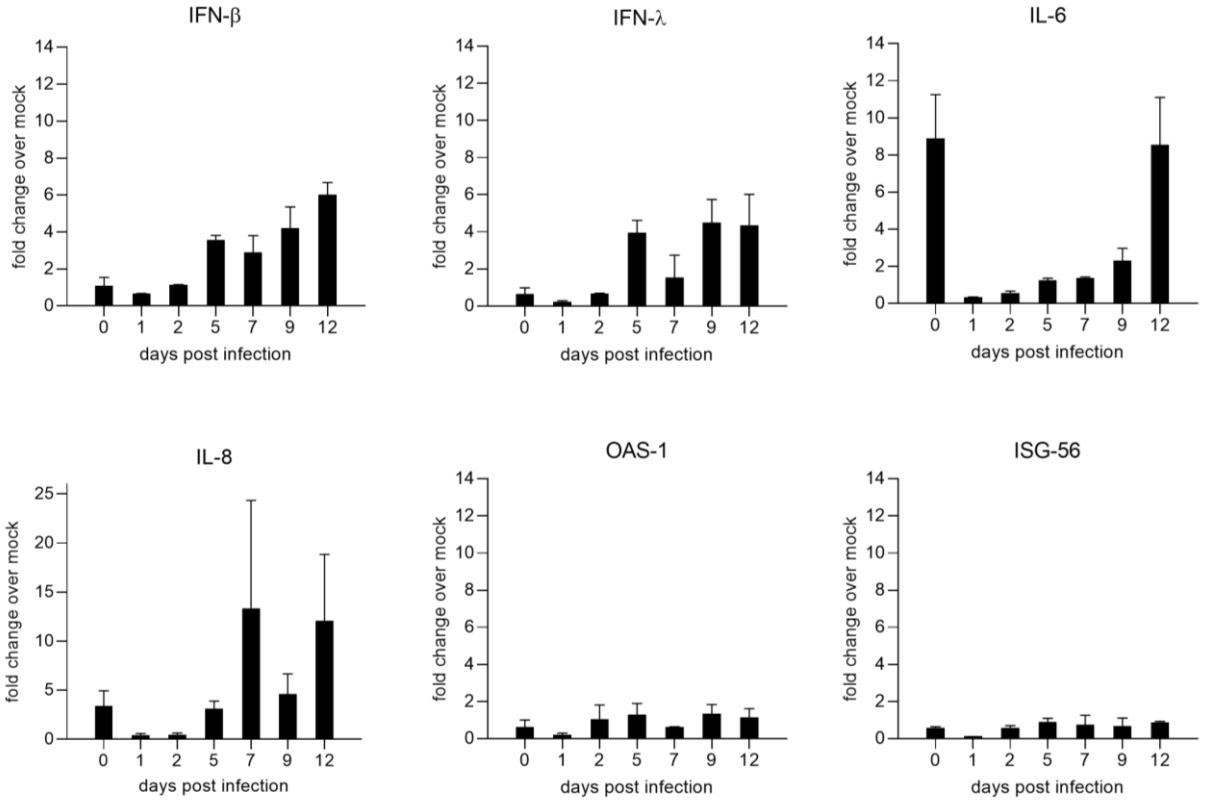

Figure 15: Time course of NiV induced cytokine and interferon-stimulated-gene (ISG) upregulation. Quantification of cytokine and ISG mRNA after RNA extraction (see 4.4.10) by qPCR (see 4.4.11) for IFN-β, IFN-λ, IL-6, IL-8, OAS-1, and ISG-56. Results are depicted as fold change over mock from two replicates with the minimum and maximum value indicated by error bars. Fold change over mock was calculated with the 2-ΔΔCT method (see 4.4.11).

5.1.6. NiV protein dynamics

To confirm whether the increase of ISGs measured on mRNA level also resulted in changed protein expression, the host response to NiV infection on a protein level was assessed by mass spectrometry. Protein samples from the different time courses were subjected to quantitative high-resolution mass spectrometry based on LFQ (see 4.6.1 and 4.6.2) to analyze the dynamic and complex molecular virus-host interplay in an *in vitro* infection model. Considering the limited number of infected cells observed in the early stage of infection (Figure 10), only low virus protein levels were detected 1 dpi (Figure 16) which remained on input levels detected 0 dpi. In accordance with the immunofluorescence data (Figure 10), an onset of NiV gene expression was indicated by increased NiV N and P levels at 2 dpi. Further increase of RNP-associated proteins and the envelope proteins M, F and G correlate with the replication and spread of the virus observed by immunofluorescent and qPCR detection (Figure 12).

From day 5 on, accessory V, W and C proteins were detected as well. Both infection kinetics performed revealed a robust increase of structural virus protein levels from early to late time points in infection. Unique peptides for all NiV proteins, including all accessory proteins were detected during the course of in infection in fully-differentiated PBEC-ALI cultures. The increasing protein levels confirmed the immunofluorescence data in a quantitative and reproducible manner.

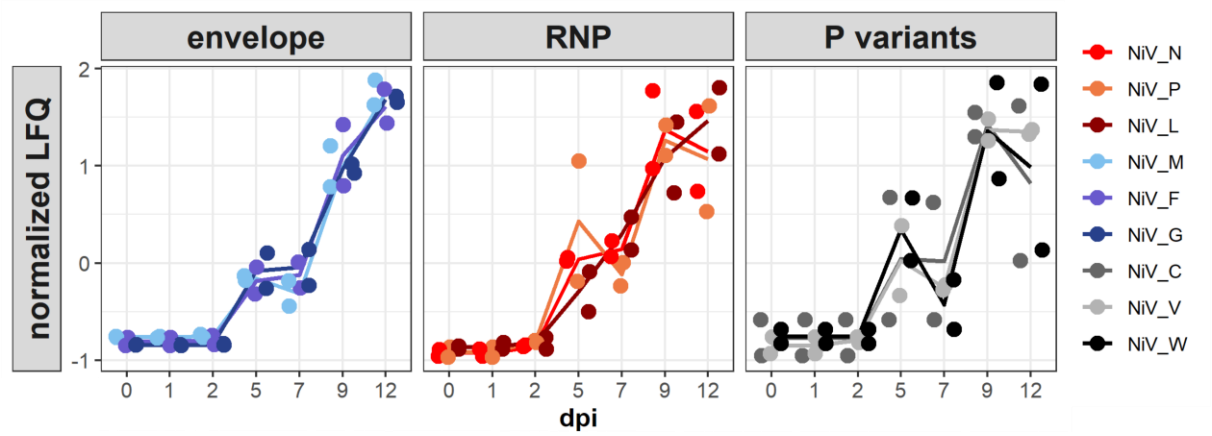

Figure 16: Time course of NiV protein expression in pig PBEC-ALI cultures. Protein samples were extracted from NiV-infected pig PBEC-ALI cultures and analyzed by MS (4.6.1). NiV proteins are grouped as envelope proteins (M, F and G), RNP-associated proteins (N, P and L) and P-associated accessory proteins (C, V and W). NiV protein levels are depicted as normalized values based on label-free quantification (4.6.2). Curves represent the mean of two independent time course experiments (n=2) with the respective values indicated by colored bullets.

5.1.7. Variation of the host cell proteome during infection

A total of 6345 host proteins were identified by MS and considered for further statistical analysis (4.6.2). The principal component analysis (PCA) of the unprocessed quantitative data (Figure 17, left panel) indicated time-dependent clustering of samples, which was, superimposed by a dominant influence of the respective donor animals on the composition of the proteomes. This influence could be partially compensated by normalization of the quantitative data (Figure 17, right panel), which resulted in a more time-dependent clustering of all samples. In a first statistical evaluation, which included all time points, the expression kinetics of all identified proteins (virus and host) were subjected to a von Neumann test (von Neumann, 1941) to detect those proteins with expression levels that do not vary randomly over time but rather show a time-dependent trend. To this end, von Neumann statistics were performed for every identified protein and both experiments separately to detect those with an up- or downward expression trend. Proteins that showed p-values < 0.05 in both replicates of the kinetic experiment were subjected to GO analysis with the gProfiler R-package. The resulting enriched GO terms (Supplement 8) strongly suggested activation of the innate immune response (GO:0045087) and other pathways detailed below.

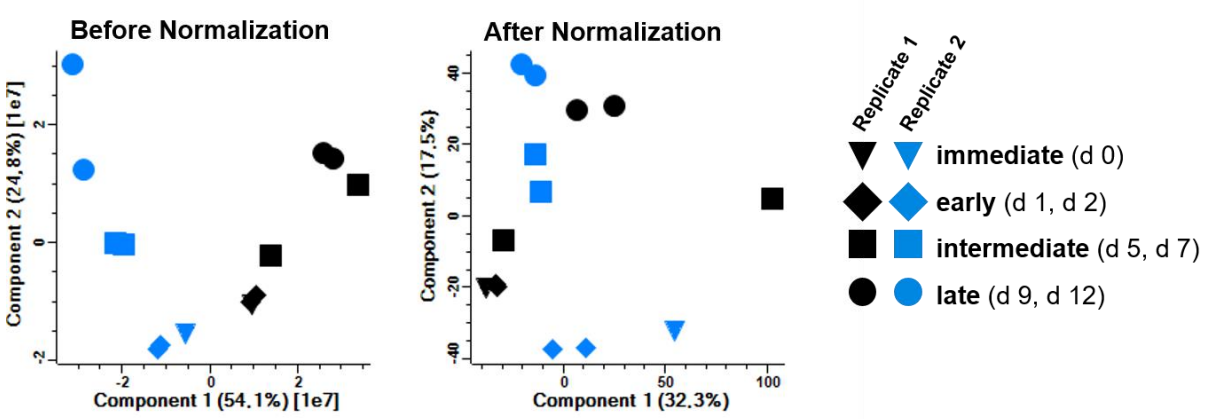

Figure 17: PCA of NiV-infected PBEC-ALI cultures. Quantitative MS data of both independent replicates were subjected to PCA analysis before (left panel) and after (right panel) normalization. Prior to normalization, animal-to-animal variability dominated the sample clustering. This influence was partially compensated by normalization, resulting in a more time-dependent clustering of all samples.

5.1.8. DEG and GO term enrichment analysis

For further statistical evaluation of the impact of NiV infection on the host proteasome and the identification of DEG, the early (1 dpi, 2 dpi) and late (9 dpi, 12 dpi) stages were compared. The selection was based on the clustering of the samples in the PCA analysis (Figure 17) and that 5 and 7 dpi represent a transition phase in the expression of viral proteins (Figure 16). Furthermore, qPCR analysis at 0 dpi (Figure 15) suggested handling effects on the PBEC-ALI and this time point was excluded from evaluation. Comparing DEG of the early and late stage of the infection and statistical testing (left or right-sided t-test, p-value < 0.05) of normalized data revealed 730 upregulated and 123 downregulated genes (Supplement 5). To achieve an overview of GO and KEGG terms and their relation to each other, enrichment analysis of DEG followed by network analysis in Cytoscape was performed (Figure 18, Supplement 6). Multiple innate-immunity related pathways were upregulated, including type I and gamma interferon signaling and responses, antigen processing, MHC I protein complexes and protein processing (Figure 18A), indicating a broad upregulation of anti-viral and immune system activating factors. On the other hand, pathways downregulated at a later time point of infection included metabolic processes and processes involved in mRNA splicing (Figure 18B). Overexpressed genes were mainly annotated with innate immune response processes (GO:0006955, GO:0002218, GO:0002252, GO:0002253) and downregulated genes were primary involved in RNA splicing and mRNA processing (KEGG:03040, GO:0006397, GO:0008380, GO:0000398) (Supplement 9). Cellular components (annotated in the GO:CC branch of the Gene Ontology) with increased expression included the proteasome complex (GO:0000502), ER (GO:0005783), MHC I peptide loading complex (GO:0042824), and mitochondria (GO:0005739).

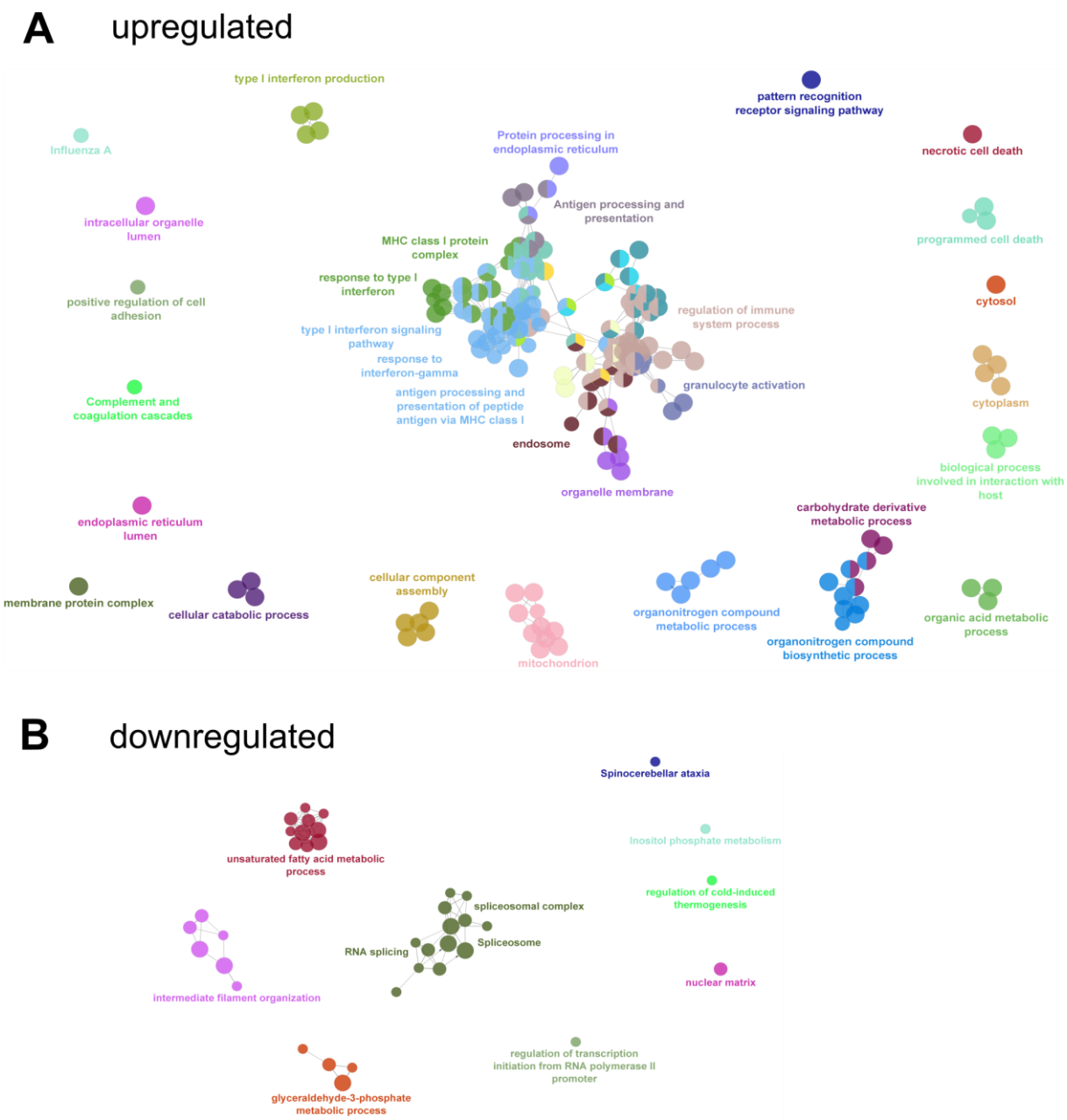

Figure 18: Overview of enriched GO and KEGG terms and their relation by GO network analysis. Early (1 dpi, 2 dpi) and late (9 dpi, 12 dpi) stages were compared. Up- **(A)** or downregulated **(B)** genes were subjected to GO-term enrichment analysis followed by network analysis with the ClueGO package (Bindea et al., 2009) of Cytoscape (4.6.2). Clusters are labeled with one representative GO-term name from the cluster. Parameters and detailed results are listed in Supplement 6.

Six GO/KEGG terms listed in Table 7 were selected for a more detailed analysis of the expression kinetics of the associated gene products. The relative expression levels of the identified proteins representing the respective enriched GO terms were visualized in volcano plots in Figure 19 to Figure 21 together with NiV protein levels as a reference for upregulated genes. For DEG highlighted in the following volcano plots, the individual values for expression fold-changes and p-values are listed in Supplement 10.

Table 7: Overview of selected GO/KEGG terms for a more detailed analysis. Based on GO-term enrichment analysis of differentially regulated genes with the gProfiler software (Supplement 9).

regulation	term name	GO ID
up	antigen processing and presentation of peptide antigen	GO:0048002
	proteasome	KEGG: 03050
	response to type I IFN	GO:0071357
	response to IFN gamma	GO:0034341
	pattern recognition signaling pathway	GO:0002221
down	spliceosome	KEGG:03040

Ribosomal proteins were chosen as a presumably unaffected control (Figure 19A) and showed no significant changes in the expression level as expected. Abundance of most identified proteins remained unchanged. On the other hand, significant regulations were observed for proteins related to genes annotated with other terms, including the spliceosome complex (Figure 19B). For instance, 23 proteins were downregulated, while only 2 were upregulated (Figure 19C) within the spliceosome complex term. For further analysis of typical virus host response pathways, terms for pattern recognition and interferon response were evaluated.

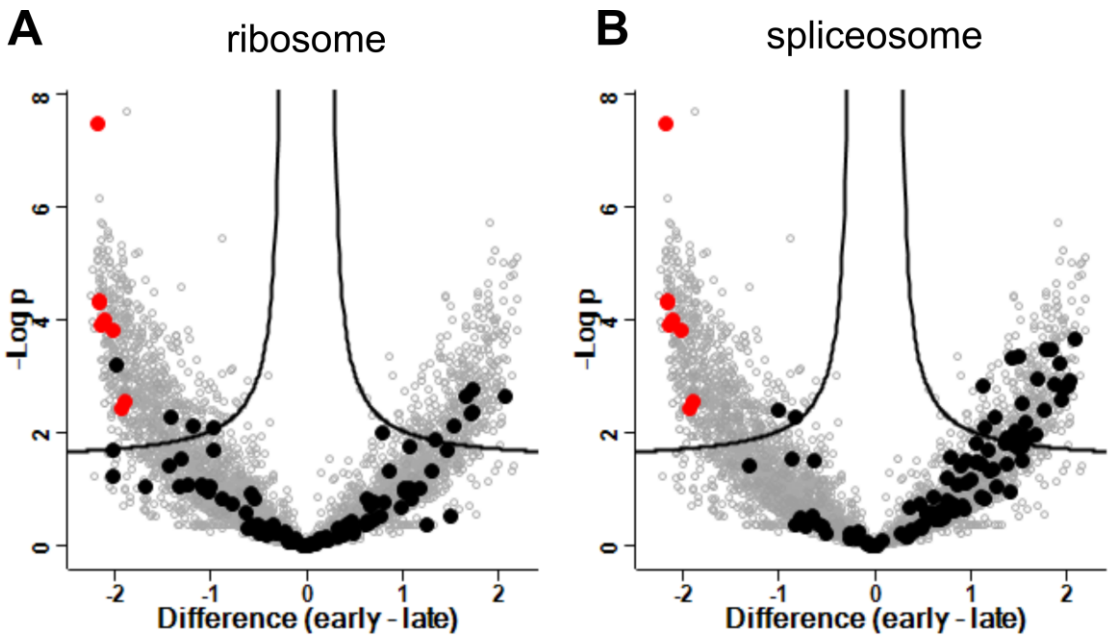

C

ribosome	
up	CANX, RPL32, RPS11, RRBP1
down	APEX1, MRPL11, MTG1, RPL13, RPL34, RPS25, RPS3
spliceosome	
up	PRPF8, XAB2
down	DDX23, DHX15, HNRNPA3, *HNRNPC, HNRNPK, HNRNPM, **HSPA1, HSPA8, LSM4, LSM6, PPIH, PPIL1, PRPF3, PRPF40A, PUF60, RBM8A, SLU7, SNRPA1, SRSF1, SRSF3, SRSF9, TCERG1, U2AF2, USP39

**HNRNPC: HNRNPCL1; HNRNPCL2; HNRNPCL3; HNRNPCL4; **HSPA1: HSPA1A; HSPA1B*

Figure 19: Differentially expressed genes in late and early phases of infection: NiV proteins (red), ribosomal (KEGG:03010), and spliceosomal (KEGG:03040) proteins. Volcano plots highlight genes annotated within GO-Terms **(A)** ribosome (KEGG:03010) and **(B)** spliceosome (KEGG:03040). **(C)** DEG corresponding to GO terms.

5.1.9. Interferons and antigen pattern recognition

The impact of NiV infection on the interferon induction, the pattern recognition factors, and the host proteasome response was evaluated by visualization of gene expression relating to specific GO terms in volcano plots (Figure 20). Upregulation of 24 proteins revealed strong type I IFN signaling and response (Figure 20). The affected proteins include 2'-5'-oligoadenylatesynthetases (OAS2, OASL), interferon-induced GTP-binding protein Mx proteins (MX1, MX2), interferon-induced protein with tetratricopeptide repeats 2 (IFIT2) and signal transducers and activators of transcription (STAT1, STAT2). Furthermore, increased expression levels of proteins involved in type II IFN-gamma signaling were observed (Figure 20). This involved 16 proteins like protein tyrosine phosphatase non-receptor type 1 (PTPN1), beta-2-microglobulin (B2M), and E3 ubiquitin-protein ligases (TRIM22, TRIM22). Moreover, 12 proteins associated with the pattern recognition pathway (GO:0002221) were upregulated (Figure 20), including the monocyte differentiation antigen CD14 (CD14), cathepsin S

(CTSS), endoplasmin (HSP90BS) operating as a molecular chaperon in the processing and transport of secreted proteins, dual specificity mitogen-activated protein kinase kinases (MAP2K1, MAP2K3), nuclear factor NF-kappa-B p100 subunit (NFKB2) and the toll-like receptor 3 (TLR3). On the contrary, ubiquitin-conjugating factors UBE2D2 and UBE2V1 were decreased when early and late stage of infection were compared (Figure20). Overall, these data indicate a broad NiV induced upregulation of interferon-related signaling pathways and the pattern recognition pathway.

A

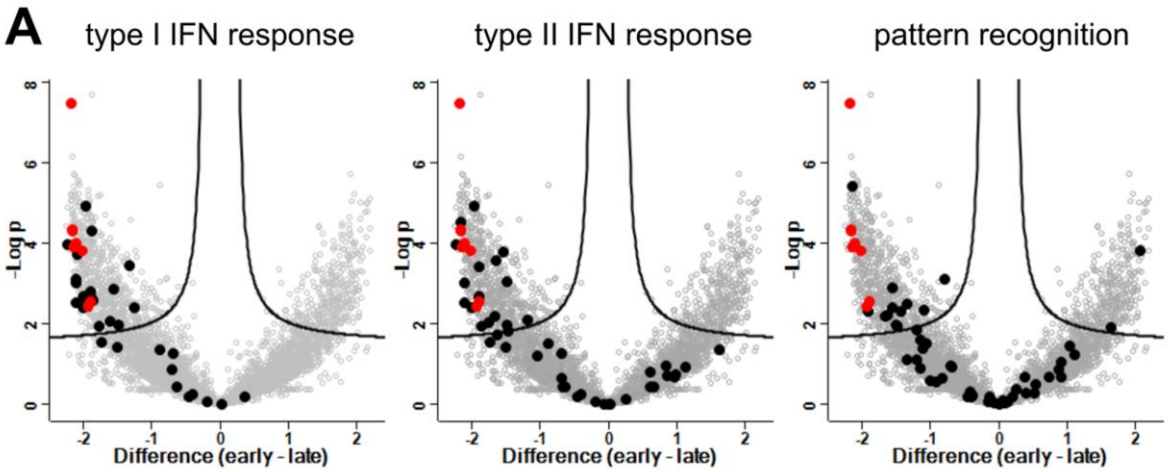

B

	type I IFN response
up	ADAR, BST2, GBP2, *HLA, IFIT2, IFIT3, ISG15, ISG20, MX1, MX2, OAS2, OASL, PSMB8, PTPN1, RSAD2, STAT1, STAT2, **USP
down	-
	type II IFN response
up	B2M, BST2, CAMK2D, GBP2, GBP6, *HLA, ICAM1, NUB1, OAS2, OASL, PML, PTPN1, STAT1, TLR3, TRIM21, TRIM22
down	-
	pattern recognition receptor signaling pathway
up	CD14, CTSSm, HSP90B1, LBP, MAP2K1, MAP2K3, NFKB2, PGLYRP1, PIK3AP1, RIPK1, TLR3, UNC93B1
down	UBE2D2, UBE2V1

**HLA: HLA-A;HLA-B;HLA-C;HLA-E;HLA-F;HLA-G; **USP: USP18;USP41*

Figure 20: DEG in late and early phases of infection: virus proteins, type I IFN response (GO: 0071357), and response to IFN gamma (GO:0034341). Volcano plots highlight genes annotated with GO-terms **(A)** response to Type I IFN (GO: 0071357), response to IFN gamma (GO:0034341), and pattern recognition (GO:0002221). NiV proteins are highlighted in red as reference for upregulated genes. **(B)** Regulated DEG corresponding to GO-Terms.

5.1.10. Antigen processing and presentation

Pathways activated by the interferon response were analyzed including the antigen processing and presentation of peptide antigen (GO:0048002), as well as the proteasome complex (GO:0000502). This indicated a potent upregulation of antigen processing and presentation upon virus infection and interferon induction (Figure 21). Increased expression of 16 proteins like the TAP-transporters (TAP1, TAP2), ER chaperon Calreticulin (CALR) and Calnexin (CALN), MHC I components B2M and HLAs and aminopeptidases ERAP1 and ERAP2, indicated upregulation of MHC I dependent antigen presentation with progressing infection (Figure 21A). Furthermore, cathepsin CTSS and CTSV levels are upregulated, suggesting activation endosomal antigen processing and MHC I cross-presentation by the vacuolar pathway. In contrast, downregulation was observed for the dynactin subunit 2 (DCTN2), protein transport protein Sec61 subunit beta (SEC61B) and several proteasome subunits.

Regarding the proteasome complex (Figure 21B), a total of 9 upregulated proteins were identified including immunoproteasome subunit beta types PSMB8, PSMB9, and PSMB10. Together with the proteasome activator complex subunit 2 (PSME2) of the immunoproteasome specific regulatory 11S cap structure, indicated increased levels of immunoproteasomes during the NiV infection. In contrast, decreased levels of PSMC1 (26S protease regulatory subunit 4; Rpt2), PSMC3 (26S protease regulatory subunit 6A; Rpt5), PSMD4 (6S proteasome non-ATPase regulatory subunit 4; Rpn10), and PSMD11 (26S proteasome non-ATPase regulatory subunit 11; Rpn6) further indicated conversion from the conventional 26S proteasomes to immunoproteasomes since they are part of the 19S regulatory subunit of the constitutive proteasome.

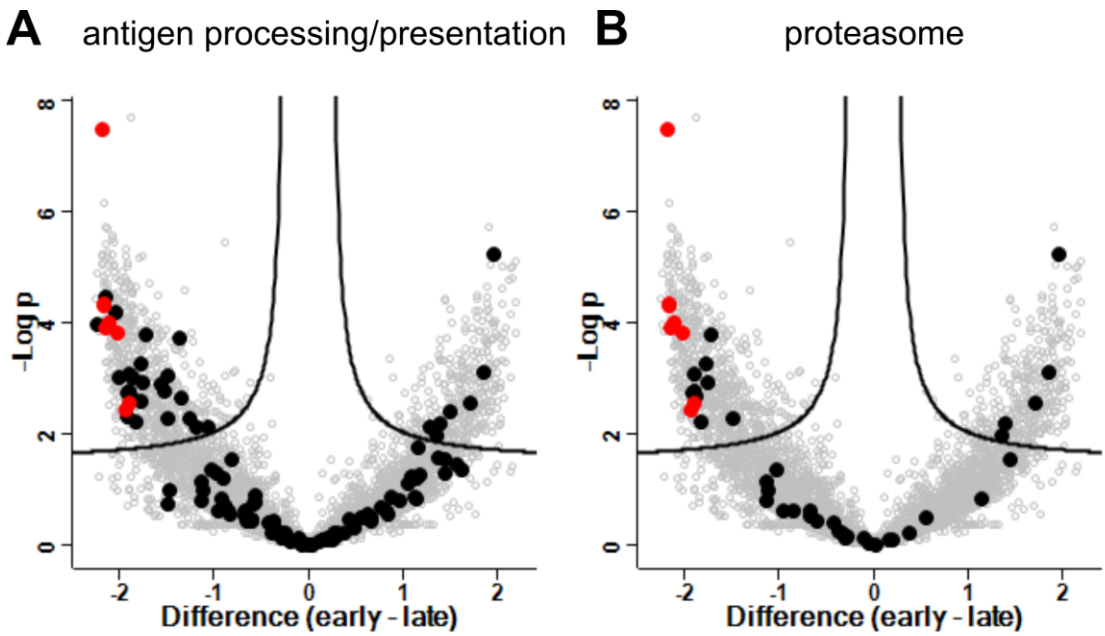

C

antigen processing and presentation	
up	B2M, CALR, CANX, CTSS, CTSV, ERAP1, ERAP2, *HLA, ITGAV, KIFAP3, KLC1, **PSMxx, TAP1, TAP2, TPP2, UNC93B1
down	DCTN2, **PSMxx, SEC61B
proteasome	
up	PSMA3, PSMB1, PSMB10, PSMB3, PSMB8, PSMB9, PSMD6, PSMD7, PSME2
down	PSMC1, PSMC2, PSMC3, PSMD11, PSMD4
**HLA: HLA-A, HLA-B, HLA-C, HLA-E, HLA-F, HLA-G; **PSMxx: proteasome subunits*	

Figure 21: Differentially expressed genes in late and early phases of infection: virus proteins, antigen processing and presentation (GO: 0048002), and proteasome (KEGG: 03050). Volcano plot highlight genes in black related to **(A)** antigen processing and presentation (GO:0048002) and **(B)** the proteasome term (KEGG:03050). NiV proteins are highlighted in red as reference for upregulated genes. **(C)** Regulated DEG corresponding to GO-Terms.

In summary, infection of fully-differentiated bronchial ferret and porcine ALI culture was characterized in this thesis. Thereby it was demonstrated that NiV induce a robust immune response upon infection. Strong interferon type I and type II response was observed resulting in a regulated antigen processing and presentation and the conversion from the constitutive proteasome to the immunoproteasome.

5.2. Establishment of a reverse genetic system for the Cedar virus

5.2.1. Construction of a full length cDNA CedPV plasmid

In order to generate a rCedPV that allows functional studies of *Henipaviruses* at BSL-2 facilities, a CedPV cDNA full length plasmid was constructed from synthetic DNAs and rCedPV was successfully rescued. Moreover, an imaging based quantitative pipeline was established for the testing of potential inhibitors of virus replication.

The CedPV cDNA clone was generated from synthetic DNA-fragments (see 4.7) on the basis of the CedPV isolate CG1a isolate sequence (gene bank accession no. NC_025351.1). The cloning procedure is depicted in Figure 22. Fragments 1 to 5 were obtained as linear dsDNAs, the 7506 bp L CDS was amplified from an L gene encoding plasmid (see 3.10). The length of each fragment, including the L CDS fragment amplified from an expression vector, indicated by the respective numbers. Each fragment contained overlapping terminal sequences of 30 bp (indicated by dashed lines) with the respective up- and down-stream fragments. The cDNA-fragments were sequentially inserted in the plasmid vector by Hot Fusion (see 4.4.8). The pt7 plasmid vector comprised a T7 promoter (T7P), an HDV-SC, a T7 terminator sequence (T7T) and an ampicillin resistance gene. Briefly, in a first reaction fragment 1 and fragment 2 were inserted, followed by fragment 3, fragment 4, fragment 5 and the L CDS. Full length cDNA sequencing revealed one mutation at genomic nucleotide position 2312 (G2312A), which was silent in the P ORF, but non-silent in the alternative C ORF (C protein amino acid position 68; R68K). The full length cDNA plasmid comprising the authentic CedPV sequence was generated by PCR-based mutagenesis of the pt7 CedPV C-R68K plasmid (see 4.4.9).

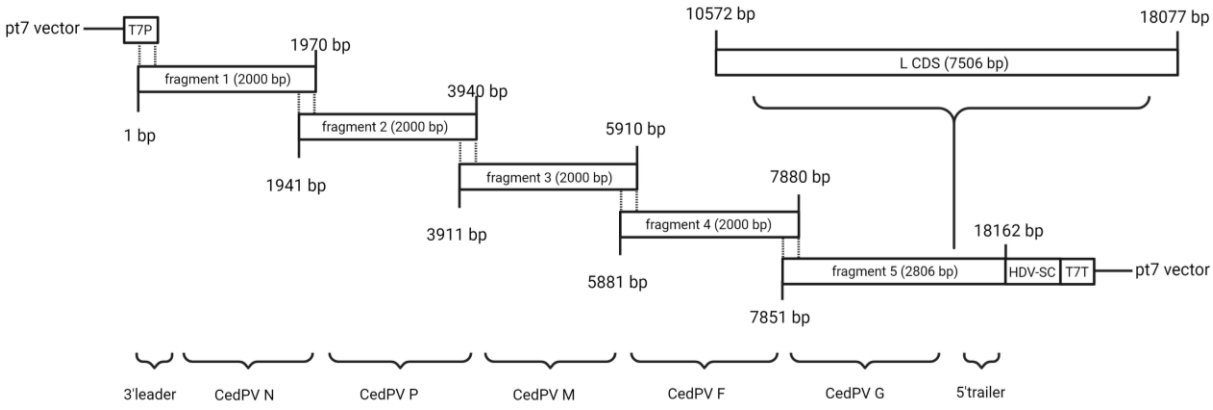

Figure 22: Schematic representation of the cloning strategy for the CedPV full-length cDNA clone. All fragments were ordered at Eurofins Genomics, based on the sequence of the CedPV full-length (cedar virus isolate CG1a, complete genome NC_025351.1). The length of each fragment, including the L CDS fragment amplified from an expression vector, are indicated by the respective numbers. Each fragment was synthesized with a 30 bp overhang (indicated by dashed lines) complementary to previous/subsequent fragment to simplify the assembly process via Hot Fusion (see 4.4.8). Briefly, fragment 1 and fragment 2 were cloned simultaneously into a pt7 vector, followed by fragment 3, fragment 4 and fragment 5. Due to the complexity of the L CDS region it had to be added at the end of the cloning procedure. For a detailed description of the molecular cloning see 4.7.

5.2.2. Rescue of rCedPV

Similar to previously described protocols (Laing et al., 2018), the cDNA full length plasmids for rCedPV C-R68K and rCedPV were transfected in BSR-T7/5 cells together with expression plasmids pCAGGS CedPV-N, -P and -L (see 4.3.1). In contrast to previous CedPV rescue protocols, where supernatant passaged to Vero cells was performed for virus detection and amplification, successful rescue of recombinant rCedPV was directly monitored in the transfected BSR-T7/5 cells. Formation of cell syncytia and immunofluorescence staining two days after supernatant transfer to fresh BSR-T7/5 cell cultures indicated a successful rescue, exemplary shown for rCedPV in Figure 23. Whereas the N protein was detected in typical cytoplasmic inclusion body structures, G protein exhibited a typical distribution in vesicle like structures.

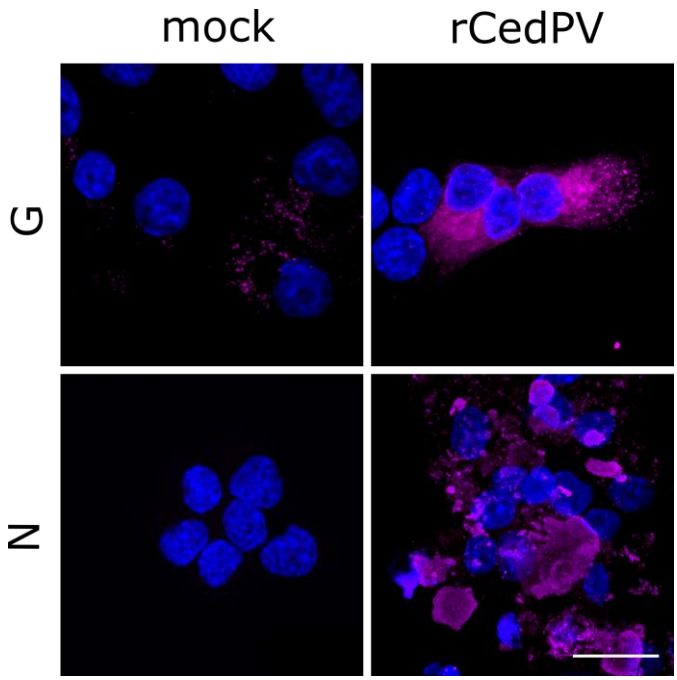

Figure 23: Immunofluorescence detection of CedPV N and G proteins in rCedPV infected BSR-T7/5. Successful rescue of recombinant CedPV was confirmed by N and G protein detection after supernatant passage from plasmid transfected cells at 2 dpi (see 4.3.1). Magenta, CedPV G and CedPV N; blue: Hoechst 33342. Scale bar = 20 µm.

To further characterize rCedPV, replication kinetics on BSR-T7/5, Vero and A549 cells were compared. Both, Vero and BSR-T7/5 cells are commonly used cell lines for virus rescues. While BSR-T7/5 cells have a defect in interferon type I induction (Habjan et al., 2008) Vero cells have an interferon-gene deletion (Desmyter et al., 1968; Rhim and Schell, 1967). In contrast, A549 cells are considered IFN competent and are derived from the human lung (Tanabe et al., 2003).

After infection with rCedPV at an MOI of 0.01, supernatant samples were collected at 0, 16, 24, 72, and 96 hpi and the infectious titres (pfu/ml) were determined by titration on the respective cell lines (see 4.3.2). At 72 hpi, the infectious virus titres increased to 4.2×10^5 pfu/ml, 1.9×10^6 pfu/ml, and

3×10^4 ffu/ml on BSR-T7/5, Vero, and A549 cells, respectively, and then stagnated (Figure 24). During the early stages, the titres on Vero cells were lower than on BSR-T7/5 cells. These data indicated efficient replication in the three tested cell lines, but also revealed cell line specific differences in virus replication. This could be due to cell line specific differences in genome replication, virus release, or antiviral cellular responses. rCedPV C-R68K exhibited end titres of 1.3×10^6 pfu/ml, 1.5×10^6 pfu/ml and 2.3×10^4 ffu/ml in the respective cell lines, indicating that the amino acid exchange did not substantially alter virus growth (Supplement 11). However, since effects on C-protein functions could not be excluded, all following experiments were performed with rCedPV.

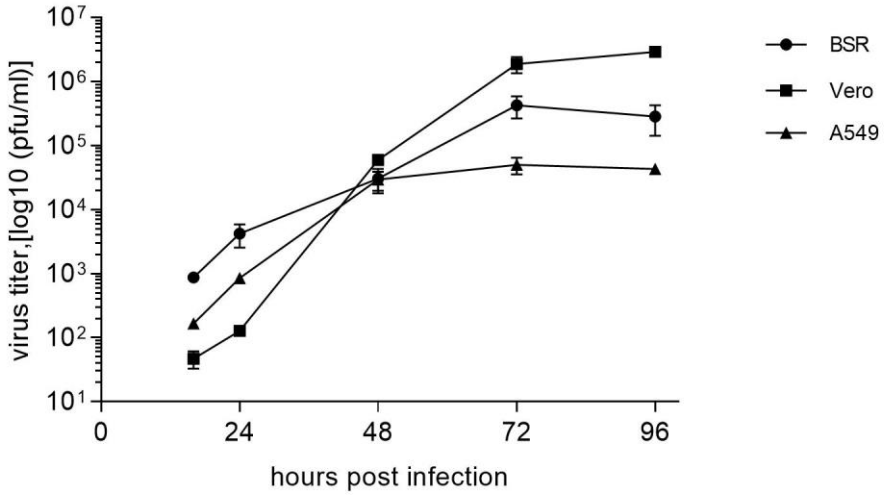

Figure 24: Growth curves of rCedPV on BSR-T7/5, Vero and A549 cells. BSR-T7/5, Vero and A549 cells were infected with rescued rCedPV (see 4.3.1) and the titer of the replication kinetics was determined on the respective cell lines (see 4.3.5). In BSR-T7/5 and A549 cells, rCedPV grew to 10- and 60-fold lower end titers compared to Vero cells. Results are depicted as the mean of three replicates and error bars indicate the standard deviation.

Cell-cell fusion activity of CedPV infected, ephrin-B2 negative HeLa cells was shown to depend on trans-complementation of EphrinB2 (Laing et al., 2018). To assess whether reduced virus growth of rCedPV in A549 cells was accompanied with less efficient cell syncytia formation, infected cell cultures from growth curves described above, were monitored by bright field microscopy.

Notably, different effects of rCedPV on cell morphology and cytopathic effects were observed. Syncytia were detectable in BSR-T7/5, Vero and A549 cells at 2 dpi, 3 dpi and 4 dpi respectively (Figure 25, arrow heads), indicating distinct time courses of syncytia formation. Earlier appearance of syncytia in BSR-T7/5 cells was accompanied with a strong CPE at 4 dpi , whereas no obvious signs of CPE were observed in Vero and A549 cells. These data indicated that CPE in the infected cell cultures not strictly correlated with the differences in the replication kinetics described above (Figure 24).

However, productive infection of A549 cells and late cell-cell fusion and rather small syncytia in A549 cells indicated that these cells could represent a suitable cell line model for rCedPV inhibitor screens and imaging based automated quantification (see 5.2.3).

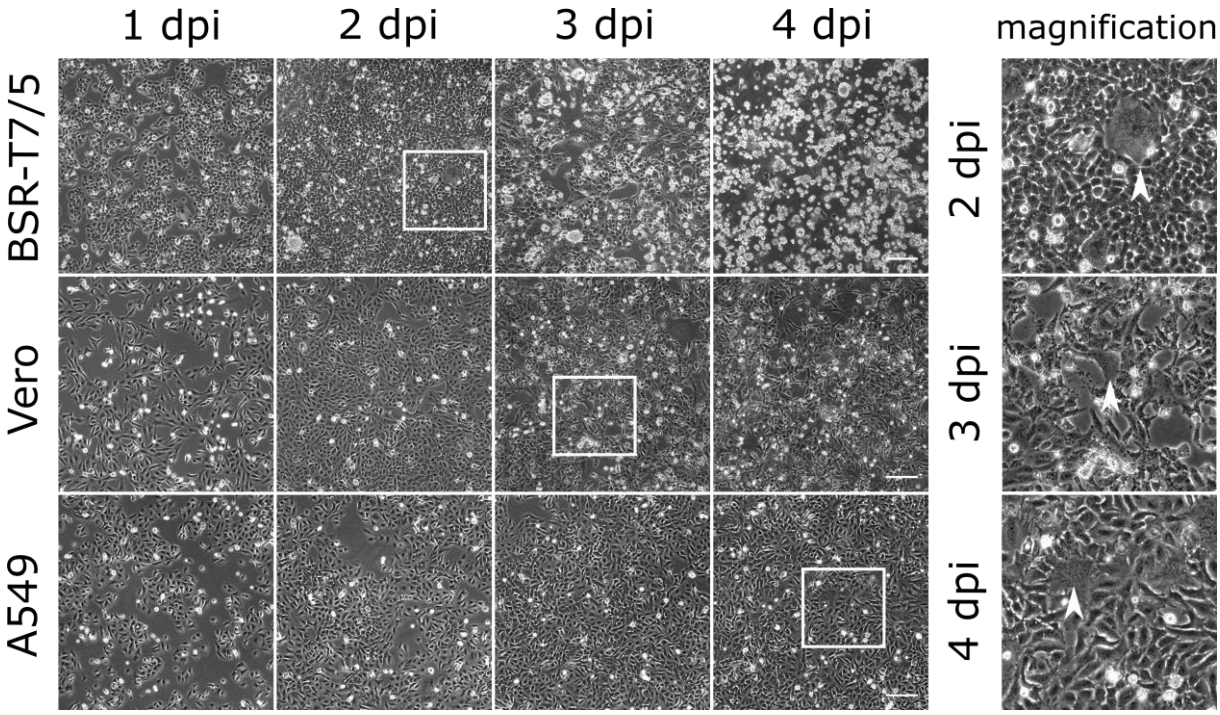

Figure 25: Syncytia formation and CPE in BSR-T7/5, Vero, and A549 cells. After infection of cells with an MOI of 0.01, the morphology of the cells was monitored by bright field microscopy up to day 4 post infection. Detail views (white squares) with syncytia are indicated by arrowheads and are depicted on the right. Scale bars = 200 µm.

5.2.3. Establishment of a quantitative analysis pipeline for siRNA inhibitor screens

In order to investigate the role of cellular factors in CedPV infected cells and to screen for potential host gene directed inhibitory factors, an imaging based screening and quantitative analysis pipeline were established. To this end, different host and viral genes were targeted with a siRNA-pool either targeting virus or selected cellular mRNAs, each consisting of 15 or 30 different siRNAs, respectively (sense and antisense). Since cellular targets were targeted, siRNA transfection was performed two days before rCedPV infection, in order to achieve knock-downs at the timepoint of infection.

The overall working procedure of the siRNA-inhibitor screen is depicted in Figure 26. After siRNA transfection (see 4.1.2) in 1×10^4 A549 cells in a 96-well format, the cells were incubated for 48 h (Figure 26, ①) prior to the infection with CedPV at an MOI of 0.1 (Figure 26, ②). 24 h later the cells were fixed and immunostained for CedPV G and cell nuclei (Hoechst33342) (Figure 26, ③). The 96-well plates were scanned with a Leica DMi8 THUNDER imaging system with six field of views per well (Figure 26, ④) and the acquired data files was conducted to bioinformatic quantification using the Arivis-Vision 4D software (see 4.5.4). Thereby, the numbers of infected cells and the total number of cells

per field of view were determined in one batch (Figure 26, ⑤). The latter was also used to assess toxic effects of the siRNAs on cell growth.

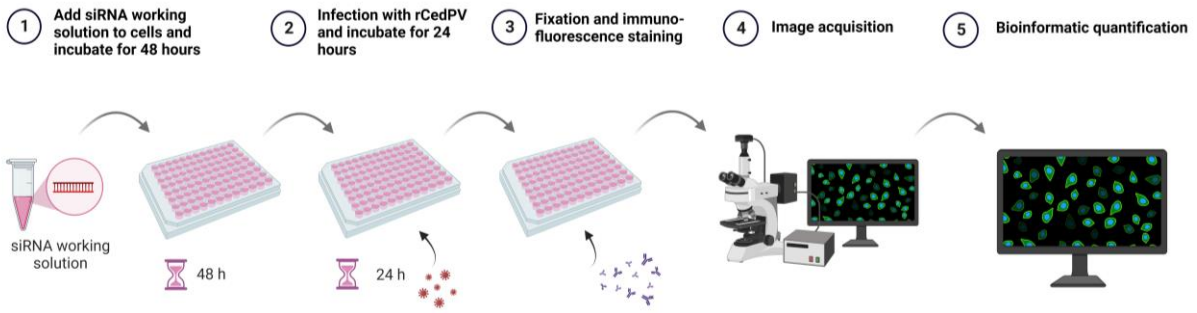

Figure 26: Schematic presentation of the siRNA screening workflow. **(1)** The siRNA transfection mix was added to the cells (see 4.1.2). After 48 h incubation **(2),** the transfected cells were infected with rCedPV. **(3)** 24 h later the cells were fixed, immunostained for CedPV G protein, and nuclei were stained with Hoechst33342. **(4)** The plates were scanned in a motorized fluorescence microscope by acquisition of six field of views per well. **(5)** Numbers of Hoechst3334 and CedPV G positive cells were automatically quantified by the bioinformatic pipeline (see 4.5.4). The percentage of infected cells was determined and the number of infected cells was used as a measure for cell growth inhibitory effects of the siRNAs.

The workflow was used to carry out siRNA screens against several viral and host factors. Since, pre-existing siRNA libraries against human genes were used for inhibition of host factors, human A549 cells susceptible to CedPV infection (see 5.2.2) were used.

As depicted in Figure 27A, each siRNA-Pool and combinations of siRNA-Pools were tested in triplicates. Of the antiviral siRNA Pools (L-1, L-2, L-3, N-1 and N-2), L-1, L-2 were used for additional triplicates (L-1.2 and L-2.2). Quantification of cell viability by comparing the number of cells at 3 days post transfection, no indications of toxic cell growth inhibitory effects of the siRNA-Pools were observed (Figure 27B). Only KIF11 directed siRNAs, known to induce cell death by downregulation of KIF11 protein, led to reduction of the cell numbers to 3952.

Whereas 6.7 % and 6.4 % infected cells were observed after transfection of negative controls consisting of irrelevant siRNAs not targeting any humans, mouse, rat, or dog mRNA sequences, inhibition of rCedPV infection to 2.6, 2.8, and 2.4, 2.0 % was observed for the virus specific siRNA Pools L-1, L-2, N-1, and N-2 at a p-value of <0.1 (Figure 27C). Although L-3 inhibition was not statistically significant reduction to a mean of 2.9 % indicated that L-3 exhibited inhibitory activities as well. Even though only a 3.2-fold reduction in the number of infected cells could be recognized, these data demonstrate the feasibility of the analysis pipeline to detect and quantify inhibitory effects on CedPV infection. While siRNA pools directed against *Henipavirus* entry receptors, ephrin(EFN)B2, EFNB3 and EFNA5 resulted in an increase of rCedPV infection to 10.2, 9.6, 10.3 %, targeting of EFNB1 resulted in an inhibition of infection to 3.8 %. A combination of pools directed against EFNB1, EFNB2 and EFNB3 resulted in a decrease to 4.7 % infected cells whereas a combination of EFNB1, EFNB2, EFNB3 and EFNA5 resulted in an increase to 7.1 % infected cells. A selection of siRNA pools against promising host

factors, including sphingosine-1-phosphate lyase (SGPL1), ceramide transfer protein (CERT1), acid sphingomyelinase-like phosphodiesterase 3b (SMPDL3B), neutral ceramidase B (ASAH2B), and the kinesin-like protein KIF11 (KIF11) resulted in an increase of rCedPV infection to 7.9, 9.7, 7.8, 7.4 and 10.8 % (Figure 27C). However, targeting of host factors resulted exclusively for KIF 11 in a statistically significant increase of infected cells.

A

	1	2	3	4	5	6	7	8	9	10
A	NEG	MOCK	KIF11	L-1	L-1	L-2	L-2	L-3	N-1	N-2
B	NEG	MOCK	KIF11	L-1	L-1	L-2	L-2	L-3	N-1	N-2
C	NEG	MOCK	KIF11	L-1	L-1	L-2	L-2	L-3	N-1	N-2
D	EFNB1	EFNB2	EFNB3	EFNA5	EFNB1/ 2/3	EFN-B1/ 2/3/A5	SGPL1	CERT1	SMPDL3 B	ASAH2B
E	EFNB1	EFNB2	EFNB3	EFNA5	EFNB1/ 2/3	EFN-B1/ 2/3/A5	SGPL1	CERT1	SMPDL3 B	ASAH2B
F	EFNB1	EFNB2	EFNB3	EFNA5	EFNB1/ 2/3	EFN-B1/ 2/3/A5	SGPL1	CERT1	SMPDL3 B	ASAH2B

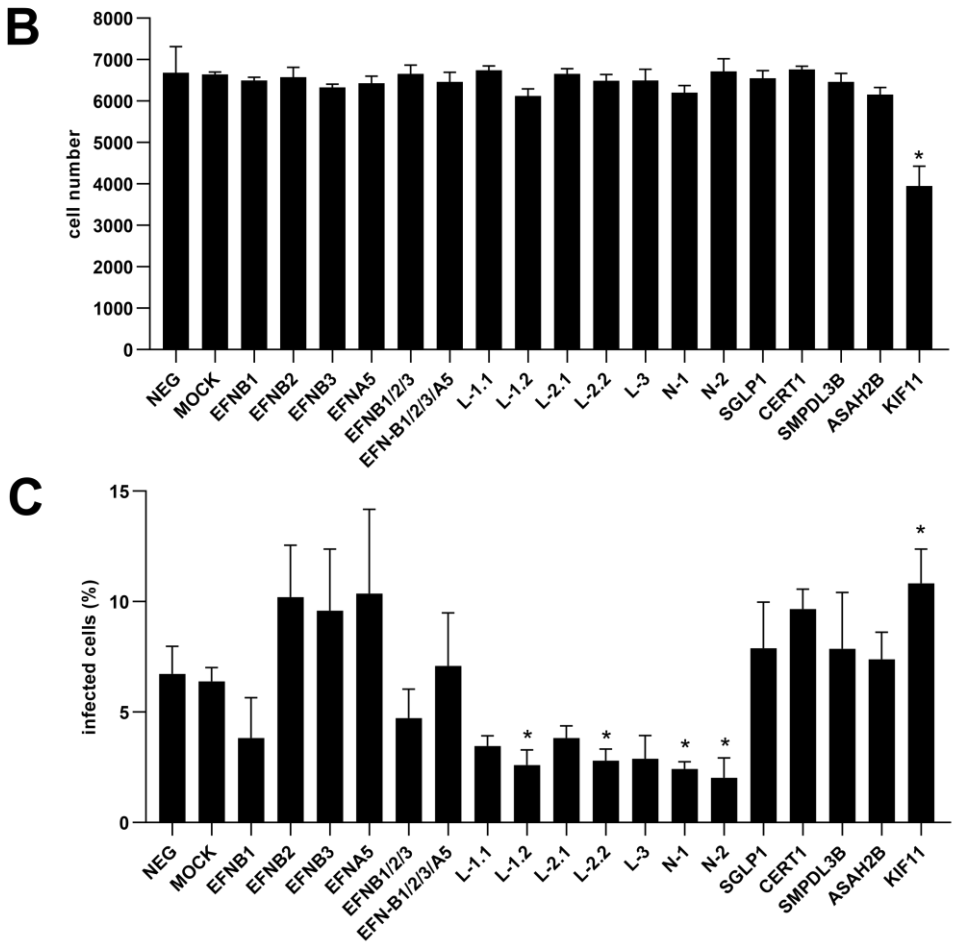

Figure 27: Screening with several siRNA directed against viral or host factors. (A) Schematic presentation of each siRNA-Pool and combinations of siRNA-Pools tested in triplicates. **(B)** The total number of cells in each sample was counted to assess toxic effects of the siRNAs on cell growth. **(C)** The different siRNAs (see 3.8) were transfected (see 4.1.2) into A549 cells and after an 48 h incubation time infected with CedPV (MOI 0.1) and incubated for another 24 h, following an immunostaining (see 4.5.1) against CedPV G. Six images per sample were acquired with a Leica thunderbird imager DMi8 and a 10×/0.12 dry N PLAN objective using the LAS X (v3.7.423463) software. Afterwards, the cells were counted with an automated image analysis pipeline performed with Arivis Vision4D (see 4.5.4). Results are depicted as the mean of three replicates and error bars indicate the standard deviation. Significance against the mock control is indicated by stars (Dunnett's: p-value of <0.1).

With the development of the siRNA screening pipeline and proof of concept for antiviral siRNA pools, the recombinant CedPV clone (see 3.10) was used as a backbone to insert various fluorescence reporter genes in order to optimize the analysis workflow by allowing direct virus quantification in live, unstained samples. Moreover, reporter fluorescence intensities could be used as a direct measure of virus gene expression and localization of the reporter proteins to the nucleus may improve automated recognition and counting of CedPV infected cells. To this end, three different reporter CDS were inserted in the full length cDNA plasmid clone CedPV. These included the nUnaG, TurboFP635 and nTurboFP635. Nuclear localization of the reporters was achieved by inserting an NLS derived from the SV40 large T antigen N-terminally fused to the reporter coding sequence. After insertion of an extra-cistron encoding the different reporter CDS between the P and M gene in the CedPV full length cDNA clone (see 4.7.2), the recombinant viruses were rescued.

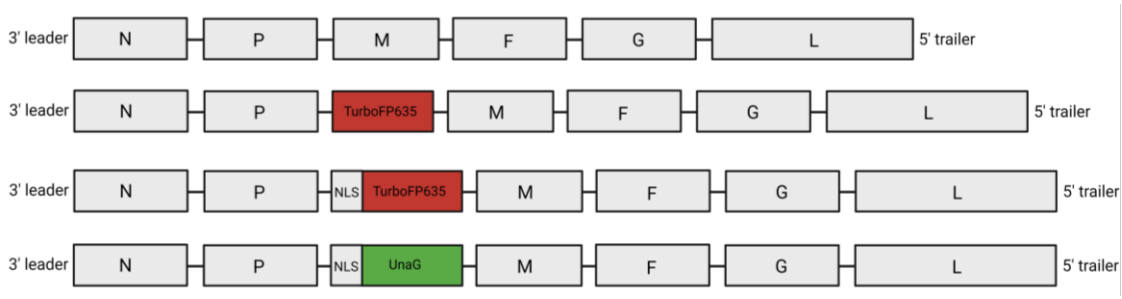

Figure 28: Schematic overview of constructed reporter encoding plasmids. Reporter genes encoding for the respective reporter proteins TurboFP635 as well as nuclear localizing nTurboFP635 and nUnaG were inserted as an extra-cistron between the P and M genes to maintain the expression levels of N and P. The cloning procedure is described in detail in chapter 4.7.

To verify reporter expression and localization, BSR-T7/5 cells were infected with the rescued viruses and the different reporters were observed by immunofluorescence imaging (Figure 29).

Infected cells were visible for all three reporter expressing viruses indicated by CedPV P in cytoplasmic IBs (grey) and the reporter expression (respective color, Figure 29). Both nUnaG and nTurboFP635 accumulated in the nuclei. In contrast, TurboFP635missing the NLS localized both cytoplasmatic and partially in the nuclei. Overall, these data indicate a successful rescue of the reporter expressing viruses and their expected localization in the cytoplasm or the nucleus.

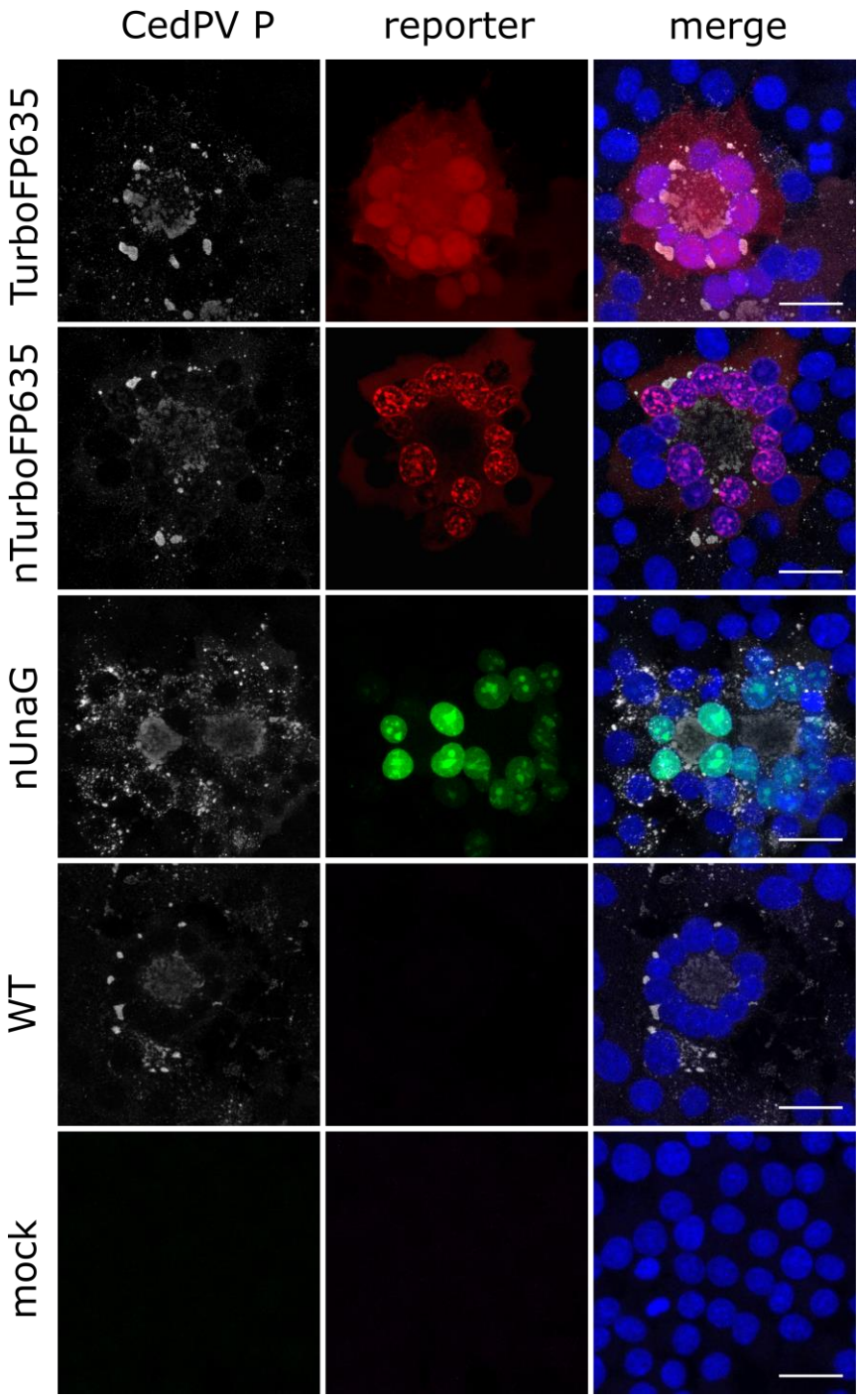

Figure 29: Immunofluorescence staining of different reporter-expressing rCedPV. BSR-T7/5 cells were infected with different reporter expressing viruses, (see 4.3.1) fixed 2 dpi and immunostained for CedPV P (see 4.5.1). Nuclei were stained using Hoechst 33342. Scale bar = 20 µm.

In summary, rCedPV was successfully rescued and characterized to allow functional studies of *Henipaviruses* at BSL-2 facilities. To this end, an imaging based screening and quantitative analysis pipeline was established to investigate the role of cellular factors and to screen for potential host gene directed inhibitory factors. This includes reporter expressing viruses to optimize the analysis workflow by allowing direct virus quantification in live, unstained samples.

6. Discussion

NiV is a highly pathogenic BSL-4 pathogen, which has caused several outbreaks in the past decades. Pigs serve as an intermediate host for NiV transmission from its bat reservoir to humans, where severe respiratory and neurological disease can develop (Chua et al., 1999; Lee et al., 1999; Yob et al., 2001). The extraordinarily large host range, lack of a vaccine and a case fatality rate over 70 % results in the classification as a high consequence BSL-4 pathogen (Luby and Broder, 2014). To understand why the virus constitutes a high-risk pathogen for livestock and humans, knowledge about virus replication and host responses in relevant cells and tissues is crucial. Beyond analysis of highly pathogenic BSL-4 *Henipaviruses*, it is also of utmost importance to have access to nonpathogenic *Henipaviruses* for comparative studies and to provide low biosafety level inhibitor and host factor screens. Most *in vitro* studies with NiV have been performed in conventional cell lines, and only few examples exist where NiV infection has been investigated in fully differentiated human BEC-ALI cultures (Escaffre et al., 2016; Sauerhering et al., 2017) mimicking the infection of respiratory epithelia. However, no studies in differentiated PBEC-ALI cultures are available, although pigs serve as a relevant intermediate host for transmission to humans through respiratory excretion (Chua et al., 1999).

Here, the time course of NiV infection in differentiated PBEC and FBEC-ALI cultures was characterized by immunofluorescence analysis, virus mRNA-quantification, and titration of released infectious virus. To achieve insights in the quality and dynamics of host-responses to NiV infection in the differentiated bronchial epithelium cultures, over a time period of 12 days infection kinetics were monitored and correlated with a quantitative high-resolution mass spectrometry analysis. Identification of all virus proteins and a total of 6345 host proteins at the different time points provided a comprehensive insight into the dynamics of NiV infection and resultant host responses. The data revealed a potent type I/II interferon response in infected PBEC-ALI cultures and broad upregulation of downstream antigen processing and MHC I presentation. The latter may contribute to the role of the respiratory epithelium not only as a physiological barrier but also as a priming site for the induction of adaptive immunity. Slow spread of the virus with strong cytopathic effects at infected areas, together with low levels of released infectious virus at the apical and basal sides of the PBEC-ALI cultures but increasing virus mRNA levels over time, further indicated limited release of infectious virions. Most likely, progeny virus remained cell associated and a model where cell associated virus may contribute to efficient NiV spread is suggested.

Furthermore, a reverse genetic system for CedPV was established to study *Henipavirus* replication and to perform virus inhibitor screenings at biosafety level 2. Although recombinant CedPV has already been described (Laing et al., 2018), availability is restricted and the here generated recombinant full length cDNA clone and derived recombinant rCedPV, together with an imaging based quantitative analysis pipeline represent a promising tool for future approaches related to the function of virus proteins, influence of host-factors and virus replication and *Henipavirus*-inhibitor screens at low biosafety levels.

6.1. Dynamics of NiV replication in PBEC- and FBEC-ALI cultures

Similar to previous studies in non-differentiated pig and human BEC (Sauerhering et al., 2016) infection of non-differentiated pig and ferret BEC (Figure 8) confirmed the susceptibility of the prepared primary bronchial cells. Moreover, faster appearance of a CPE with fragmentation of cell nuclei in FBEC cultures (Figure 8, arrowhead) indicated a higher resilience of PBECs to NiV infection. Disruption of the differentiated FBEC-ALI cultures from 5 dpi on (Figure 10B, arrowheads) and still rather continuous PBEC cell layers at 12 dpi (Figure 10A) indicated a higher resilience to NiV infection in differentiated PBEC as well. Even though strong CPE also appeared in differentiated PBEC in later phases of NiV infection (Figure 13), the PBEC-ALI cultures remained robust enough to allow studies on host cell responses for a time period of 12 days.

In contrast to non-differentiated primary BEC (Figure 8), the specific infectivity of NiV in the ALI-cultures was low, as indicated by immunofluorescence detection (Figure 9 and Figure 10) and mass spectrometry virus protein quantification (Figure 16) at 1 and 2 dpi after infection with a Vero specific cell titer of 2 x 10^6 pfu/well. However, continuous NiV replication and spread occurred as indicated by focal infection herds from 5 dpi on (Figure 10 and Figure 13), in PBEC-ALI cultures increasing mRNA levels from 1 dpi on (Figure 12) and mass spectrometry detection of all virus proteins (Figure 16) from 5 dpi on. The focal appearance of infection together with remarkable low levels of progeny virus release at the apical and the basal sides of the ALI-cultures (Figure 11) but increasing virus mRNA and protein levels in cell extracts, strongly indicated cell-to-cell spread of NiV in the ALI-cultures and that most of the newly formed virus may have remained cell associated. However, further experiments are required to quantify cell-associated NiV infectivity to confirm production of cell-associated infectious progeny virus.

In differentiated primary cultures of human airway epithelial cells, it was recently shown that cell-associated measles virus (MeV) infect monocyte-derived macrophages as a first stage of infection in a new host. Furthermore, dislodged infected epithelial patches and their expulsion through coughing and sneezing were discussed to contribute to the high reproductive number of MeV by increasing the virus survival time and delivery of high infectious doses to the next host (Hippee et al., 2021).

Moreover, MeV infected multinucleated giant cells have been reported to be released from human BEC-ALI cultures (Lin et al., 2021). In contrast to MeV-infected human BEC-ALI cultures, where apical, ciliated cell patches were infected without signs of cell death, NiV infection in the middle area of the PBEC-ALI cultures led to observed strong cytopathic effects in those cells. Apical cell layers were mostly preserved, as demonstrated by the integrity of cilia, tight-, and cell adherens junctions after infection of the PBEC-ALI cultures (Figure 13 and Figure 14). Whether those differences in BEC-ALI culture replication between MeV and NiV can be attributed to distinct virus specific mechanisms or whether host species specific factors contribute remains open. Previous characterization of NiV infected human BEC-ALI cultures revealed disruption of the epithelium integrity (Escaffre et al., 2016), indicating a comparable CPE as observed here in PBEC-ALI cultures.

However, despite of potential differences in cell tropism and CPE induction by MeV and NiV, as already discussed for MeV (Hippee et al., 2021) NiV transmission may be supported by cell-associated virus. Inhalation of cell associated virus may ensure a high local infectious dose and thus may increase efficiency of infection. Indeed, the amount of infectious airborne influenza A virus (IAV), porcine reproductive and respiratory syndrome virus (PRRSV), and porcine epidemic diarrhea virus (PEDV) increased with the size of exhaled aerosols (Alonso et al., 2015). Further increase could be postulated by exhalation of larger virus containing debris. This model and relevance of the ALI-culture based *in vitro* results is further supported by the presence of virus antigen positive cells debris in the respiratory tract lumen of NiV infected pigs with lung lesions (Mohd Nor et al., 2000). Taking into account that pigs develop a severe cough following NiV infection, the so called “one-mile cough” (Kulkarni et al., 2013), exhaled cell debris might play a major role in the rapid infection in swine populations.

6.2. Host response to NiV infection

The observation of a relative low level of infection in basal and apical cell layers (Figure 13 and Figure 14) could be due to the specific differentiation state and cell-specific molecular host response patterns. Using quantitative mass spectrometry, we considered the overall response pattern in the differentiated PBECs and did not distinguish between individual cell types. Interestingly, IAV infection in PBEC-ALI cultures was characterized by the destruction of ciliated cells, but maintenance of the barrier function. Destroyed ciliated cells were compensated by basal cells without further differentiation (Wu et al., 2016). In this study, NiV hardly affected ciliated cells but rather exclusively appeared in middle cell layers inducing severe CPE (Figure 13 and Figure 14), and thus differed from IAV infections. Comparatively intact basal cell layers, even at late phases of NiV infection (Figure 14), indicated similarities to IAV infections, as the basal cells may compensate for virus-induced cell loss.

In contrast to non-differentiated primary PBEC (Elvert et al., 2020), NiV infection robustly induced multiple factors involved in type I and type II interferon responses and other infection related pathways over its infection course in the differentiated PBEC-ALI cultures (Figure 15 and Figure 18). Previous studies described a lack of efficient type I IFN induction in NiV infected non-differentiated PBEC or human BEC-ALI cultures, which suggested a neglectable role of type I IFN in NiV pathogenesis. These low type I IFN levels have been considered a prerequisite for efficient replication in respiratory epithelia and airborne virus spread (Elvert et al., 2020; Escaffre et al., 2016). In contrast, a robust antiviral response is induced in the differentiated PBEC-ALI cultures in this study , with long term virus replication, virus spread and strong CPE in the late phase of infection. Comparable interferon response and subsequent expression of inflammation related genes was observed in experimentally infected ferrets (Leon et al., 2018), indicating that here described hosts responses may be closer to the *in vivo* situation, either because of the more differentiated infection model or the deeper host response-analysis by high resolution mass spectrometry.

The surprisingly low initial infection of PBEC-ALI cultures by NiV was not due to an immediate and broad type I interferon upregulation, as IFN-β and IFN-λ mRNA levels increased later during infection (Figure 15). Accordingly, it might be a result of the differentiation status of the cells resulting in mucus and cilia capturing particles or the different cell types and receptor variation. However, a rapid inhibitory response either by ALI culture handling or directly by virus recognition cannot be excluded, as the mRNA levels of pro-inflammatory cytokines IL-6 and IL-8 were elevated directly after infection (Figure 15). Nevertheless, downregulation of both cytokines at days 1 and 2 after infection together with increased IFN-β, IFN-λ, IL-6, and IL-8 mRNA levels starting at 5 dpi revealed that these host responses directly correlated with the level of virus replication and protein expression (virus spread and RNA levels in Figure 10 and Figure 12; NiV protein levels in Figure 16). This is in line with previous studies that revealed upregulated IFN-λ levels in differentiated human BEC after NiV infection (Sauerhering et al., 2017).

Although levels of all viral proteins (N, P, V, W, C and M) involved in host response escape (reviewed in (Pelissier et al., 2019)) increased at 5 dpi, they were not sufficient to negate type I and II interferon and related host responses in the late phases of the infection course (Table 7). However, continuous virus spread in the PBEC-ALI cultures revealed the capability of the virus to replicate in the context of observed host response patterns, including ISGs such as BST2, ADAR, IFIT2/3, ISG15, ISG20, MX1, MX2, OAS2, and OASL (Figure 20), which are inhibitory to multiple RNA viruses (reviewed in (Schoggins and Rice, 2011)). Whether antagonistic virus proteins enable efficient NiV replication in the context of the observed response patterns, and thus lead to a balance of progressive virus replication and host mediated restrictions, or whether DEG at 9 and 12 dpi already reflect a phase of virus inhibition requires further investigation.

As the main protein degradation system, proteasomes are involved in the protein quality control in all eukaryotic cells (Baker et al., 2014; Dimasuay et al., 2018). Around 80 % of cellular proteins are cleaved by that proteolytic machinery (Kammerl and Meiners, 2016). With pro-inflammatory stimuli the proteolytically subunits of the constitutive proteasome are exchanged with immunoproteasome subunits (PSMB8/9/10). Both virus-induced type I interferon and type II induce conversion to immunoproteasomes (Aki et al., 1994; Shin et al., 2006). They are rapidly induced by IFN-γ treatment in respiratory cells *in vitro* and murine gammaherpesvirus-68 (MHV-68) lung infection (Keller et al., 2015). IFN-γ and NF-κB dependent immunoproteasome upregulation was also observed for an NS1-deficient influenza A virus variant (Tisoncik et al., 2011). Among others, immunoproteasomes participate in the cleavage of viral proteins that follows the virus-derived antigen presentation via the major histocompatibility complex class I (MHC I) complex. Subsequent the presented virus-derived proteins can be recognized by CD8+ cytotoxic T cell (CTL) resulting in pathogen clearance (Basler et al., 2011; Kammerl and Meiners, 2016; Shin et al., 2006).

Induction of immunoproteasomes in the PBEC-ALI cultures by NiV infection, indicated by the increased expression of 20S subunits PSMB8, PSMB 9, and PSMB 10, together with the 11S subunit PSME2 and downregulation of the 19 S subunits PSMC1, PSMC2, PSMC3, PSMD4, and PSMD11 (Figure 21) most likely was also interferon-driven and positively influenced by antigen processing for peptide transport and MHC I antigen presentation. Concerted upregulation of TAP1/2, MHC I subunits, related chaperones, endopeptidases ERAP1 and ERAP2, and lysosomal/endosomal cathepsins S and L2 proteases (Figure 21) pointed towards antigen processing and presentation of endogenous proteins.

Cathepsin S is expressed in antigen-presenting cells (APCs) and plays a critical role in the presentation of exogenous antigens by the major histocompatibility complex class II (MHC II) (Riese et al., 1996). However, presence of APCs can be excluded in the experimental setting due to selection conditions for epithelial cells during PBEC preparation and cultivation (Fulcher et al., 2005). Together with the lack of MHC II-related factors in the mass spectrometry analysis, the cathepsins indicated increased protein degradation in endosomal compartments of the epithelial cells. Indeed, cathepsin S can be expressed in airway epithelial cells (Oei et al., 2004), and expression is induced under inflammatory conditions by IFN-γ (reviewed in (Brown et al., 2020)). Due to the upregulation of IFN-γ response-related genes (Figure 20) in the PBECs, cathepsin S upregulation might be a direct response to cytokine signaling. Cathepsin S plays a vital role in the generation of TAP-independent cross-presentation (Shen et al., 2004) of MHC I in the vacuolar recycling pathway (Basha et al., 2008) and it is conceivable that efficient NiV mediated upregulation of both, TAP-dependent and TAP-independent MHC I antigen presentation contribute to the establishment of an adequate adaptive immune response. This could also contribute to the MHC I cross-presentation of lysosomal/endosomal NiV antigens in the absence

of APCs (Mehrfeld et al., 2018). However, further experiments that directly confirm cathepsin S dependent MHC I cross-presentation of endosomal antigen are required.

Upregulation of components of the proteasome and the peptide loading complex (PLC) in NiV infection have been described before. However, induction of the immunoproteasomal major components in NiV infected endothelial cells, as indicated by selective upregulation of TAP1 and PSMB9 without PSMB8 and PSMB10, was considered imbalanced (Mathieu et al., 2011), although IFN-β and innate cytokines are induced in NiV-infected endothelial cells (Lo et al., 2010). Whereas the findings on type I and type II interferon responses (Figure 20) are in line with interferon induction in endothelial cells, differences in the level of immunoproteasome and MHC I upregulation suggest different capacities of endothelial cells and the here used differentiated PBEC-ALI cultures to upregulate MHC I antigen presentation after NiV infection.

Whereas NiV antigen processing by immunoproteasomes may play an important role for efficient antigen presentation, proteasomal activities may also directly affect virus replication, as proteasome inhibitors have been shown to inhibit NiV budding (Wang et al., 2010). Most likely, mono-ubiquitination of the NiV matrix protein is affected by reduced proteasomal poly-ubiquitin turnover and thus virus budding is influenced (Wang et al., 2010). Although increased immunoproteasome protein levels were observed (Figure 21), which may also result in a higher turnover of poly-ubiquitinylated proteins, a pro-viral effect on NiV budding by elevated mono-ubiquitin levels remains highly speculative.

Overall, a complex host response pattern in the PBEC-ALI cultures with type I and II interferon signaling and downstream immunoproteasomal meditated MHC I antigen presentation was observed. Infection of PBEC leads to efficient NiV replication in the swine respiratory tract that triggers MHC I priming of adaptive immune responses to the virus. In the NiV infected pig, MHC I presentation may lead to both efficient CTL mediated elimination of infected cells and potentially CTL-mediated immunopathogenesis in the lung. However, in the PBEC-ALI cultures no CTL were present and a contribution of CTL responses to the observed CPE is excluded. Notably, after aerosol NiV infection of African green monkeys , severe respiratory disease went along with changes in cytokine response and activated CD8+ T cell numbers, but not with apparent neutralizing antibody titers over an 8-10 days course of disease (Cong et al., 2017), indicating the timeframe of experiments as a critical component.

Downregulation of RNA processing and metabolic pathways (Supplement 9) could be due to a general increase in cytopathic effects (Figure 13) or direct inhibition of cellular gene expression by the virus. Host manipulatory functions of HeV and NiV are often discussed in the context of nuclear accumulation of the matrix protein M (Bauer et al., 2014; Günther et al., 2020; Sun et al., 2014; Wang et al., 2010; Watkinson and Lee, 2016). For example, binding of M to the treacle protein results in silencing of rRNA

biogenesis (Rawlinson et al., 2018). However, enrichment of rRNA biosynthesis related terms were not identified, and thus could not confirm NiV M induced silencing of rRNA biogenesis in primary differentiated PBECs. Also, homeostasis of most ribosomal proteins with only a few factors up- and downregulated (Figure 19) suggested relatively constant levels of cellular protein synthesis over the infection period of 12 days. Accordingly, neither increasing protein accumulation in the course of cultivation nor substantial protein loss by the observed CPE in the late phase was detectable. Whether downregulation of spliceosome components (Figure 19) was related to host manipulatory M or other NiV protein functions, or whether it is an indirect outcome of the complex host response pattern and their effects on spliceosomal mRNA modification remains to be clarified.

Overall, the here presented data show, that the type I and II related innate immune response is upregulated in NiV infected PBEC-ALI cultures, which results in IFN-dependent upregulation of antigen processing and MHC I presentation. Thus, a model is proposed in which NiV infection and spread in differentiated PBECs is slowed by potent innate immune responses to the virus infection (Figure 30). In contrast to previous reports based on non-differentiated PBEC or endothelial cells, in NiV-infected differentiated PBEC-ALI cultures, limitations in interferon responses and incomplete immunoproteasome formation after NiV infection can be excluded. Altogether, the findings highlight the particular role of the respiratory epithelium not only as a physical barrier to virus infections but also indicate its role as a primary site of adaptive immune induction through NiV induced antigen processing and MHC I presentation.

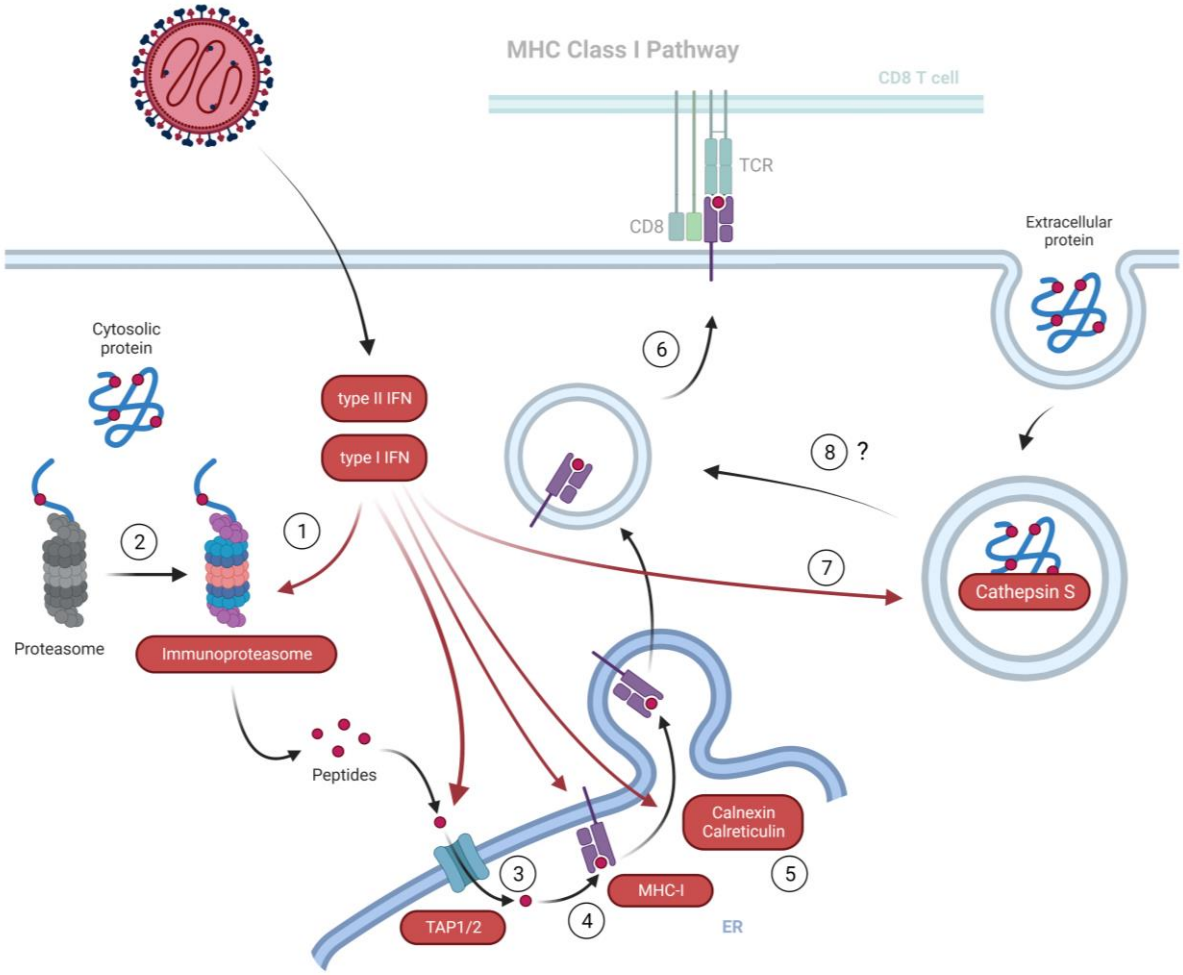

Figure 30: Model of type I/II IFN mediated upregulation of MHC I antigen presentation after NiV infection of PBEC-ALI cultures. (1) Upon pro-inflammatory stimuli (IFN type 1/2), **(2)** the proteolytically subunits of the constitutive proteasome are exchanged with immunoproteasome subunits leading to the conversion to immunoproteasomes. **(3)** Upregulation of the TAP-heterodimer, **(4)** MHC I subunits **(5)** and associated ER chaperons **(6)** indicate elevated peptide transport and MHC I antigen presentation. **(7)** Increased levels of cathepsin S indicate endosomal processing of extracellular antigens and **(8)** cross-presentation via MHC I. Overall, NiV infection and spread in differentiated PBECs might be slowed by a potent innate immune response and induce efficient processing of antigens for priming of CD8+ T-cell mediated immune responses.

6.3. Recombinant CedPV – A full virus BSL-2 tool for *Henipavirus* research

A reverse genetic system for the CedPV was established that allows functional studies of *Henipaviruses* at the BSL-2 biosafety level. Being the first nonpathogenic virus species in the *Henipavirus* genus, it allows research under less restricted circumstances than in a BSL-4 facility. Based on a here generated recombinant CedPV, an imaging based-screening and quantitative analysis pipeline was established to investigate the role of cellular factors and to screen for potential virus and host gene directed inhibitory factors. In order to generate rCedPV, a CedPV cDNA full length plasmid was constructed from synthetic DNAs and rCedPV was successfully rescued from the respective full length cDNA clone (Figure 22). In contrast to a previously described CedPV reverse genetics system, where newly formed virus was transferred from plasmid transfected BSR-T7/5 cells to Vero cells for further amplification (Laing et al., 2018), here both plasmid transfection and virus amplification were performed on the BSR-T7/5 hamster cells. Successful virus rescue was already detected by cell-syncytium formation in the transfected cell culture. CedPV infection of BSR-T7/5 cells was also confirmed by immunofluorescence with N and G protein distribution in IBs and vesicle-like structures, respectively (Figure 23) (Marsh et al., 2012; Vogt et al., 2005). The here used rescue protocol not only represents a simplified version of the previous protocol but can also considered more suitable, since hamsters represent a model for nonpathogenic *in vivo* replication of the CedPV (Schountz et al., 2019). Furthermore, highly pathogenic HeV and NiV replicate in baby hamster kidney cells (Aljofan et al., 2009).

Infection of BSR-T7/5, Vero and A549 cells with rescued rCedPV resulted in different effects on cell morphology and CPE (Figure 25). As mentioned above, BSR-T7/5 cells exhibited syncytia formation and CPE, which appeared faster than in Vero cells, whereas almost no syncytia were observed in A549 cells. Despite the difference in cell morphology, virus titers obtained on Vero cells were comparable to those reported for Vero cells (Figure 24) (Amaya et al., 2021; Laing et al., 2018) and the end titers were tenfold higher than in BSR-T7/5 cells. Thus, fast syncytium formation and appearance of CPE may decrease virus production in later phases of cultivation. However, although A549 cells were susceptible to rCedPV infection, loss of syncytia formation did not increase virus titres, as indicated by the lowest end titers of 4.7×10^4 ffu/ml at 96 hpi (Figure 24). Notably, also HeV and NiV replicate well in BSR and Vero cells, less efficient in HeLa, and worst in A549 cells (Aljofan et al., 2009).

It can be assumed that the suitability of BSR-T7/5 and Vero cells for CedPV replication may rely on defects in IFN-related antiviral responses in these cell lines. Vero cells, derived from the African green monkey kidney have a defect in interferon production (Desmyter et al., 1968; Rhim and Schell, 1967) and BSR-T7/5 cells have a defect in interferon type I induction (Habjan et al., 2008), while A549 cells are interferon competent (Tanabe et al., 2003). Productive infection of rCedPV in A549 cells, even at lower levels than in Vero and BSR T7/5 cells, indicated that host response antagonistic V and W

proteins expressed from HeV and NiV are not required for CedPV replication in an IFN-competent cellular environment, although the lack of these proteins in CedPV might contribute to less efficient replication.

As discussed in previous work (Aljofan et al., 2009), the differences between the cell types might also be a result of receptor sequence variation or expression. Indeed, in receptor Ephrin B2 negative HeLa cells, complementation of the receptor increased virus titres and syncytia formation (Laing et al., 2018), indicating that receptor usage might be more relevant than V and W protein expression. However, although CedPV is unable to effectively inhibit IFN responses (Lieu et al., 2015; Marsh et al., 2012) interference of CedPV encoded C protein with IRF7 phosphorylation and TLR 7/9 dependent interferon induction (Mathieu et al., 2012; Yamaguchi et al., 2014) might be sufficient to ensure replication in IFN-competent cell lines (Figure 24) and nonpathogenic replication *in vivo*. Off note, the non-silent mutation C-R68K in C, grew to comparable virus titer as the wildtype CedPV (Supplement 11). However, as no further experiments have been performed to characterize the impact of that mutation in C, it remains to be clarified whether this mutant could be used to assess C protein-dependent effects on virus replication.

In order develop a tool to investigate the role of cellular factors in CedPV replication and to screen for potential host gene or virus directed inhibitors, an imaging based screening and quantitative analysis pipeline was established (Figure 26). To this end, different host and viral genes were targeted with a pool of 15 or 30 different siRNAs prior to CedPV infection, immunofluorescent visualization and bioinformatic quantification. By the use of siRNA pools, the individual concentration of each siRNA is reduced and off-target gene silencing can be reduced (Hannus et al., 2014). Since pre-existing siRNA libraries against human genes were used for host cell gene knock down, A549 cells were used that are susceptible to CedPV infection (Figure 24) and that have a low cell-cell fusion activity after CedPV infection (Figure 25). The latter was considered important for the downstream quantification of infected cells after immunofluorescence staining or by fluorescence reporter expression.

While HeV and NiV use ephrin-B2 and ephrin-B3 as entry receptors (Bonaparte et al., 2005; Negrete et al., 2005), CedPV also enters cells through additional ephrin receptors (ephrin-B1, ephrin-A2 and ephrin-A5) but not ephrin-B3 (Laing et al., 2019; Pryce et al., 2020). Reason for this is a distinct receptor binding site of the CedPV G (Laing et al., 2019). Interestingly, transfection of ephrin-B1 siRNA pools resulted in less infected cells compared to the controls, while ephrin-B2, ephrin-B3 and ephrin-A5 specific siRNAs resulted in more infected cells (Figure 27A). Even though the results were not statistically significant, these trends might indicate a more effective utilization of ephrin-B1 in the absence of the other ephrin's. As discussed in previous work (Xu et al., 2012), lack of ephrin-B2, ephrin-B3 or ephrin-A5 might result in less competition between the receptor and therefore an increase in

the amount of infected cells. Off note, ephrin-B1 has a relatively high expression in the lung (Pryce et al., 2020) and consequently might be highly abundant in A549 cells. However, analysis of ephrin levels and confirmation of lower ephrin protein levels after siRNA transfection have to await to confirm robust protein knock-down. Combinational transfection without decreasing the individual siRNA pool concentration of ephrin-B1/B2/B3 and ephrin-B1/B2/B3/A5 resulted in comparable amounts of infected cells compared to the controls. It is important to note that, CedPV is also able to utilize the ephrin-A2 receptor, which was not targeted in these experiments (Laing et al., 2019). This suggests that a combination of ephrin-A2 and ephrin-B1 results in the optimal cell entry for CedPV. However, this remains speculative and has to be clarified in future experiments assessing which receptors or combinations are most sufficient for entry.

Use of KIF11 as a positive control for successful siRNA delivery, as visible by lower cell numbers after knock-down of that cell survival factor (Figure 27B) (Blangy et al., 1995; Ferenz et al., 2010), largely excluded inefficient siRNA RNA delivery to the A549 cells. Since knockdown of KIF11 led to a reduced cell number (Figure 27A) the increase in the number of infected cells most likely did not improve virus entry or replication but was most likely a result of interference with cell growth after infection.

In contrast to KIF11, and ephrin directed siRNA pools, siRNAs against four selected factors of the lipid metabolism (SGPL1, CERT1, SMPDL3B and ASAH2B), did not significantly affect CedPV infection and replication. These targets were chosen, since they have been validated in a pre-existing siRNA pool library (data not shown). Effects of those factors or involved pathways on virus replication has been demonstrated before: For example, SGPL1 has an antiviral activity during influenza A virus infection via the activation of the JAK/STAT signaling (Seo et al., 2010; Wolf et al., 2021) (Vijayan et al., 2017). The ceramide transport protein CERT1 is crucial for conversion of ceramide to sphingomyelin (Fukasawa et al., 1999; Hanada et al., 2003), which is essential for formation of lipid rafts (Ando et al., 2015) involved in entry, assembly and budding for many viruses (reviewed in (Suzuki and Suzuki, 2006)). SMPDL3B encodes for a lipid-modifying enzyme that negatively regulates the innate immunity (Heinz et al., 2015). Neutral ceramidase B also known as ASAH2B is regulating ceramide levels and inhibition of ceramidase results in an increased levels of ceramide (Simoes et al., 2022). As stated above, neither of the siRNAs directed against those selected factors affected CedPV infection or replication significantly. Whether a slight increase in the number of infected cells after CERT1 siRNA transfection indicates some positive effects on CedPV replication and whether there is a specific involvement of the respective lipid metabolism pathway remains to be clarified.

Whereas targeting of host factors not or rather inefficiently affected CedPV infection, targeting of the essential virus genes N and L led to significant reduction of CedPV infection (Figure 27). Even though further optimization is required to increase efficiency of infection in negative controls, these data

demonstrate that the established siRNA-based screening protocol, with an automated, imaging-based analysis pipeline (see 4.5.4) for quantification of CedPV infection is a valid tool for future screening approaches.

With development of the siRNA screening pipeline and proof of concept for antiviral siRNA pools, various fluorescence reporter-expressing viruses were generated for future direct virus quantification. To this end, reporter genes encoding for TurboFP635 and nuclear localizing variants of TurboFP635 and UnaG were inserted in the rCedPV (Figure 28). While TurboFP635 is a commonly used constitutively red fluorescent protein, UnaG is a cofactor-dependent green fluorescent protein, which utilize bilirubin as its ligand. It is smaller than most common reporter genes, has higher pH tolerance and is oxygen independent (Kumagai et al., 2013). Availability of such viruses could fasten the imaging workflow and allow implementation of high-content screening platforms. Moreover, reporter fluorescence intensities could be used as a direct measure of virus gene expression and localization of the reporter proteins to the nucleus may facilitate automated recognition and counting of CedPV infected cells. Infection of BSR-T7/5 cells with the reporter-expressing rCedPV resulted in the expected distribution in the cytoplasm or the nuclei of the respective reporters (Figure 29). Partially fragmented areas observed for the nuclear localizing reporter might be a result of the fixation process or an overexpression. Overall, a reverse genetic system for CedPV was established to study *Henipaviruses* replication at the biosafety level 2. Together with an imaging based quantitative analysis pipeline this provides a promising tool for future approaches related to the function of virus proteins, influence of host-factors and virus replication and *Henipavirus*-inhibitor screens at low biosafety levels.

7. Summary

The respiratory epithelium acts as both, a barrier of the respiratory tract to Nipah virus (NiV) entry and at the same time as a significant determinant of virus shedding. Both, for humans and pigs, replication in the respiratory tract epithelia is considered a major factor in transmission to other hosts. To understand why the virus constitutes a high-risk pathogen for livestock and humans, knowledge about viral replication and host responses in relevant cells and tissues is crucial. Most *in vitro* studies, however, have been performed in conventional cell lines or non-differentiated lung cells. Only a few examples exist where *Henipavirus* infections have been investigated in fully-differentiated lung epithelial cell models.

Thus, one aim of this thesis was to investigate infection, replication, spread and host protein dynamics of NiV in primary bronchial epithelial cells (BEC) cultivated at the air-liquid-interphase (ALI). By immunofluorescence imaging, the NiV infection dynamics in BEC-ALI cultures were monitored over a 12 day time course, in order to provide detailed information about the infection process in the respiratory epithelium of pigs and ferrets. Compared to undifferentiated primary BEC, the specific infectivity of NiV in BEC-ALI cultures was low. Infections remained focal and complete infection of the cultures was not observed, even at 12 dpi. Analysis of viral titers and viral mRNA indicated a limited virion release from the infected ALI-cultures while most of the newly synthesized NiV-RNA remained cell associated. Immunofluorescence analysis of cross sections from infected ALI-cultures revealed large infected areas that exhibited a strong cytopathic effect (CPE). Disruption of the epithelium resulted in apical release of virus antigen-positive cell detritus while ciliated areas and basal cells were less affected. From these data it was concluded, that NiV transmission could be supported by exhalation of cell debris associated NiV and thus may contribute to rapid spread of infection in swine populations.

A second aim was to explore the dynamics of host responses to NiV infection in differentiated BEC-ALI culture and to assess whether this differs to conventional cell line data available from literature. Even though strong CPE appeared in later phases of NiV infection, at least the porcine PBEC-ALI cultures remained robust enough to allow protein sampling over 12 days infection course. Subsequent MS-based proteomics enabled unprecedent insight in complex cell culture response upon NiV infection. Previous reports indicated a lack of efficient interferon type I induction in non-differentiated pig or human BEC which were considered a prerequisite for efficient replication in the respiratory epithelium and virus spread. In contrast to non-differentiated pig BEC (PBEC), in PBEC-ALI cultures multiple factors involved in interferon responses were upregulated upon NiV infection. Thereby it was demonstrated that NiV infection induced a robust innate immune response upon infection with elevated components of antigen processing and presentation resulting in the conversion from the constitutive proteasome

to the immunoproteasome. In contrast to previous reports about NiV-infected non-differentiated PBEC or endothelial cells, incomplete immunoproteasome formation and limitations in interferon response could be excluded. Thus, a model is proposed in which NiV infection and spread in differentiated PBECs is slowed by potent innate immune responses to the virus infection. Overall, the findings highlight the important role of the respiratory epithelium not only as a physical barrier to virus infections but also indicate its role as a primary site of adaptive immune induction through NiV induced antigen processing and MHC I presentation.

Finally, to allow functional studies of *Henipaviruses* at the BSL-2 biosafety level a recombinant CedPV was generated and rescued. An imaging based screening and quantitative analysis pipeline was established to investigate the role of cellular factors and to screen for potential virus and host gene directed inhibitory factors. Accordingly, different host and viral genes were targeted with a siRNA-pool either targeting virus or selected cellular mRNAs followed by the infection with the CedPV and the quantification of infected cells. With proof of concept of the siRNA screening pipeline, the recombinant CedPV clone was used as a backbone to insert various fluorescence reporter genes in order to optimize the analysis workflow by allowing direct virus quantification in live, unstained samples. Consequently, this thesis provides a valuable proof for future approaches related to the function of virus proteins, influence of host-factors and virus replication and *Henipavirus*-inhibitor screens at low biosafety levels.

8. References

Abbott, A. 2003. Biology's new dimension. *Nature*. 424:870-872.

Aken, B.L., P. Achuthan, W. Akanni, M.R. Amode, F. Bernsdorff, J. Bhai, K. Billis, D. Carvalho-Silva, C. Cummins, P. Clapham, L. Gil, C.G. Girón, L. Gordon, T. Hourlier, S.E. Hunt, S.H. Janacek, T. Juettemann, S. Keenan, M.R. Laird, I. Lavidas, T. Maurel, W. McLaren, B. Moore, D.N. Murphy, R. Nag, V. Newman, M. Nuhn, C.K. Ong, A. Parker, M. Patricio, H.S. Riat, D. Sheppard, H. Sparrow, K. Taylor, A. Thormann, A. Vullo, B. Walts, S.P. Wilder, A. Zadissa, M. Kostadima, F.J. Martin, M. Muffato, E. Perry, M. Ruffier, D.M. Staines, S.J. Trevanion, F. Cunningham, A. Yates, D.R. Zerbino, and P. Flicek. 2017. Ensembl 2017. *Nucleic Acids Res*. 45:D635-D642.

Aki, M., N. Shimbara, M. Takashina, K. Akiyama, S. Kagawa, T. Tamura, N. Tanahashi, T. Yoshimura, K. Tanaka, and A. Ichihara. 1994. Interferon-gamma induces different subunit organizations and functional diversity of proteasomes. *J Biochem*. 115:257-269.

Albariño, C., M. Foltzer, J. Towner, L. Rowe, S. Campbell, C. Jaramillo, B. Bird, D. Reeder, M. Vodzak, P. Rota, M. Metcalfe, C. Spiropoulou, B. Knust, J. Vincent, M. Frace, S. Nichol, P. Rollin, and U. Ströher. 2014. Novel Paramyxovirus Associated with Severe Acute Febrile Disease, South Sudan and Uganda, 2012. *Emerging Infectious Disease journal*. 20:211.

Aljofan, M., S. Saubern, A.G. Meyer, G. Marsh, J. Meers, and B.A. Mungall. 2009. Characteristics of Nipah virus and Hendra virus replication in different cell lines and their suitability for antiviral screening. *Virus Research*. 142:92-99.

Alonso, C., P.C. Raynor, P.R. Davies, and M. Torremorell. 2015. Concentration, Size Distribution, and Infectivity of Airborne Particles Carrying Swine Viruses. *PLoS One*. 10:e0135675.

Amaya, M., H. Cheng, V. Borisevich, C.K. Navaratnarajah, R. Cattaneo, L. Cooper, T.W. Moore, I.N. Gaisina, T.W. Geisbert, L. Rong, and C.C. Broder. 2021. A recombinant Cedar virus based high-throughput screening assay for henipavirus antiviral discovery. *Antiviral Research*. 193:105084.

Ando, J., M. Kinoshita, J. Cui, H. Yamakoshi, K. Dodo, K. Fujita, M. Murata, and M. Sodeoka. 2015. Sphingomyelin distribution in lipid rafts of artificial monolayer membranes visualized by Raman microscopy. *Proceedings of the National Academy of Sciences*. 112:4558-4563.

Andri et mult. al. S. 2021. DescTools: Tools for Descriptive Statistics. R package version 0.99.44, https://cran.r-project.org/package=DescTools.

Ang, B.S.P., T.C.C. Lim, and L. Wang. 2018. Nipah Virus Infection. *J Clin Microbiol*. 56:e01875-01817.

Ashburner, M., C.A. Ball, J.A. Blake, D. Botstein, H. Butler, J.M. Cherry, A.P. Davis, K. Dolinski, S.S. Dwight, J.T. Eppig, M.A. Harris, D.P. Hill, L. Issel-Tarver, A. Kasarskis, S. Lewis, J.C. Matese, J.E. Richardson, M. Ringwald, G.M. Rubin, and G. Sherlock. 2000. Gene ontology: tool for the unification of biology. The Gene Ontology Consortium. *Nat Genet*. 25:25-29.

Audsley, M.D., D.A. Jans, and G.W. Moseley. 2016. Nucleocytoplasmic trafficking of Nipah virus W protein involves multiple discrete interactions with the nuclear import and export machinery. *Biochemical and Biophysical Research Communications*. 479:429-433.

Baker, T., H. Bach, R. Gamelli, R. Love, and M. Majetschak. 2014. Proteasomes in Lungs From Organ Donors and Patients With End-Stage Pulmonary Diseases. *Physiological research / Academia Scientiarum Bohemoslovaca*. 63.

Bals, R., C. Beisswenger, S. Blouquit, and T. Chinet. 2004. Isolation and air–liquid interface culture of human large airway and bronchiolar epithelial cells. *Journal of Cystic Fibrosis*. 3:49-51.

Bankowski, R.A., R.E. Corstvet, and G.T. Clark. 1960. Isolation of an Unidentified Agent from the Respiratory Tract of Chickens. *Science*. 132:292-293.

Basha, G., G. Lizée, A.T. Reinicke, R.P. Seipp, K.D. Omilusik, and W.A. Jefferies. 2008. MHC Class I Endosomal and Lysosomal Trafficking Coincides with Exogenous Antigen Loading in Dendritic Cells. *PLoS One*. 3:e3247.

Basler, C.F. 2012. Nipah and hendra virus interactions with the innate immune system.

Basler, M., U. Beck, C.J. Kirk, and M. Groettrup. 2011. The antiviral immune response in mice devoid of immunoproteasome activity. *J Immunol*. 187:5548-5557.

Battisti, A.J., G. Meng, D.C. Winkler, L.W. McGinnes, P. Plevka, A.C. Steven, T.G. Morrison, and M.G. Rossmann. 2012. Structure and assembly of a paramyxovirus matrix protein. *Proc Natl Acad Sci U S A*. 109:13996-14000.

Bauer, A., S. Neumann, A. Karger, A.-K. Henning, A. Maisner, B. Lamp, E. Dietzel, L. Kwasnitschka, A. Balkema-Buschmann, G.M. Keil, and S. Finke. 2014. ANP32B Is a Nuclear Target of Henipavirus M Proteins. *PLoS One*. 9:e97233.

Becker, N., A. Heiner, and A. Maisner. 2022. Cytosolic Nipah Virus Inclusion Bodies Recruit Proteins Without Using Canonical Aggresome Pathways. *Frontiers in Virology*. 1.

Behlke, M.A. 2006. Progress towards in Vivo Use of siRNAs. *Molecular Therapy*. 13:644-670.

Bharaj, P., Y.E. Wang, B.E. Dawes, T.E. Yun, A. Park, B. Yen, C.F. Basler, A.N. Freiberg, B. Lee, and R. Rajsbaum. 2016. The Matrix Protein of Nipah Virus Targets the E3-Ubiquitin Ligase TRIM6 to Inhibit the IKKε Kinase-Mediated Type-I IFN Antiviral Response. *PLoS pathogens*. 12:e1005880-e1005880.

Bindea, G., B. Mlecnik, H. Hackl, P. Charoentong, M. Tosolini, A. Kirilovsky, W.-H. Fridman, F. Pagès, Z. Trajanoski, and J. Galon. 2009. ClueGO: a Cytoscape plug-in to decipher functionally grouped gene ontology and pathway annotation networks. *Bioinformatics*. 25:1091-1093.

Birnboim, H.C., and J. Doly. 1979. A rapid alkaline extraction procedure for screening recombinant plasmid DNA. *Nucleic Acids Res*. 7:1513-1523.

Blangy, A., H.A. Lane, P. d'Hérin, M. Harper, M. Kress, and E.A. Niggt. 1995. Phosphorylation by p34cdc2 regulates spindle association of human Eg5, a kinesin-related motor essential for bipolar spindle formation in vivo. *Cell*. 83:1159-1169.

Blom, R.A.M., S.T. Erni, K. Krempaská, O. Schaerer, R.M. van Dijk, M. Amacker, C. Moser, S.R.R. Hall, C. von Garnier, and F. Blank. 2016. A Triple Co-Culture Model of the Human Respiratory Tract to Study Immune-Modulatory Effects of Liposomes and Virosomes. *PLoS One*. 11:e0163539.

Bojkova, D., M. Bechtel, K.M. McLaughlin, J.E. McGreig, K. Klann, C. Bellinghausen, G. Rohde, D. Jonigk, P. Braubach, S. Ciesek, C. Münch, M.N. Wass, M. Michaelis, and J. Cinatl, Jr. 2020. Aprotinin Inhibits SARS-CoV-2 Replication. *Cells*. 9.

Bonaparte, M.I., A.S. Dimitrov, K.N. Bossart, G. Crameri, B.A. Mungall, K.A. Bishop, V. Choudhry, D.S. Dimitrov, L.-F. Wang, B.T. Eaton, and C.C. Broder. 2005. Ephrin-B2 ligand is a functional receptor for Hendra virus and Nipah virus. *Proceedings of the National Academy of Sciences*. 102:10652-10657.

Brown, R., S. Nath, A. Lora, G. Samaha, Z. Elgamal, R. Kaiser, C. Taggart, S. Weldon, and P. Geraghty. 2020. Cathepsin S: investigating an old player in lung disease pathogenesis, comorbidities, and potential therapeutics. *Respir Res*. 21:111.

Buchholz, U.J., S. Finke, and K.K. Conzelmann. 1999. Generation of bovine respiratory syncytial virus (BRSV) from cDNA: BRSV NS2 is not essential for virus replication in tissue culture, and the human RSV leader region acts as a functional BRSV genome promoter. 73:251–259.

Calain, P., and L. Roux. 1993. The rule of six, a basic feature for efficient replication of Sendai virus defective interfering RNA. *J Virol*. 67:4822-4830.

Cameron, A.E., and D.F. Eggers. 1948. An Ion ``Velocitron''. *Review of Scientific Instruments*. 19:605-607.

Carré, H. 1905. Sur la maladie des jeunes chiens. *Comptes Rendus De L'académie Des Sciences*. 140:1489–1491.

Castellani, S., S. Di Gioia, L. di Toma, and M. Conese. 2018. Human Cellular Models for the Investigation of Lung Inflammation and Mucus Production in Cystic Fibrosis. *Analytical Cellular Pathology*. 2018:3839803.

Chadha, M.S., J.A. Comer, L. Lowe, P.A. Rota, P.E. Rollin, W.J. Bellini, T.G. Ksiazek, and A. Mishra. 2006. Nipah virus-associated encephalitis outbreak, Siliguri, India. *Emerg Infect Dis*. 12:235-240.

Chan, R.W.Y., K.M. Yuen, W.C.L. Yu, C.C.C. Ho, J.M. Nicholls, J.S.M. Peiris, and M.C.W. Chan. 2010. Influenza H5N1 and H1N1 Virus Replication and Innate Immune Responses in Bronchial Epithelial Cells Are Influenced by the State of Differentiation. *PLoS One*. 5:e8713.

Chua, K.B., K.J. Goh, K.T. Wong, A. Kamarulzaman, P.S. Tan, T.G. Ksiazek, S.R. Zaki, G. Paul, S.K. Lam, and C.T. Tan. 1999. Fatal encephalitis due to Nipah virus among pig-farmers in Malaysia. *Lancet*. 354:1257-1259.

Ciancanelli, M.J., V.A. Volchkova, M.L. Shaw, V.E. Volchkov, and C.F. Basler. 2009. Nipah virus sequesters inactive STAT1 in the nucleus via a P gene-encoded mechanism. *J Virol*. 83:7828-7841.

Cong, Y., M.R. Lentz, A. Lara, I. Alexander, C. Bartos, J.K. Bohannon, D. Hammoud, L. Huzella, P.B. Jahrling, K. Janosko, C. Jett, E. Kollins, M. Lackemeyer, D. Mollura, D. Ragland, O. Rojas, J. Solomon, Z. Xu, V. Munster, and M.R. Holbrook. 2017. Loss in lung volume and changes in the immune response demonstrate disease progression in African green monkeys infected by small-particle aerosol and intratracheal exposure to Nipah virus. *PLoS Negl Trop Dis*. 11:e0005532.

Cox, J., and M. Mann. 2008. MaxQuant enables high peptide identification rates, individualized p.p.b.-range mass accuracies and proteome-wide protein quantification. *Nature Biotechnology*. 26:1367-1372.

Desmyter, J., L. Melnick Joseph, and E. Rawls William. 1968. Defectiveness of Interferon Production and of Rubella Virus Interference in a Line of African Green Monkey Kidney Cells (Vero). *J Virol*. 2:955-961.

Diederich, S., and A. Maisner. 2007. Molecular characteristics of the Nipah virus glycoproteins. 1102:39–50.

Diederich, S., M. Moll, H.-D. Klenk, and A. Maisner. 2005. The Nipah Virus Fusion Protein Is Cleaved within the Endosomal Compartment*. *Journal of Biological Chemistry*. 280:29899-29903.

Diederich, S., L. Thiel, and A. Maisner. 2008. Role of endocytosis and cathepsin-mediated activation in Nipah virus entry. *Virology*. 375:391-400.

Dietzel, E., L. Kolesnikova, B. Sawatsky, A. Heiner, M. Weis, G.P. Kobinger, S. Becker, V.v. Messling, A. Maisner, and T.S. Dermody. 2016. Nipah Virus Matrix Protein Influences Fusogenicity and Is Essential for Particle Infectivity and Stability. 90:2514.

Dietzel, E., L. Kolesnikova, B. Sawatsky, A. Heiner, M. Weis, G.P. Kobinger, S. Becker, V. von Messling, and A. Maisner. 2015. Nipah Virus Matrix Protein Influences Fusogenicity and Is Essential for Particle Infectivity and Stability. *J Virol*. 90:2514-2522.

Dimasuay, K.G., A. Sanchez, N. Schaefer, J. Polanco, D.A. Ferrington, and H.W. Chu. 2018. Immunoproteasomes as a novel antiviral mechanism in rhinovirus-infected airways. *Clinical Science*. 132:1711-1723.

Doyle, T.M. 1927. A hitherto unrecorded disease of fowls due to a filter-passing virus. *J. Comp. Path. Therap.* 40:144-169.

Drexler, J.F., V.M. Corman, M.A. Müller, G.D. Maganga, P. Vallo, T. Binger, F. Gloza-Rausch, V.M. Cottontail, A. Rasche, S. Yordanov, A. Seebens, M. Knörnschild, S. Oppong, Y. Adu Sarkodie, C. Pongombo, A.N. Lukashev, J. Schmidt-Chanasit, A. Stöcker, A.J.B. Carneiro, S. Erbar, A. Maisner, F. Fronhoffs, R. Buettner, E.K.V. Kalko, T. Kruppa, C.R. Franke, R. Kallies, E.R.N. Yandoko, G. Herrler, C. Reusken, A. Hassanin, D.H. Krüger, S. Matthee, R.G. Ulrich, E.M. Leroy, and C. Drosten. 2012. Bats host major mammalian paramyxoviruses. *Nature communications*. 3:796-796.

Elvert, M., L. Sauerhering, and A. Maisner. 2020. Cytokine Induction in Nipah Virus–Infected Primary Human and Porcine Bronchial Epithelial Cells. 221:S395-S400.

Enchery, F., C. Dumont, M. Iampietro, R. Pelissier, N. Aurine, L.M. Bloyet, C. Carbonnelle, C. Mathieu, C. Journo, D. Gerlier, and B. Horvat. 2021. Nipah virus W protein harnesses nuclear 14-3-3 to inhibit NF-kappaB-induced proinflammatory response. *Commun Biol*. 4:1292.

Enders, J.F., and T.C. Peebles. 1954. Propagation in Tissue Cultures of Cytopathogenic Agents from Patients with Measles.†. *Proceedings of the Society for Experimental Biology and Medicine*. 86:277 - 286.

Escaffre, O., V. Borisevich, J.R. Carmical, D. Prusak, J. Prescott, H. Feldmann, and B. Rockx. 2013. Henipavirus pathogenesis in human respiratory epithelial cells. *J Virol*. 87:3284-3294.

Escaffre, O., V. Borisevich, L.A. Vergara, J.W. Wen, D. Long, and B. Rockx. 2016. Characterization of Nipah virus infection in a model of human airway epithelial cells cultured at an air-liquid interface. 97:1077–1086.

Ferenz, N.P., A. Gable, and P. Wadsworth. 2010. Mitotic functions of kinesin-5. *Seminars in Cell & Developmental Biology*. 21:255-259.

Foelsch, D., and P. Leloup. 1976. Fatale endemische Infektion in einem Serpentarium. Tierarztl. *Praxis*. 4:527-536.

Fu, C., W.P. Donovan, O. Shikapwashya-Hasser, X. Ye, and R.H. Cole. 2014. Hot Fusion: an efficient method to clone multiple DNA fragments as well as inverted repeats without ligase. *PLoS One*. 9:e115318-e115318.

Fukasawa, M., M. Nishijima, and K. Hanada. 1999. Genetic Evidence for ATP-dependent Endoplasmic Reticulum-to-Golgi Apparatus Trafficking of Ceramide for Sphingomyelin Synthesis in Chinese Hamster Ovary Cells. *Journal of Cell Biology*. 144:673-685.

Fulcher, M.L., S. Gabriel, K.A. Burns, J.R. Yankaskas, and S.H. Randell. 2005. Well-differentiated human airway epithelial cell cultures. 107:183–206.

Giard, D.J., S.A. Aaronson, G.J. Todaro, P. Arnstein, J.H. Kersey, H. Dosik, and W.P. Parks. 1973. In Vitro Cultivation of Human Tumors: Establishment of Cell Lines Derived From a Series of Solid Tumors2. *JNCI: Journal of the National Cancer Institute*. 51:1417-1423.

Grossegesse, M., D. Bourquain, M. Neumann, L. Schaade, J. Schulze, C. Mache, T. Wolff, A. Nitsche, and J. Doellinger. 2022. Deep Time Course Proteomics of SARS-CoV- and SARS-CoV-2-Infected Human Lung Epithelial Cells (Calu-3) Reveals Strong Induction of Interferon-Stimulated Gene Expression by SARS-CoV-2 in Contrast to SARS-CoV. *Journal of Proteome Research*.

Günther, M., A. Bauer, M. Müller, L. Zaeck, and S. Finke. 2020. Interaction of host cellular factor ANP32B with matrix proteins of different paramyxoviruses. 101:44-58.

Habchi, J., S. Blangy, L. Mamelli, M.R. Jensen, M. Blackledge, H. Darbon, M. Oglesbee, Y. Shu, and S. Longhi. 2011. Characterization of the Interactions between the Nucleoprotein and the Phosphoprotein of Henipavirus*. *Journal of Biological Chemistry*. 286:13583-13602.

Habjan, M., N. Penski, M. Spiegel, and F. Weber. 2008. T7 RNA polymerase-dependent and -independent systems for cDNA-based rescue of Rift Valley fever virus. *Journal of General Virology*. 89:2157-2166.

Halpin, K., B. Bankamp, B.H. Harcourt, W.J. Bellini, and P.A. Rota. 2004. Nipah virus conforms to the rule of six in a minigenome replication assay. *Journal of General Virology*. 85:701-707.

Hanada, K., K. Kumagai, S. Yasuda, Y. Miura, M. Kawano, M. Fukasawa, and M. Nishijima. 2003. Molecular machinery for non-vesicular trafficking of ceramide. *Nature*. 426:803-809.

Hannus, M., M. Beitzinger, J.C. Engelmann, M.-T. Weickert, R. Spang, S. Hannus, and G. Meister. 2014. siPools: highly complex but accurately defined siRNA pools eliminate off-target effects. *Nucleic Acids Res*. 42:8049-8061.

Harcourt, B.H., L. Lowe, A. Tamin, X. Liu, B. Bankamp, N. Bowden, P.E. Rollin, J.A. Comer, T.G. Ksiazek, M.J. Hossain, E.S. Gurley, R.F. Breiman, W.J. Bellini, and P.A. Rota. 2005. Genetic

characterization of Nipah virus, Bangladesh, 2004. *Emerging infectious diseases*. 11:1594-1597.

Harcourt, B.H., A. Tamin, K. Halpin, T.G. Ksiazek, P.E. Rollin, W.J. Bellini, and P.A. Rota. 2001. Molecular Characterization of the Polymerase Gene and Genomic Termini of Nipah Virus. *Virology*. 287:192-201.

Harcourt, B.H., A. Tamin, T.G. Ksiazek, P.E. Rollin, L.J. Anderson, W.J. Bellini, and P.A. Rota. 2000. Molecular Characterization of Nipah Virus, a Newly Emergent Paramyxovirus. *Virology*. 271:334-349.

Harit, A.K., R.L. Ichhpujani, S. Gupta, K.S. Gill, S. Lal, N.K. Ganguly, and S.P. Agarwal. 2006. Nipah/Hendra virus outbreak in Siliguri, West Bengal, India in 2001. *Indian J Med Res*. 123:553-560.

Harrison, M.S., T. Sakaguchi, and A.P. Schmitt. 2010. Paramyxovirus assembly and budding: building particles that transmit infections. *Int J Biochem Cell Biol*. 42:1416-1429.

Harrison, R.G. 1910. The outgrowth of the nerve fiber as a mode of protoplasmic movement. *Journal of Experimental Zoology*. 9:787-846.

Hatton, C.F., R.A. Botting, M.E. Dueñas, I.J. Haq, B. Verdon, B.J. Thompson, J.S. Spegarova, F. Gothe, E. Stephenson, A.I. Gardner, S. Murphy, J. Scott, J.P. Garnett, S. Carrie, J. Powell, C.M.A. Khan, L. Huang, R. Hussain, J. Coxhead, T. Davey, A.J. Simpson, M. Haniffa, S. Hambleton, M. Brodlie, C. Ward, M. Trost, G. Reynolds, and C.J.A. Duncan. 2021. Delayed induction of type I and III interferons mediates nasal epithelial cell permissiveness to SARS-CoV-2. *Nat Commun*. 12:7092.

Hegre, O.D., R.C. McEvoy, V. Bachelder, and A. Lazarow. 1972. Organ Culture of Fetal Rat Pancreas: Quantitative Analysis by Linear Scanning of Islet and Other Tissue Components. *In Vitro*. 7:366-376.

Heinz, Leonhard X., Christoph L. Baumann, Marielle S. Köberlin, B. Snijder, R. Gawish, G. Shui, O. Sharif, Irene M. Aspalter, André C. Müller, Richard K. Kandasamy, Florian P. Breitwieser, A. Pichlmair, M. Bruckner, M. Rebsamen, S. Blüml, T. Karonitsch, A. Fauster, J. Colinge, Keiryn L. Bennett, S. Knapp, Markus R. Wenk, and G. Superti-Furga. 2015. The Lipid-Modifying Enzyme SMPDL3B Negatively Regulates Innate Immunity. *Cell Reports*. 11:1919-1928.

Hekman, R.M., A.J. Hume, R.K. Goel, K.M. Abo, J. Huang, B.C. Blum, R.B. Werder, E.L. Suder, I. Paul, S. Phanse, A. Youssef, K.D. Alysandratos, D. Padhorny, S. Ojha, A. Mora-Martin, D. Kretov, P.E.A. Ash, M. Verma, J. Zhao, J.J. Patten, C. Villacorta-Martin, D. Bolzan, C. Perea-Resa, E. Bullitt, A. Hinds, A. Tilston-Lunel, X. Varelas, S. Farhangmehr, U. Braunschweig, J.H. Kwan, M. McComb, A. Basu, M. Saeed, V. Perissi, E.J. Burks, M.D. Layne, J.H. Connor, R. Davey, J.X. Cheng, B.L. Wolozin, B.J. Blencowe, S. Wuchty, S.M. Lyons, D. Kozakov, D. Cifuentes, M. Blower, D.N. Kotton, A.A. Wilson, E. Muhlberger, and A. Emili. 2020. Actionable Cytopathogenic Host Responses of Human Alveolar Type 2 Cells to SARS-CoV-2. *Mol Cell*. 80:1104-1122 e1109.

Hess, I.M.R., P.D. Massey, B. Walker, D.J. Middleton, and T.M. Wright. 2011. Hendra virus: what do we know? *New South Wales Public Health Bulletin*. 22:118-122.

Hippee, C.E., B.K. Singh, A.L. Thurman, A.L. Cooney, A.A. Pezzulo, R. Cattaneo, and P.L. Sinn. 2021. Measles virus exits human airway epithelia within dislodged metabolically active infectious centers. *PLoS Pathog*. 17:e1009458.

Hooper, P., S. Zaki, P. Daniels, and D. Middleton. 2001. Comparative pathology of the diseases caused by Hendra and Nipah viruses. 3:315–322.

Hooper, P.T., H.A. Westbury, and G.M. Russell. 1997. The Lesions of Experimental Equine Morbillivirus Disease in Cats and Guinea Pigs. *Veterinary Pathology*. 34:323-329.

Hossain, M.J., E.S. Gurley, J.M. Montgomery, M. Bell, D.S. Carroll, V.P. Hsu, P. Formenty, A. Croisier, E. Bertherat, M.A. Faiz, A.K. Azad, R. Islam, M.A. Molla, T.G. Ksiazek, P.A. Rota, J.A. Comer, P.E. Rollin, S.P. Luby, and R.F. Breiman. 2008. Clinical presentation of nipah virus infection in Bangladesh. *Clin Infect Dis*. 46:977-984.

Hsu, V.P., M.J. Hossain, U.D. Parashar, M.M. Ali, T.G. Ksiazek, I. Kuzmin, M. Niezgoda, C. Rupprecht, J. Bresee, and R.F. Breiman. 2004. Nipah virus encephalitis reemergence, Bangladesh. *Emerging infectious diseases*. 10:2082-2087.

Hyatt, A.D., S.R. Zaki, C.S. Goldsmith, T.G. Wise, and S.G. Hengstberger. 2001. Ultrastructure of Hendra virus and Nipah virus within cultured cells and host animals. *Microbes and Infection*. 3:297-306.

ICTV. 2012. Family - Paramyxoviridae. *In* Virus Taxonomy. A.M.Q. King, M.J. Adams, E.B. Carstens, and E.J. Lefkowitz, editors. Elsevier, San Diego. 672-685.

ICTV. 2022. The Master Species List: A Spreadsheet of Current Taxonomy. *In* ICTV_Master_Species_List_2021_v2, https://ictv.global/msl.

Ijperen, C., P. Kuhnert, J. Frey, and J.P. Clewley. 2002. Virulence typing of Escherichia coli using microarrays. *Molecular and Cellular Probes*. 16:371-378.

Johnston Gunner, P., B. Bradel-Tretheway, D. Piehowski Paul, M. Brewer Heather, R. Lee Bom Nae, T. Usher Nicholas, J.L.R. Zamora, V. Ortega, M. Contreras Erik, R. Teuton Jeremy, P. Wendler Jason, M. Matz Keesha, N. Adkins Joshua, and C. Aguilar Hector. 2019. Nipah Virus-Like Particle Egress Is Modulated by Cytoskeletal and Vesicular Trafficking Pathways: a Validated Particle Proteomics Analysis. *mSystems*. 4:e00194-00119.

Kammerl, I.E., and S. Meiners. 2016. Proteasome function shapes innate and adaptive immune responses. *American Journal of Physiology-Lung Cellular and Molecular Physiology*. 311:L328-L336.

Kanehisa, M., and S. Goto. 2000. KEGG: kyoto encyclopedia of genes and genomes. *Nucleic Acids Res*. 28:27-30.

Karas, M., D. Bachmann, and F. Hillenkamp. 1985. Influence of the wavelength in high-irradiance ultraviolet laser desorption mass spectrometry of organic molecules. *Analytical Chemistry*. 57:2935-2939.

Kasloff, S.B., A. Leung, B.S. Pickering, G. Smith, E. Moffat, B. Collignon, C. Embury-Hyatt, D. Kobasa, and H.M. Weingartl. 2019. Pathogenicity of Nipah henipavirus Bangladesh in a swine host. 9:5230.

Keller, I.E., O. Vosyka, S. Takenaka, A. Kloss, B. Dahlmann, L.I. Willems, M. Verdoes, H.S. Overkleeft, E. Marcos, S. Adnot, S.M. Hauck, C. Ruppert, A. Gunther, S. Herold, S. Ohno, H. Adler, O. Eickelberg, and S. Meiners. 2015. Regulation of immunoproteasome function in the lung. *Sci Rep*. 5:10230.

Kolberg, L., Raudvere, U. 2021. Package 'gprofiler2' Version 0.2.1. Available at https://cran.r-project.org/web/packages/gprofiler2/gprofiler2.pdf.

Kraneveld, F.C. 1926. A poultry disease in the Dutch East Indies. *Ned Indisch Bl Diergeneeskd*. 38:448-450.

Kulkarni, D., C. Tosh, G. Venkatesh, and D. Kumar. 2013. Nipah virus infection: Current scenario. *Indian journal of virology : an official organ of Indian Virological Society*. 24:398-408.

Kumagai, A., R. Ando, H. Miyatake, P. Greimel, T. Kobayashi, Y. Hirabayashi, T. Shimogori, and A. Miyawaki. 2013. A Bilirubin-Inducible Fluorescent Protein from Eel Muscle. *Cell*. 153:1602-1611.

Kuroya, M., N. Ishida, and T. Shiratori. 1953. Newborn Virus Pneumonitis (Type Sendai)

II. The Isolation of A New Virus. *The Tohoku Journal of Experimental Medicine*. 58:62-62.

Kvellestad, A., B.H. Dannevig, and K. Falk. 2003. Isolation and partial characterization of a novel paramyxovirus from the gills of diseased seawater-reared Atlantic salmon (Salmo salar L.). *Journal of General Virology*. 84:2179-2189.

Laing, E.D., M. Amaya, C.K. Navaratnarajah, Y.R. Feng, R. Cattaneo, L.F. Wang, and C.C. Broder. 2018. Rescue and characterization of recombinant cedar virus, a non-pathogenic Henipavirus species. *Virol J*. 15:56.

Laing, E.D., C.K. Navaratnarajah, S. Cheliout Da Silva, S.R. Petzing, Y. Xu, S.L. Sterling, G.A. Marsh, L.F. Wang, M. Amaya, D.B. Nikolov, R. Cattaneo, C.C. Broder, and K. Xu. 2019. Structural and functional analyses reveal promiscuous and species specific use of ephrin receptors by Cedar virus. *Proc Natl Acad Sci U S A*. 116:20707-20715.

Lamers, M.M., J. van der Vaart, K. Knoops, S. Riesebosch, T.I. Breugem, A.Z. Mykytyn, J. Beumer, D. Schipper, K. Bezstarosti, C.D. Koopman, N. Groen, R.B.G. Ravelli, H.Q. Duimel, J.A.A. Demmers, G. Verjans, M.P.G. Koopmans, M.J. Muraro, P.J. Peters, H. Clevers, and B.L. Haagmans. 2021. An organoid-derived bronchioalveolar model for SARS-CoV-2 infection of human alveolar type II-like cells. *Embo j*. 40:e105912.

Lee, K.-E., T. Umapathi, C.-B. Tan, H. Tjoei-Lian Tjia, T.-S. Chua, H.M.-L. Oh, K.-M. Fock, A. Kurup, A. Das, A.K.-Y. Tan, and W.-L. Lee. 1999. The neurological manifestations of Nipah virus encephalitis, a novel paramyxovirus. *Annals of Neurology*. 46:428-432.

Lee, S.-H., K. Kim, J. Kim, J.S. No, K. Park, S. Budhathoki, S.H. Lee, J. Lee, S.H. Cho, S. Cho, G.-Y. Lee, J. Hwang, H.-C. Kim, T.A. Klein, C.-S. Uhm, W.-K. Kim, and J.-W. Song. 2021. Discovery and Genetic Characterization of Novel Paramyxoviruses Related to the Genus Henipavirus in Crocidura Species in the Republic of Korea. *Viruses*. 13.

Leon, A.J., V. Borisevich, N. Boroumand, R. Seymour, R. Nusbaum, O. Escaffre, L. Xu, D.J. Kelvin, and B. Rockx. 2018. Host gene expression profiles in ferrets infected with genetically distinct henipavirus strains. *PLoS Negl Trop Dis*. 12:e0006343.

Levens, J.H., and J.F. Enders. 1945. The Hemoagglutinative Properties of Amniotic Fluid from Embryonated Eggs Infected with Mumps Virus. *Science*. 102:117-120.

Leyrat, C., M. Renner, K. Harlos, J.T. Huiskonen, and J.M. Grimes. 2014. Structure and self-assembly of the calcium binding matrix protein of human metapneumovirus. *Structure*. 22:136-148.

Li, M., C. Embury-Hyatt, and H.M. Weingartl. 2010. Experimental inoculation study indicates swine as a potential host for Hendra virus. *Vet Res*. 41:33-33.

Li, Z., M. Yu, H. Zhang, D.E. Magoffin, P.J.M. Jack, A. Hyatt, H.-Y. Wang, and L.-F. Wang. 2006. Beilong virus, a novel paramyxovirus with the largest genome of non-segmented negative-stranded RNA viruses. *Virology*. 346:219-228.

Lieu, K.G., G.A. Marsh, L.-F. Wang, and H.J. Netter. 2015. The non-pathogenic Henipavirus Cedar paramyxovirus phosphoprotein has a compromised ability to target STAT1 and STAT2. *Antiviral Research*. 124:69-76.

Lin, H., H. Li, H.-J. Cho, S. Bian, H.-J. Roh, M.-K. Lee, J.S. Kim, S.-J. Chung, C.-K. Shim, and D.-D. Kim. 2007. Air-Liquid Interface (ALI) Culture of Human Bronchial Epithelial Cell Monolayers as an in vitro Model for Airway Drug Transport Studies. *Journal of Pharmaceutical Sciences*. 96:341-350.

Lin, W.-H.W., A.J. Tsay, E.N. Lalime, A. Pekosz, and D.E. Griffin. 2021. Primary differentiated respiratory epithelial cells respond to apical measles virus infection by shedding multinucleated giant cells. *Proceedings of the National Academy of Sciences*. 118:e2013264118.

Liou, T.G., F.R. Adler, B.C. Cahill, D.R. Cox, J.E. Cox, G.J. Grant, K.E. Hanson, S.C. Hartsell, N.D. Hatton, M.N. Helms, J.L. Jensen, C. Kartsonaki, Y. Li, D.T. Leung, J.E. Marvin, E.A. Middleton, S.M. Osburn-Staker, K.A. Packer, S.M. Shakir, A.B. Sturrock, K.D. Tardif, K.J. Warren, L.J. Waddoups, L.J. Weaver, E. Zimmerman, and R. Paine, 3rd. 2021. SARS-CoV-2 innate effector associations and viral load in early nasopharyngeal infection. *Physiol Rep*. 9:e14761.

Liu, Q., J.A. Stone, B. Bradel-Tretheway, J. Dabundo, J.A. Benavides Montano, J. Santos-Montanez, S.B. Biering, A.V. Nicola, R.M. Iorio, X. Lu, and H.C. Aguilar. 2013. Unraveling a three-step spatiotemporal mechanism of triggering of receptor-induced Nipah virus fusion and cell entry. *PLoS pathogens*. 9:e1003770-e1003770.

Livak, K.J., and T.D. Schmittgen. 2001. Analysis of Relative Gene Expression Data Using Real-Time Quantitative PCR and the 2−ΔΔCT Method. *Methods*. 25:402-408.

Lo, M.K., D. Miller, M. Aljofan, B.A. Mungall, P.E. Rollin, W.J. Bellini, and P.A. Rota. 2010. Characterization of the antiviral and inflammatory responses against Nipah virus in endothelial cells and neurons. *Virology*. 404:78-88.

Lo, M.K., and P.A. Rota. 2008. The emergence of Nipah virus, a highly pathogenic paramyxovirus. 43:396–400.

Luby, S.P., and C.C. Broder. 2014. Paramyxoviruses: Henipaviruses. *In* Viral Infections of Humans: Epidemiology and Control. R.A. Kaslow, L.R. Stanberry, and J.W. Le Duc, editors. Springer US, Boston, MA. 519-536.

Luby, S.P., M. Rahman, M.J. Hossain, L.S. Blum, M.M. Husain, E. Gurley, R. Khan, B.-N. Ahmed, S. Rahman, N. Nahar, E. Kenah, J.A. Comer, and T.G. Ksiazek. 2006. Foodborne transmission of Nipah virus, Bangladesh. *Emerging infectious diseases*. 12:1888-1894.

Madera, S., A. Kistler, H. Ranaivoson, V. Ahyong, A. Andrianiaina, S. Andry, V. Raharinosy, T. Randriambolamanantsoa, N.A. Fifi Ravelomanantsoa, C. Tato, J. DeRisi, H. Aguilar, V. Lacoste, P. Dussart, J.-M. Heraud, and C. Brook. 2022. Discovery and Genomic Characterization of a Novel Henipavirus, Angavokely virus, from fruit bats in Madagascar. bioRxiv.

Mandel, M., and A. Higa. 1970. Calcium-dependent bacteriophage DNA infection. *Journal of Molecular Biology*. 53:159-162.

Marsh, G.A., C. de Jong, J.A. Barr, M. Tachedjian, C. Smith, D. Middleton, M. Yu, S. Todd, A.J. Foord, V. Haring, J. Payne, R. Robinson, I. Broz, G. Crameri, H.E. Field, and L.F. Wang. 2012. Cedar virus: a novel Henipavirus isolated from Australian bats. *PLoS Pathog*. 8:e1002836.

Marsh, G.A., E.R. Virtue, I. Smith, S. Todd, R. Arkinstall, L. Frazer, P. Monaghan, G.A. Smith, C.C. Broder, D. Middleton, and L.-F. Wang. 2013. Recombinant Hendra viruses expressing a reporter gene retain pathogenicity in ferrets. *Virology Journal*. 10:95.

Martin, A., P. Staeheli, and U. Schneider. 2006. RNA Polymerase II-Controlled Expression of Antigenomic RNA Enhances the Rescue Efficacies of Two Different Members of the Mononegavirales Independently of the Site of Viral Genome Replication. *J Virol*. 80:5708-5715.

Martinez-Gil, L., N.M. Vera-Velasco, and I. Mingarro. 2017. Exploring the Human-Nipah Virus Protein-Protein Interactome. *J Virol*. 91.

Mathieu, C., V. Guillaume, V.A. Volchkova, C. Pohl, F. Jacquot, R.Y. Looi, K.T. Wong, C. Legras-Lachuer, V.E. Volchkov, J. Lachuer, and B. Horvat. 2012. Nonstructural Nipah Virus C Protein Regulates both the Early Host Proinflammatory Response and Viral Virulence. *J Virol*. 86:10766-10775.

Mathieu, C., C. Legras-Lachuer, and B. Horvat. 2011. Transcriptome Signature of Nipah Virus Infected Endothelial Cells. *In* Advances in the Etiology, Pathogenesis and Pathology of Vasculitis. L.M. Amezcua-Guerra, editor. InTech.

Matsui, H., B.R. Grubb, R. Tarran, S.H. Randell, J.T. Gatzy, C.W. Davis, and R.C. Boucher. 1998a. Evidence for Periciliary Liquid Layer Depletion, Not Abnormal Ion Composition, in the Pathogenesis of Cystic Fibrosis Airways Disease. *Cell*. 95:1005-1015.

Matsui, H., S.H. Randell, S.W. Peretti, C.W. Davis, and R.C. Boucher. 1998b. Coordinated clearance of periciliary liquid and mucus from airway surfaces. *The Journal of clinical investigation*. 102:1125-1131.

McCormack, J.G., A.M. Allworth, L.A. Selvey, and P.W. Selleck. 1999. Transmissibility from horses to humans of a novel paramyxovirus, equine morbillivirus (EMV). *Journal of Infection*. 38:22-23.

Mehand, M.S., F. Al-Shorbaji, P. Millett, and B. Murgue. 2018. The WHO R&D Blueprint: 2018 review of emerging infectious diseases requiring urgent research and development efforts. *Antiviral Research*. 159:63-67.

Mehrfeld, C., S. Zenner, M. Kornek, and V. Lukacs-Kornek. 2018. The Contribution of Non-Professional Antigen-Presenting Cells to Immunity and Tolerance in the Liver. *Frontiers in Immunology*. 9:635.

Meier, F., S. Beck, N. Grassl, M. Lubeck, M.A. Park, O. Raether, and M. Mann. 2015. Parallel Accumulation–Serial Fragmentation (PASEF): Multiplying Sequencing Speed and Sensitivity by Synchronized Scans in a Trapped Ion Mobility Device. *Journal of Proteome Research*. 14:5378-5387.

Mertens, T.C.J., H. Karmouty-Quintana, C. Taube, and P.S. Hiemstra. 2017. Use of airway epithelial cell culture to unravel the pathogenesis and study treatment in obstructive airway diseases. *Pulmonary Pharmacology & Therapeutics*. 45:101-113.

Middleton, D.J., C.J. Morrissy, B.M. van der Heide, G.M. Russell, M.A. Braun, H.A. Westbury, K. Halpin, and P.W. Daniels. 2007. Experimental Nipah Virus Infection in Pteropid Bats (Pteropus poliocephalus). *Journal of Comparative Pathology*. 136:266-272.

Middleton, D.J., H.A. Westbury, C.J. Morrissy, B.M. van der Heide, G.M. Russell, M.A. Braun, and A.D. Hyatt. 2002. Experimental Nipah Virus Infection in Pigs and Cats. 126:124–136.

Miller, A.J., and J.R. Spence. 2017. In Vitro Models to Study Human Lung Development, Disease and Homeostasis. *Physiology (Bethesda)*. 32:246-260.

Mohd Nor, M.N., C.H. Gan, and B.L. Ong. 2000. Nipah virus infection of pigs in peninsular Malaysia. 19:160–165.

Mulay, A., B. Konda, G. Garcia, C. Yao, S. Beil, J.M. Villalba, C. Koziol, C. Sen, A. Purkayastha, J.K. Kolls, D.A. Pociask, P. Pessina, J.S. de Aja, C. Garcia-de-Alba, C.F. Kim, B. Gomperts, V. Arumugaswami, and B.R. Stripp. 2021. SARS-CoV-2 infection of primary human lung epithelium for COVID-19 modeling and drug discovery. *Cell Reports*. 35:109055.

Mullis, K., F. Faloona, S. Scharf, R. Saiki, G. Horn, and H. Erlich. 1986. Specific enzymatic amplification of DNA in vitro: the polymerase chain reaction. *Cold Spring Harb Symp Quant Biol.* 51:263-273.

Murray, K., R. Rogers, L. Selvey, P. Selleck, A. Hyatt, A. Gould, L. Gleeson, P. Hooper, and H. Westbury. 1995. A novel morbillivirus pneumonia of horses and its transmission to humans. *Emerging infectious diseases*. 1:31-33.

Negrete, O.A., E.L. Levroney, H.C. Aguilar, A. Bertolotti-Ciarlet, R. Nazarian, S. Tajyar, and B. Lee. 2005. EphrinB2 is the entry receptor for Nipah virus, an emergent deadly paramyxovirus. *Nature*. 436:401-405.

Neuhoff, V., N. Arold, D. Taube, and W. Ehrhardt. 1988. Improved staining of proteins in polyacrylamide gels including isoelectric focusing gels with clear background at nanogram sensitivity using Coomassie Brilliant Blue G-250 and R-250. *Electrophoresis*. 9:255-262.

Niwa, H., Y. Ken-ichi, and M. Jun-ichi. 1991. Efficient selection for high-expression transfectants with a novel eukaryotic vector. *Gene*. 108:193-199.

O'Sullivan, J.D., A.M. Allworth, D.L. Paterson, T.M. Snow, R. Boots, L.J. Gleeson, A.R. Gould, A.D. Hyatt, and J. Bradfield. 1997. Fatal encephalitis due to novel paramyxovirus transmitted from horses. *The Lancet*. 349:93-95.

Oei, E., T. Kalb, P. Beuria, M. Allez, A. Nakazawa, M. Azuma, M. Timony, Z. Stuart, H. Chen, and K. Sperber. 2004. Accessory cell function of airway epithelial cells. *Am J Physiol Lung Cell Mol Physiol*. 287:L318-331.

Pager, C.T., W.W. Craft, J. Patch, and R.E. Dutch. 2006. A mature and fusogenic form of the Nipah virus fusion protein requires proteolytic processing by cathepsin L. *Virology*. 346:251-257.

Park, M.-S., M.L. Shaw, J. Muñoz-Jordan, J.F. Cros, T. Nakaya, N. Bouvier, P. Palese, A. García-Sastre, and C.F. Basler. 2003. Newcastle disease virus (NDV)-based assay demonstrates interferon-antagonist activity for the NDV V protein and the Nipah virus V, W, and C proteins. *J Virol*. 77:1501-1511.

Patch, J.R., Z. Han, S.E. McCarthy, L. Yan, L.-F. Wang, R.N. Harty, and C.C. Broder. 2008. The YPLGVG sequence of the Nipah virus matrix protein is required for budding. *Virology Journal*. 5:137.

Pelissier, R., M. Iampietro, and B. Horvat. 2019. Recent advances in the understanding of Nipah virus immunopathogenesis and anti-viral approaches. *F1000Res*. 8.

Perez-Riverol, Y., A. Csordas, J. Bai, M. Bernal-Llinares, S. Hewapathirana, D.J. Kundu, A. Inuganti, J. Griss, G. Mayer, M. Eisenacher, E. Pérez, J. Uszkoreit, J. Pfeuffer, T. Sachsenberg, Ş. Yılmaz, S. Tiwary, J. Cox, E. Audain, M. Walzer, A.F. Jarnuczak, T. Ternent, A. Brazma, and J.A. Vizcaíno. 2019. The PRIDE database and related tools and resources in 2019: improving support for quantification data. *Nucleic Acids Research*. 47:D442-D450.

Prianichnikov, N., H. Koch, S. Koch, M. Lubeck, R. Heilig, S. Brehmer, R. Fischer, and J. Cox. 2020. MaxQuant Software for Ion Mobility Enhanced Shotgun Proteomics. *Mol Cell Proteomics*. 19:1058-1069.

Pruniéras, M., M. Régnier, and D. Woodley. 1983. Methods for Cultivation of Keratinocytes with an Air-Liquid Interface. *Journal of Investigative Dermatology*. 81:S28-S33.

Pryce, R., K. Azarm, I. Rissanen, K. Harlos, T.A. Bowden, and B. Lee. 2020. A key region of molecular specificity orchestrates unique ephrin-B1 utilization by Cedar virus. 3.

R Core Team. 2020. R: A Language and Environment for Statistical Computing. R Foundation for Statistical Computing, Vienna, Austria.

Rawlinson, S.M., T. Zhao, A.M. Rozario, C.L. Rootes, P.J. McMillan, A.W. Purcell, A. Woon, G.A. Marsh, K.G. Lieu, L.F. Wang, H.J. Netter, T.D.M. Bell, C.R. Stewart, and G.W. Moseley. 2018. Viral regulation of host cell biology by hijacking of the nucleolar DNA-damage response. *Nat Commun*. 9:3057.

Renshaw, R.W., A.L. Glaser, H. Van Campen, F. Weiland, and E.J. Dubovi. 2000. Identification and Phylogenetic Comparison of Salem Virus, a Novel Paramyxovirus of Horses. *Virology*. 270:417-429.

Rhim, J.S., and K. Schell. 1967. Cytopathic and Plaque Assay of Rubella Virus in a Line of African Green Monkey Kidney Cells (Vero). *Proceedings of the Society for Experimental Biology and Medicine*. 125:602-606.

Riese, R.J., P.R. Wolf, D. Bromme, L.R. Natkin, J.A. Villadangos, H.L. Ploegh, and H.A. Chapman. 1996. Essential role for cathepsin S in MHC class II-associated invariant chain processing and peptide loading. *Immunity*. 4:357-366.

Rima, B., A. Balkema-Buschmann, W.G. Dundon, P. Duprex, A. Easton, R. Fouchier, G. Kurath, R. Lamb, B. Lee, P. Rota, L. Wang, and C. Ictv Report. 2019. ICTV Virus Taxonomy Profile: Paramyxoviridae. *The Journal of general virology*. 100:1593-1594.

Ringel, M., A. Heiner, L. Behner, S. Halwe, L. Sauerhering, N. Becker, E. Dietzel, B. Sawatsky, L. Kolesnikova, and A. Maisner. 2019. Nipah virus induces two inclusion body populations: Identification of novel inclusions at the plasma membrane. *PLOS Pathogens*. 15:e1007733.

Rodriguez, J.J., C.D. Cruz, and C.M. Horvath. 2004. Identification of the nuclear export signal and STAT-binding domains of the Nipah virus V protein reveals mechanisms underlying interferon evasion. *J Virol*. 78:5358-5367.

Rodriguez, J.J., J.-P. Parisien, and C.M. Horvath. 2002. Nipah virus V protein evades alpha and gamma interferons by preventing STAT1 and STAT2 activation and nuclear accumulation. *J Virol*. 76:11476-11483.

Rodriguez, K.R., and C.M. Horvath. 2013. Amino acid requirements for MDA5 and LGP2 recognition by paramyxovirus V proteins: a single arginine distinguishes MDA5 from RIG-I. *J Virol*. 87:2974-2978.

Rous, P., and F.S. Jones. 1916. A METHOD FOR OBTAINING SUSPENSIONS OF LIVING CELLS FROM THE FIXED TISSUES, AND FOR THE PLATING OUT OF INDIVIDUAL CELLS. *Journal of Experimental Medicine*. 23:549-555.

RStudio Team. 2020. RStudio: Integrated Development for R. RStudio, PBC, Boston, Available at http://www.rstudio.com/.

Sah, R., A. Mohanty, S. Chakraborty, and K. Dhama. 2022. Langya virus: A newly identified zoonotic henipavirus. *Journal of Medical Virology*. 94:5621-5622.

Sampath, R., T.A. Hall, C. Massire, F. Li, L.B. Blyn, M.W. Eshoo, S.A. Hofstadler, and D.J. Ecker. 2007. Rapid Identification of Emerging Infectious Agents Using PCR and Electrospray Ionization Mass Spectrometry. *Annals of the New York Academy of Sciences*. 1102:109-120.

Sanchez-Aparicio, M.T., L.J. Feinman, A. Garcia-Sastre, and M.L. Shaw. 2018. Paramyxovirus V Proteins Interact with the RIG-I/TRIM25 Regulatory Complex and Inhibit RIG-I Signaling. *J Virol*. 92.

Sanger, F., S. Nicklen, and A.R. Coulson. 1977. DNA sequencing with chain-terminating inhibitors. *Proc Natl Acad Sci U S A*. 74:5463-5467.

Sasaki, M., M. Kishimoto, Y. Itakura, K. Tabata, K. Intaruck, K. Uemura, S. Toba, T. Sanaki, A. Sato, W.W. Hall, Y. Orba, and H. Sawa. 2021. Air-liquid interphase culture confers SARS-CoV-2 susceptibility to A549 alveolar epithelial cells. *Biochemical and Biophysical Research Communications*. 577:146-151.

Satterfield, B.A., R.W. Cross, K.A. Fenton, K.N. Agans, C.F. Basler, T.W. Geisbert, and C.E. Mire. 2015. The immunomodulating V and W proteins of Nipah virus determine disease course. *Nature Communications*. 6:7483.

Sauerhering, L., H. Müller, L. Behner, M. Elvert, S.K. Fehling, T. Strecker, and A. Maisner. 2017. Variability of interferon-λ induction and antiviral activity in Nipah virus infected differentiated human bronchial epithelial cells of two human donors. *Journal of General Virology*. 98:2447-2453.

Sauerhering, L., M. Zickler, M. Elvert, L. Behner, T. Matrosovich, S. Erbar, M. Matrosovich, and A. Maisner. 2016. Species-specific and individual differences in Nipah virus replication in porcine and human airway epithelial cells. *Journal of General Virology*. 97:1511-1519.

Schindelin, J., I. Arganda-Carreras, E. Frise, V. Kaynig, M. Longair, T. Pietzsch, S. Preibisch, C. Rueden, S. Saalfeld, B. Schmid, J.-Y. Tinevez, D.J. White, V. Hartenstein, K. Eliceiri, P. Tomancak, and A. Cardona. 2012. Fiji: an open-source platform for biological-image analysis. *Nature Methods*. 9:676-682.

Schnell, M.J., T. Mebatsion, and K.K. Conzelmann. 1994. Infectious rabies viruses from cloned cDNA. *The EMBO Journal*. 13:4195-4203.

Schoggins, J.W., and C.M. Rice. 2011. Interferon-stimulated genes and their antiviral effector functions. *Curr Opin Virol*. 1:519-525.

Schountz, T., C. Campbell, K. Wagner, J. Rovnak, C. Martellaro, B.L. DeBuysscher, H. Feldmann, and J. Prescott. 2019. Differential Innate Immune Responses Elicited by Nipah Virus and Cedar Virus Correlate with Disparate In Vivo Pathogenesis in Hamsters. *Viruses*. 11.

Seo, Y.-J., C. Blake, S. Alexander, and B. Hahm. 2010. Sphingosine 1-Phosphate-Metabolizing Enzymes Control Influenza Virus Propagation and Viral Cytopathogenicity. *J Virol*. 84:8124-8131.

Shannon, P., A. Markiel, O. Ozier, N.S. Baliga, J.T. Wang, D. Ramage, N. Amin, B. Schwikowski, and T. Ideker. 2003. Cytoscape: A Software Environment for Integrated Models of Biomolecular Interaction Networks. *Genome Research*. 13:2498-2504.

Sharma, V., S. Kaushik, R. Kumar, J.P. Yadav, and S. Kaushik. 2019. Emerging trends of Nipah virus: A review. *Reviews in Medical Virology*. 29:e2010.

Sharma, V.K., I. Sharma, and J. Glick. 2020. The expanding role of mass spectrometry in the field of vaccine development. *Mass Spectrometry Reviews*. 39:83-104.

Shaw, M.L., W.B. Cardenas, D. Zamarin, P. Palese, and C.F. Basler. 2005. Nuclear localization of the Nipah virus W protein allows for inhibition of both virus- and toll-like receptor 3-triggered signaling pathways. *J Virol*. 79:6078-6088.

Shaw, M.L., A. Garcia-Sastre, P. Palese, and C.F. Basler. 2004. Nipah virus V and W proteins have a common STAT1-binding domain yet inhibit STAT1 activation from the cytoplasmic and nuclear compartments, respectively. *J Virol*. 78:5633-5641.

Shen, L., L.J. Sigal, M. Boes, and K.L. Rock. 2004. Important role of cathepsin S in generating peptides for TAP-independent MHC class I crosspresentation in vivo. *Immunity*. 21:155-165.

Shi, M., X.-D. Lin, X. Chen, J.-H. Tian, L.-J. Chen, K. Li, W. Wang, J.-S. Eden, J.-J. Shen, L. Liu, E.C. Holmes, and Y.-Z. Zhang. 2018. The evolutionary history of vertebrate RNA viruses. *Nature*. 556:197-202.

Shin, E.C., U. Seifert, T. Kato, C.M. Rice, S.M. Feinstone, P.M. Kloetzel, and B. Rehermann. 2006. Virus-induced type I IFN stimulates generation of immunoproteasomes at the site of infection. *J Clin Invest*. 116:3006-3014.

Shortridge, K.F., and D.J. Alexander. 1978. Incidence and preliminary characterisation of a hitherto unreported, serologically distinct, avian paramyxovirus isolated in Hong Kong. *Research in Veterinary Science*. 25:128-130.

Simoes, M., A. Saleh, Y.-M. Choi, M.V. Airola, J.D. Haley, and N. Coant. 2022. Measurement of neutral ceramidase activity in vitro and in vivo. *Analytical Biochemistry*. 643:114577.

Singhal, N., M. Kumar, P.K. Kanaujia, and J.S. Virdi. 2015. MALDI-TOF mass spectrometry: an emerging technology for microbial identification and diagnosis. *Frontiers in Microbiology*. 6.

Sioud, M. 2004. Therapeutic siRNAs. *Trends in Pharmacological Sciences*. 25:22-28.

Smith, H.O., and K.W. Welcox. 1970. A Restriction enzyme from Hemophilus influenzae: I. Purification and general properties. *Journal of Molecular Biology*. 51:379-391.

Sugai, A., H. Sato, I. Takayama, M. Yoneda, and C. Kai. 2017. Nipah and Hendra Virus Nucleoproteins Inhibit Nuclear Accumulation of Signal Transducer and Activator of Transcription 1 (STAT1) and STAT2 by Interfering with Their Complex Formation. *J Virol*. 91.

Sun, W., T.S. McCrory, W.Y. Khaw, S. Petzing, T. Myers, and A.P. Schmitt. 2014. Matrix proteins of Nipah and Hendra viruses interact with beta subunits of AP-3 complexes. *J Virol*. 88:13099-13110.

Suzuki, T., and Y. Suzuki. 2006. Virus Infection and Lipid Rafts. *Biological and Pharmaceutical Bulletin*. 29:1538-1541.

Tamin, A., B.H. Harcourt, T.G. Ksiazek, P.E. Rollin, W.J. Bellini, and P.A. Rota. 2002. Functional Properties of the Fusion and Attachment Glycoproteins of Nipah Virus. *Virology*. 296:190-200.

Tanabe, M., M. Kurita-Taniguchi, K. Takeuchi, M. Takeda, M. Ayata, H. Ogura, M. Matsumoto, and T. Seya. 2003. Mechanism of up-regulation of human Toll-like receptor 3 secondary to infection of measles virus-attenuated strains. *Biochemical and Biophysical Research Communications*. 311:39-48.

Tanaka, K., H. Waki, Y. Ido, S. Akita, Y. Yoshida, T. Yoshida, and T. Matsuo. 1988. Protein and polymer analyses up to m/z 100 000 by laser ionization time-of-flight mass spectrometry. *Rapid Communications in Mass Spectrometry*. 2:151-153.

Temin, H.M., and S. Mizutani. 1970. Viral RNA-dependent DNA Polymerase: RNA-dependent DNA Polymerase in Virions of Rous Sarcoma Virus. *Nature*. 226:1211-1213.

Tikasingh, E.S., A.H. Jonkers, L. Spence, and T.H.G. Aitken. 1966. Nariva Virus, a Hitherto Undescribed Agent Isolated from the Trinidadian Rat, Zygodontomys B. Brevicauda (J. A. Allen & Chapman). *The American Journal of Tropical Medicine and Hygiene*. 15:235-238.

Tisoncik, J.R., R. Billharz, S. Burmakina, S.E. Belisle, S.C. Proll, M.J. Korth, A. Garcia-Sastre, and M.G. Katze. 2011. The NS1 protein of influenza A virus suppresses interferon-regulated activation of antigen-presentation and immune-proteasome pathways. *J Gen Virol*. 92:2093-2104.

Torres-Velez, F.J., W.J. Shieh, P.E. Rollin, T. Morken, C. Brown, T.G. Ksiazek, and S.R. Zaki. 2008. Histopathologic and Immunohistochemical Characterization of Nipah Virus Infection in the Guinea Pig. *Veterinary Pathology*. 45:576-585.

Tyanova, S., T. Temu, P. Sinitcyn, A. Carlson, M.Y. Hein, T. Geiger, M. Mann, and J. Cox. 2016. The Perseus computational platform for comprehensive analysis of (prote)omics data. *Nat Methods*. 13:731-740.

Vera-Velasco, N.M., M.J. García-Murria, M.M. Sánchez del Pino, I. Mingarro, and L. Martinez-Gil. 2018. Proteomic composition of Nipah virus-like particles. *Journal of Proteomics*. 172:190-200.

Vijayan, M., C. Xia, Y.E. Song, H. Ngo, C.J. Studstill, K. Drews, T.E. Fox, M.C. Johnson, J. Hiscott, M. Kester, S. Alexander, and B. Hahm. 2017. Sphingosine 1-Phosphate Lyase Enhances the Activation of IKKε To Promote Type I IFN–Mediated Innate Immune Responses to Influenza A Virus Infection. *The Journal of Immunology*. 199:677.

Vogt, C., M. Eickmann, S. Diederich, M. Moll, and A. Maisner. 2005. Endocytosis of the Nipah virus glycoproteins. 79:3865–3872.

von Neumann, J. 1941. Distribution of the Ratio of the Mean Square Successive Difference to the Variance. *The Annals of Mathematical Statistics*. 12:367-395, 329.

Walker, P.J., S.G. Siddell, E.J. Lefkowitz, A.R. Mushegian, E.M. Adriaenssens, D.M. Dempsey, B.E. Dutilh, B. Harrach, R.L. Harrison, R.C. Hendrickson, S. Junglen, N.J. Knowles, A.M. Kropinski, M. Krupovic, J.H. Kuhn, M. Nibert, R.J. Orton, L. Rubino, S. Sabanadzovic, P. Simmonds, D.B. Smith, A. Varsani, F.M. Zerbini, and A.J. Davison. 2020. Changes to virus taxonomy and the Statutes ratified by the International Committee on Taxonomy of Viruses (2020). *Archives of Virology*. 165:2737-2748.

Wang, L.-F., B.H. Harcourt, M. Yu, A. Tamin, P.A. Rota, W.J. Bellini, and B.T. Eaton. 2001. Molecular biology of Hendra and Nipah viruses. *Microbes and Infection*. 3:279-287.

Wang, L.F., W.P. Michalski, M. Yu, L.I. Pritchard, G. Crameri, B. Shiell, and B.T. Eaton. 1998. A novel P/V/C gene in a new member of the Paramyxoviridae family, which causes lethal infection in humans, horses, and other animals. *J Virol*. 72:1482-1490.

Wang, L.F., M. Yu, E. Hansson, L.I. Pritchard, B. Shiell, W.P. Michalski, and B.T. Eaton. 2000. The exceptionally large genome of Hendra virus: support for creation of a new genus within the family Paramyxoviridae. *J Virol*. 74:9972-9979.

Wang, Y.E., A. Park, M. Lake, M. Pentecost, B. Torres, T.E. Yun, M.C. Wolf, M.R. Holbrook, A.N. Freiberg, and B. Lee. 2010. Ubiquitin-regulated nuclear-cytoplasmic trafficking of the Nipah virus matrix protein is important for viral budding. *PLoS Pathog*. 6:e1001186.

Watkinson, R.E., and B. Lee. 2016. Nipah virus matrix protein: expert hacker of cellular machines. *FEBS Lett*. 590:2494-2511.

Webster, R.G., M. Morita, C. Pridgen, and B. Tumova. 1976. Ortho- and Paramyxoviruses from Migrating Feral Ducks: Characterization of a New Group of Influenza A Viruses. *Journal of General Virology*. 32:217-225.

Weingartl, H. 2015. Hendra and Nipah viruses: pathogenesis, animal models and recent breakthroughs in vaccination. *Vaccine: Development and Therapy*. 2015:59.

Whitcutt, M.J., K.B. Adler, and R. Wu. 1988. A biphasic chamber system for maintaining polarity of differentiation of culture respiratory tract epithelial cells. *In Vitro Cellular & Developmental Biology*. 24:420-428.

WHO. 2022. Prioritizing diseases for research and development in emergency contexts. World Health Organization (who.int), https://www.who.int/activities/prioritizing-diseases-for-research-and-development-in-emergency-contexts.

Wickham, H.C., W.; Takahashi, K.; Wilke, C.; Woo, K.; Yutani, H.; Dunnington, D.; RStudio 2021. Package 'ggplot2' - Version 3.3.5. Available at https://cran.r-project.org/web/packages/ggplot2/ggplot2.pdf.

Wisniewski, J.R., A. Zougman, N. Nagaraj, and M. Mann. 2009. Universal sample preparation method for proteome analysis. *Nat Methods*. 6:359-362.

Wolf, J.J., C. Xia, C.J. Studstill, H. Ngo, S.L. Brody, P.E. Anderson, and B. Hahm. 2021. Influenza A virus NS1 induces degradation of sphingosine 1-phosphate lyase to obstruct the host innate immune response. *Virology*. 558:67-75.

Wolff, M.M., and W.E. Stephens. 1953. A Pulsed Mass Spectrometer with Time Dispersion. *Review of Scientific Instruments*. 24:616-617.

Wong, K.T., I. Grosjean, C. Brisson, B. Blanquier, M. Fevre-Montange, A. Bernard, P. Loth, M.-C. Georges-Courbot, M. Chevallier, H. Akaoka, P. Marianneau, S.K. Lam, T.F. Wild, and V. Deubel. 2003. A golden hamster model for human acute Nipah virus infection. *Am J Pathol*. 163:2127-2137.

Wu, N.-H., W. Yang, A. Beineke, R. Dijkman, M. Matrosovich, W. Baumgärtner, V. Thiel, P. Valentin-Weigand, F. Meng, and G. Herrler. 2016. The differentiated airway epithelium infected by influenza viruses maintains the barrier function despite a dramatic loss of ciliated cells. *Scientific Reports*. 6:39668.

Wu, Z., L. Yang, F. Yang, X. Ren, J. Jiang, J. Dong, L. Sun, Y. Zhu, H. Zhou, and Q. Jin. 2014. Novel Henipa-like virus, Mojiang Paramyxovirus, in rats, China, 2012. *Emerging infectious diseases*. 20:1064-1066.

Xu, K., C.C. Broder, and D.B. Nikolov. 2012. Ephrin-B2 and ephrin-B3 as functional henipavirus receptors. *Seminars in Cell & Developmental Biology*. 23:116-123.

Yamaguchi, M., Y. Kitagawa, M. Zhou, M. Itoh, and B. Gotoh. 2014. An anti-interferon activity shared by paramyxovirus C proteins: Inhibition of Toll-like receptor 7/9-dependent alpha interferon induction. *FEBS Letters*. 588:28-34.

Yamashita, M., and J.B. Fenn. 1984. Electrospray ion source. Another variation on the free-jet theme. *The Journal of Physical Chemistry*. 88:4451-4459.

Yasumura, Y., and Y. Kawakita. 1963. Studies on SV40 in tissue culture-preliminary step for cancer research in vitro. *Nihon rinsho*. 21:1201-1215.

Yob, J.M., H. Field, A.M. Rashdi, C. Morrissy, B. van der Heide, P. Rota, A. bin Adzhar, J. White, P. Daniels, A. Jamaluddin, and T. Ksiazek. 2001. Nipah virus infection in bats (order Chiroptera) in peninsular Malaysia. *Emerging infectious diseases*. 7:439-441.

Yoneda, M., V. Guillaume, F. Ikeda, Y. Sakuma, H. Sato, T.F. Wild, and C. Kai. 2006. Establishment of a Nipah virus rescue system. *Proceedings of the National Academy of Sciences*. 103:16508-16513.

Yu, M., E. Hansson, B. Shiell, W. Michalski, B.T. Eaton, and L.-F. Wang. 1998. Sequence analysis of the Hendra virus nucleoprotein gene: comparison with other members of the subfamily Paramyxovirinae. *Journal of General Virology*. 79:1775-1780.

Zhang, L., M.E. Peeples, R.C. Boucher, P.L. Collins, and R.J. Pickles. 2002. Respiratory syncytial virus infection of human airway epithelial cells is polarized, specific to ciliated cells, and without obvious cytopathology. *J Virol*. 76:5654-5666.

Zhang, X.-A., H. Li, F.-C. Jiang, F. Zhu, Y.-F. Zhang, J.-J. Chen, C.-W. Tan, D.E. Anderson, H. Fan, L.-Y. Dong, C. Li, P.-H. Zhang, Y. Li, H. Ding, L.-Q. Fang, L.-F. Wang, and W. Liu. 2022. A Zoonotic Henipavirus in Febrile Patients in China. *New England Journal of Medicine*. 387:470-472.

9. Appendix

9.1. Supplementary data

Supplementary data 1 to 10 are deposited on the zenodo platform (https://zenodo.org/) with the data set identifier 10.5281/zenodo.7728169.

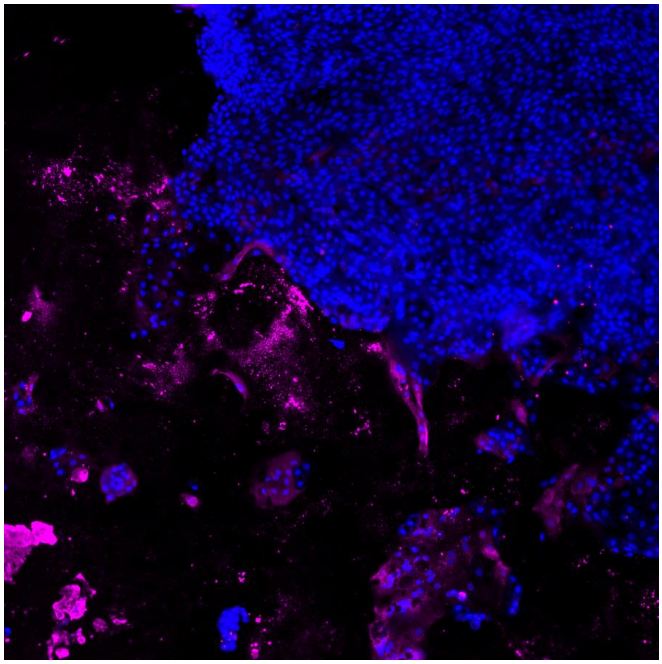

Supplement 7: Immunofluorescence detection of NiV N in FPBEC-ALI culture 12 dpi. Magnification of NiV infected FBEC-ALI culture 12 dpi (see Figure 10). Immunostaining against NiV N (magenta). Nuclei were counterstained using Hoechst 33342.

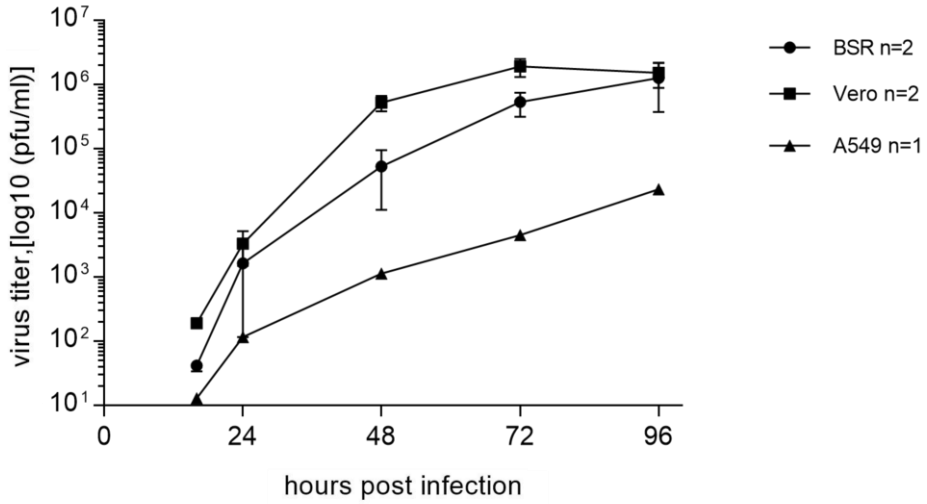

Supplement 11: Growth curves of rCedPV C-R68K on BSR-T7/5, Vero and A549 cells. BSR-T7/5, Vero and A549 cells were infected with rescued rCedPV C-R68K (see 4.3.1) and the titer of the replication kinetics was determined on the respective cell lines (see 4.3.5). In BSR-T7/5 and A549 cells, rCedPV grew to 10 and 60 fold lower end titers compared to Vero cells. Results are depicted as the mean of two, two and one replicates for BSR-T7/5, Vero and A549 cells, respectively. Error bars indicate the standard deviation.

9.2. List of figures

9.3. List of tables

9.4. Acronyms and abbreviations

ALI	air-liquid interface
AngV	Angavokely virus
ANP32B	acidic leucine-rich nuclear phosphoprotein 32 family member B
APCs	antigen-presenting cells
ASAH2B	neutral ceramidase B
ATV	Alsever's Trypsin-Versene
B2M	beta-2-microglobulin
BEC	primary bronchial epithelial cells
CALN	Calnexin
CALR	Calreticulin
CARDs	caspase activation and recruitment domains
CCLV	Collection of Cell Lines in Veterinary Medicine
cDNA	complementary DNA
CDS	coding sequence
CedPV	Cedar virus
CERT	ceramide transfer protein
CLSM	Confocal laser-scanning microscopy
Ct	cycle threshold
CTL	cytotoxic T cell
CTSS	cathepsin S
CV	crystal violet
DARV	Daeryong virus
DEG	differentially expressed genes
DNA	deoxyribonucleic acid
EFN	ephrin
eGFP	enhanced green fluorescent protein
ESI	electrospray ionization
F	Fusion protein
FA	formic acid
FASP	filter-aided sample preparation
FBEC	ferret primary bronchial epithelial cells
FCS	fetal calf serum
FDR	false discovery rate
FLI	Friedrich-Loeffler-Institut

G	Glycoprotein
GAKV	Gamak virus
GhV	Ghana virus
GO	Gene Ontology
GO:BP	Gene Ontology biological processes
GO:CC	Gene Ontology cellular components
HBSS	Hank's Balanced Salt Solution
HBSS	Hanks' Balanced Salt solution
HCV	Hepatitis C virus
HDV-SC	hepatitis delta-ribozyme-sequence
HEPES	4-(2-hydroxyethyl)-1-piperazineethanesulfonic acid
HeV	Hendra virus
IAV	Influenza A virus
IBs	inclusion bodies
IFIT2	interferon-induced protein with tetratricopeptide repeats 2
IFN	interferon
IFN-β	interferon beta
IFN-λ	interferon lambda
IKKε	IKKepsilon Kinase
IL-6	interleukin 6
IL-8	interleukin 8
IRF	interferon regulatory factor
ISG-56	IFN-stimulated gene 56
KEGG	Kyoto Encyclopedia of Genes and Genomes
L	RNA-dependent RNA Polymerase
LayV	Langya virus
LFQ	label free quantification
LGP2	laboratory of genetics and physiology gene 2
M	Matrix protein
MALDI	matrix-assisted laser desorption/ionization
MDA5	melanoma differentiation-associated gene 5
MeV	Measles virus
MHC I	major histocompatibility complex class I
MHC II	major histocompatibility complex class II
MHV-68	murine gammaherpesvirus-68

min	minute
MOI	multiplicity of infection
MojV	Mojiang virus
MQ	MaxQuant
MS	mass spectrometry
MuV	Mumps virus
MX	interferon-induced GTP-binding protein Mx protein
N	Nucleoprotein
NCDS	non-coding sequence
NiV	Nipah Virus
NiV_B	Nipah virus Bangladesh strain
NiV_M	Nipah virus Malaysia strain
NLS	nuclear localization signal
Nm	nanometer
nM	nanomolar
OAS	oligoadenylatsynthetase
ORF	open reading frame
P	Phosphoprotein
PASEF	Parallel Accumulation and Serial Fragmentation
PBEC	porcine primary bronchial epithelial cells
PBS	Phosphate buffered saline
PBST	0.2 % Triton X-100 in phosphate buffered saline
PBS-T	0.1 % Tween 20 in phosphate buffered saline
PCA	principal component analysis
PCR	polymerase chain reaction
PCs	principal components
PEDV	porcine epidemic diarrhea virus
PFA	paraformaldehyde
pfu	plaque forming units
PLC	peptide loading complex
PRRSV	porcine reproductive and respiratory syndrome virus
PTPN1	protein tyrosine phosphatase non-receptor type 1
qPCR	real-time PCR
rCedPV	recombinant Cedar virus
RIG	retinoic acid-inducible gene

RNP	ribonucleoprotein complex
rpm	rounds per minute
RT	room temperature
SARS-CoV-2	severe acute respiratory syndrome-coronavirus-2
SGPL1	sphingosine-1-phosphate lyase
siRNA	small interfering RNA
SMPDL3B	acid sphingomyelinase-like phosphodiesterase 3b
STAT	signal transducer and activator of transcription
T7P	T7 promotor
T7T	T7 terminator
THUNDER	instant computational clearing mode
TIMS	trapped ion mobility spectrometry
TLR	toll-like receptor
TOF-MS	time-of-flight mass spectrometry
TurboFP635	Katushka
nTurboFP635	nuclear localizing Katushka
TRIM	tripartite motif-containing protein
UDG	Uracil-DNA glycosylase
UnaG	Bilirubin-inducible fluorescent protein UnaG
nUnaG	nuclear localizing Bilirubin-inducible fluorescent protein UnaG
VLP	virus-like particles
ZO-1	zonula occludens 1

9.5. Eigenständigkeitserklärung

Hiermit erkläre ich, dass diese Arbeit bisher von mir weder an der Mathematisch-Naturwissenschaftlichen Fakultät der Universität Greifswald noch einer anderen wissenschaftlichen Einrichtung zum Zwecke der Promotion eingereicht wurde.

Ferner erkläre ich, dass ich diese Arbeit selbstständig verfasst und keine anderen als die darin angegebenen Hilfsmittel und Hilfen benutzt und keine Textabschnitte eines Dritten ohne Kennzeichnung übernommen habe.

_____

Martin Müller

9.6. Curriculum Vitae

9.7. Publications

Müller, M., Fischer, K., Woehnke, E., Zaeck, M. L., Prönnecke, C., Knittler, M. R., Karger, A., Diederich, S., Finke, S. (2023). Analysis of Nipah Virus Replication and Host Proteome Response Patterns in Differentiated Porcine Airway Epithelial Cells Cultured at the Air–Liquid Interface. *Viruses* 2023, 15, 961.

Gunther, M., Bauer, A., Müller, M., Zaeck, L., Finke, S. (2020). Interaction of host cellular factor ANP32B with matrix proteins of different paramyxoviruses. *J Gen Virol* 2020 Vol. 101 Issue 1 Pages 44-58

Zaeck, L.M., Scheibner, D., Sehl, J., Müller, M., Hoffmann, D., Beer, M., Abdelwhab, E.M., Mettenleiter, T.C., Breithaupt, A., Finke, S. (2021). Light Sheet Microscopy-Assisted 3D Analysis of SARS-CoV-2 Infection in the Respiratory Tract of the Ferret Model. *Viruses* 2021, 13, 529

9.8. Oral and poster presentations

18.03. – 19.03.2019 **Paramyxovirus-Meeting (FLI – PEI – University of Marburg), Langen, Germany, Presentation.** " Establishment of Henipa-reverse genetics". **Martin Müller**, Stefan Finke

13.10. – 15.10.2021 **Zoonoses 2021 – International Symposium on Zoonoses Research, Online Conference, Presentation.** "Characterization of the Nipah virus in well-differentiated porcine bronchial epithelial cells cultured at the air-liquid interface". Due to personal familiarly circumstances this presentation had to be hold by Luca M. Zaeck.
Martin Müller, Kerstin Fischer, Elisabeth Wöhnke, **Luca M. Zaeck**, Axel Karger, Sandra Diederich, Stefan Finke

25.09. – 27.09.2019 **Junior Scientist Symposium of the FLI, Jena, Germany, Poster.** "Establishment of reverse genetic systems for Henipaviruses and molecular characterization of virus-host interactions".
Müller, M., Finke, S.

24.03. – 26.03.2021 **30th Annual Meeting of the Society for Virology, Online-Conference, Poster.** "Characterization of the Nipah virus in well-differentiated porcine bronchial epithelial cells cultured at the air-liquid interface"
Martin Müller, Kerstin Fischer, Luca M. Zaeck, Sandra Diederich, Stefan Finke

20.10. – 21.10.2021 **Junior Scientist Symposium of the FLI, Online-Conference, Poster. "**Characterization of the Nipah virus in well-differentiated porcine bronchial epithelial cells cultured at the air-liquid interface".
Martin Müller, Kerstin Fischer, Luca M. Zaeck, Sandra Diederich, Stefan Finke

30.03. – 02.04.2022 **31th Annual Meeting of the Society for Virology, Online-Conference, Poster.** "Characterization of the Nipah virus in well-differentiated porcine bronchial epithelial cells cultured at the air-liquid interface"
Martin Müller, Kerstin Fischer, Elisabeth Wöhnke, Luca M. Zaeck, Axel Karger, Sandra Diederich, Stefan Finke

9.9. Acknowledgments

Viele Kollegen, Mitarbeiter und Freunde haben mich während meiner Zeit als Doktorand begleitet. Sie haben mich nicht nur unterstützt und motiviert, sondern auch geholfen mich weiterzuentwickeln und zu wachsen. Ohne euch wäre ich nicht dort wo ich nun bin. Hiermit möchte ich mich bei all diesen Menschen bedanken.

Für die Möglichkeit meine Arbeit am Institut für molekulare Virologie und Zellbiologie des Friedrich-Loeffler-Instituts anzufertigen, möchte ich mich bei Prof. Dr. Dr. h. c. Thomas C. Mettenleiter bedanken.

Mein besonderer Dank gilt Prof. Dr. Stefan Finke für die Aufnahme in seinem Labor, die wissenschaftliche Beratung und die Unterstützung als Erstbetreuer. Ich kann stolz behaupten, dass sich ein Doktorand keinen besseren Betreuer für seine Arbeit wünschen kann. Er hatte nicht nur ein offenes Ohr für alle meine Probleme und Fragen, sondern hat mir durch seine herzliche Art auch durch meine schwierigste Zeit geholfen. Vielen Dank!

Wissenschaft funktioniert nur durch gute Zusammenarbeit und die hat während meiner Zeit am Friedrich-Loeffler-Institut herausragend funktioniert. Ich möchte mich dafür insbesondere bei Dr. Sandra Diederich und Dr. Kerstin Fischer für die Arbeiten im BSL-4 Labor bedanken. Die Diskussionen, Planungen und der Input waren nicht nur hilfreich sondern haben mir immer viel Freude bereitet. Im gleichen Zuge möchte ich hier auch Dr. Axel Karger, Elisabeth Wöhnke und Barabara Bettin erwähnen. Im letzen Jahr meiner Arbeit haben sie nicht nur die massenspektrometischen Analysen durchgeführt sondern mich auch essentiell bei der Auswertung unterstützt. Ich habe noch nie soviel, in so kurzer Zeit gelernt und bedanke mich für eure Geduld und Hilfe vom ganzen Herzen.

Einer der Standpfeiler von wissenschaftlicher Arbeit ist der Laboralltag welcher nicht ohne tolle und herzliche Kollegen funktionieren kann. Da ohne technische Mitarbeiter gar nichts läuft, möchte ich mich ganz besonders bei Angela Hillner und Katrin Giesow bedanken. Nicht nur für die aufbauenden Worte, die viele Hilfe und Problemlösungen sondern auch für die tollen Arbeitstage. Im Gleichen Zuge möchte ich allen anderen Kollegen danken. Dr. Luca Zaeck, Diana Palme, Dr. Madlin Potratz, Dr. Thomas Müller, Dr. Conrad Freuling, Ola Bagato, Henriette Schwotzer und alle anderen – vielen Dank für das tolle Arbeitsumfeld. Unbedingt erwähnen möchte ich auch Kristin Virgils - die beste Sekretärin. Sie hat nicht nur Institutsweite Planung übernommen, sondern hat mir auch bei allen organisatorischen Fragen geholfen, selbst nach meiner Zeit am Friedrich-Loeffler-Institut.

Was wäre Laborarbeit ohne ein wenig Abwechslung? Daher möchte ich mich im Anschluss bei den tollen Studenten bedanken die wir im Labor hatten, insbesondere Oliver Trunschke, Julia Werner, Maximillian Richter und Carlotta Weigel.

Nun möchte ich mich bei meinen Eltern und meinem Bruder bedanken. Meine Mutter hat mich immer unterstützt und motiviert. Auch wenn Sie den Abschluss meiner Arbeit nun nicht mehr erleben kann, bin ich mir sicher das Sie unendlich stolz auf mich wäre. Ohne meinen Bruder und meinen Vater hätte ich es nicht soweit gebracht. Zuletzt bedanke ich mich bei meiner Frau. Auf unserer Hochzeit sind nicht nur Familie und Freunde zusammen gekommen sondern auch Arbeitskollegen, welche den Tag unvergesslich gemacht haben – Vielen Dank!